Published for SISSA by Springer

Received: November 25, 2018
Revised: March 12, 2019
Accepted: April 20, 2019
Published: April 23, 2019

Jet veto resummation with jet rapidity cuts

Johannes K.L. Michel, Piotr Pietrulewicz and Frank J. Tackmann

Theory Group, Deutsches Elektronen-Synchrotron (DESY), D-22607 Hamburg, Germany

E-mail: johannes.michel@desy.de, piotr.pietrulewicz@desy.de, frank.tackmann@desy.de

Abstract: Jet vetoes are widely used in experimental analyses at the LHC to distinguish different hard-interaction processes. Experimental jet selections require a cut on the (pseudo)rapidity of reconstructed jets, $|\eta_{\text{jet}}| \leq \eta_{\text{cut}}$. We extend the standard jet-p_T (jet-veto) resummation, which implicitly works in the limit $\eta_{\text{cut}} \to \infty$, by incorporating a finite jet rapidity cut. We also consider the case of a step in the required p_T^{cut} at an intermediate value of $|\eta| \simeq 2.5$, which is of experimental relevance to avoid the increased pile-up contamination beyond the reach of the tracking detectors. We identify all relevant parametric regimes, discuss their factorization and resummation as well as the relations between them, and show that the phenomenologically relevant regimes are free of large nonglobal logarithms. The η_{cut} dependence of all resummation ingredients is computed to the same order to which they are currently known for $\eta_{\text{cut}} \to \infty$. Our results pave the way for carrying out the jet-veto resummation including a sharp cut or a step at η_{cut} to the same order as is currently available in the $\eta_{\text{cut}} \to \infty$ limit. The numerical impact of the jet rapidity cut is illustrated for benchmark $q\bar{q}$ and gg initiated color-singlet processes at NLL′+NLO. We find that a rapidity cut at high $\eta_{\text{cut}} = 4.5$ is safe to use and has little effect on the cross section. A sharp cut at $\eta_{\text{cut}} = 2.5$ can in some cases lead to a substantial increase in the perturbative uncertainties, which can be mitigated by instead using a step in the veto.

Keywords: Jets, QCD Phenomenology

ArXiv ePrint: 1810.12911

Open Access, © The Authors.
Article funded by SCOAP[3].

https://doi.org/10.1007/JHEP04(2019)142

JHEP04(2019)142

Contents

1 Introduction 1

2 Factorization with no constraint beyond $\eta_{\rm cut}$ ($\tilde{p}_T^{\rm cut} = \infty$) 4
- 2.1 Overview of parametric regimes 4
- 2.2 Regime 1: $p_T^{\rm cut}/Q \gg e^{-\eta_{\rm cut}}$ (standard jet veto resummation) 5
- 2.3 Regime 2: $p_T^{\rm cut}/Q \sim e^{-\eta_{\rm cut}}$ ($\eta_{\rm cut}$ dependent beam functions) 7
- 2.4 Regime 3: $p_T^{\rm cut}/Q \ll e^{-\eta_{\rm cut}}$ (collinear NGLs) 13
- 2.5 Comparison to the literature 18

3 Generalization to a step in the jet veto at $\eta_{\rm cut}$ 20
- 3.1 Overview of parametric regimes 20
- 3.2 $p_T^{\rm cut}/Q \sim \tilde{p}_T^{\rm cut}/Q \sim e^{-\eta_{\rm cut}}$ (collinear step) 21
- 3.3 $p_T^{\rm cut}/Q \ll \tilde{p}_T^{\rm cut}/Q \sim e^{-\eta_{\rm cut}}$ (collinear NGLs) 23
- 3.4 $p_T^{\rm cut}/Q \sim \tilde{p}_T^{\rm cut}/Q \ll e^{-\eta_{\rm cut}}$ (soft-collinear step) 24
- 3.5 $p_T^{\rm cut}/Q \ll \tilde{p}_T^{\rm cut}/Q \ll e^{-\eta_{\rm cut}}$ (soft-collinear NGLs) 27

4 Numerical results 27
- 4.1 Fixed-order matching and perturbative uncertainties 28
- 4.2 Comparing different treatments of the jet rapidity cut 28
- 4.3 Resummed predictions with a sharp rapidity cut 31
- 4.4 Resummed predictions with a step in the jet veto 34

5 Conclusion 34

A Perturbative ingredients 35
- A.1 Anomalous dimensions 36
- A.2 Beam function master formula for $\eta_{\rm cut} \to \infty$ 37
- A.3 Rapidity cut dependent beam functions 39
- A.4 Soft-collinear functions 42
- A.5 Comparison to quark beam function results in the literature 43
- A.6 Mellin convolutions in the two-loop rapidity dependent beam function 44

B Jet rapidity cuts in $\mathcal{T}_B$ and $\mathcal{T}_C$ vetoes 44

1 Introduction

Measurements that involve a veto on additional jets, or more generally that divide events into exclusive jet bins, play an important role at the LHC, e.g. in Higgs and diboson measurements or in searches for physics beyond the Standard Model. The jet binning differentiates between hard processes that differ in the number of hard signal jets, and hence allows one to separate signal and background processes. The separation into 0-jet

JHEP04(2019)142

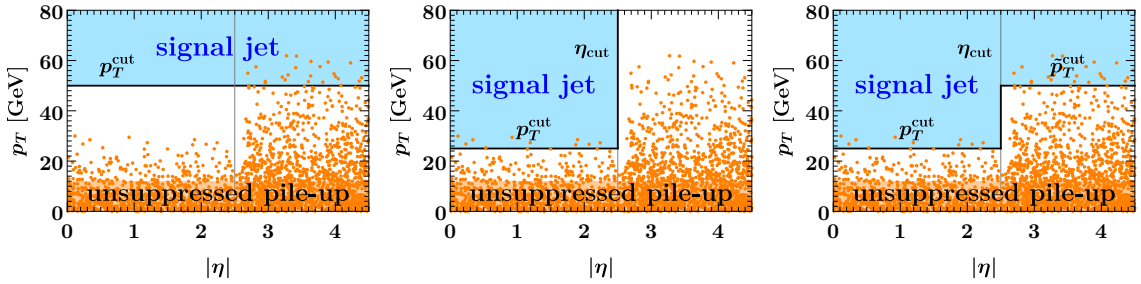

Figure 1. Cartoon of possible strategies to avoid contamination from unsuppressed pile up in jet-binned analyses. The pile-up suppression is much better in the pseudorapidity range $|\eta| \lesssim 2.5$, where it can use information from the tracking detectors. To avoid the higher pile-up contamination in the forward region, one can raise the jet threshold (left panel), only consider central jets (middle panel), or combine both approaches by using a step-like jet selection (right panel).

and $\geq$ 1-jet bins also provides a model-independent way to discriminate between $q\bar{q}$ and gg initiated processes [1].

A veto on jets with transverse momentum $p_T > p_T^{\text{cut}}$ gives rise to double logarithms $\ln^2(p_T^{\text{cut}}/Q)$ at each order in α_s, where Q is the characteristic momentum transfer of the hard interaction. These logarithms dominate the perturbative series when $p_T^{\text{cut}} \ll Q$, and represent an important source of theory uncertainty [2, 3]. They can be systematically resummed to improve the perturbative predictions and assess the associated uncertainties, which has been well-developed in Drell-Yan and Higgs production [2, 4–17], and has also been applied to several other color-singlet processes [1, 18–25].

Experiments can only reconstruct jets up to some maximal pseudorapidity $|\eta| \leq \eta_{\text{cut}}$ due to the range of the detector, e.g. for ATLAS and CMS $\eta_{\text{cut}} \sim 4.5$. In principle, the utility of the jet binning to discriminate between different hard processes increases for a tighter jet veto (smaller p_T^{cut}). However, jets with small transverse momenta are difficult to reconstruct experimentally, especially for pseudorapidity $|\eta| \gtrsim 2.5$ beyond the reach of the tracking detectors, which are important to suppress the large contamination from pile up (e.g. in the jet vertex tagging algorithm used by ATLAS [26]). This is illustrated in figure 1. As the LHC luminosity increases and pile-up conditions become harsher, the contamination from unsuppressed pile-up jets grows worse and must be avoided. One option is to increase the overall p_T^{cut}. For example, in the context of Higgs measurements, the increased pile up in Run 2 has forced raising the jet threshold from 25 GeV to 30 GeV. This however weakens the jet veto and thus reduces its utility. Alternatively, to avoid raising the jet threshold, one can consider jets only in a restricted pseudorapidity range of $|\eta| \lesssim 2.5$. However, this looses the discrimination power from forward jets, which are a distinguishing feature of some processes (most notably weak-boson fusion topologies in Higgs and diboson production). The best possible option combines both approaches and performs a step-like jet selection, with a lower p_T^{cut} threshold for central jets and a somewhat higher $\tilde{p}_T^{\text{cut}}$ threshold for forward jets. For example, recent ATLAS Higgs measurements [27] reconstruct jets using $p_T^{\text{cut}} = 25\,\text{GeV}$ for $|\eta| < 2.4$ and $\tilde{p}_T^{\text{cut}} = 30\,\text{GeV}$ for $|\eta| > 2.4$ (and no jets beyond rapidity $|y| = 4.4$).

JHEP04(2019)142

A discontinuous step in the jet threshold can also pose challenges on its own, as it makes the experimental measurements more complex. Theoretically, we will see that it can complicate the resummation of logarithms in some extreme cases. An alternative to a step is to use jet vetoes that smoothly depend on the jet rapidity [16, 28], providing a tighter veto at central rapidities and a looser one at forward rapidities. These rapidity-dependent vetoes can also be supplemented with an additional sharp jet rapidity cut, which we briefly discuss in appendix B.

The usual jet-p_T resummations [6–9, 12, 13] do not account for any jet rapidity dependence, i.e., the resummation is performed for $\eta_{\text{cut}} \to \infty$. Using parton-shower Monte Carlos, one finds that a jet rapidity cut at $\eta_{\text{cut}} = 4.5$ has a very small numerical effect, while $\eta_{\text{cut}} = 2.5$ has a sizable effect on the jet-p_T spectrum in Higgs production (see e.g. refs. [2, 6]), so it is important to properly include it in the resummation. This was already pointed out in ref. [8], where it was also speculated that a jet rapidity cut might change the resummation structure.

Our analysis in this paper fully addresses these questions by systematically incorporating the jet rapidity cut into the jet-p_T resummation, including in particular the case of a step-like veto. For this purpose, we extend the formalism of refs. [8, 13], which uses the framework of Soft-Collinear Effective Theory (SCET) [29–32]. To be concrete, our discussion focuses on color-singlet production, including the important cases of Higgs and Drell-Yan production. Our results for how to incorporate the η_{cut} dependence also carry over to processes with additional signal jets in the final state to the same extent to which the usual jet-p_T resummation for color-singlet production carries over to such cases [10, 11].

We identify all relevant parametric regimes in the veto parameters p_T^{cut}, η_{cut}, $\tilde{p}_T^{\text{cut}}$, and discuss the factorization and resummation structure for each regime. We also study the relations between the different regimes and perform numerical studies to check their respective ranges of validity. An important conclusion of our analysis is that all regions of parameter space that are of phenomenological interest can be described by parametric regimes that are free of large nonglobal logarithms.

We analytically compute the η_{cut} dependence of all ingredients at $\mathcal{O}(\alpha_s)$ as well as of the dominant $\mathcal{O}(\alpha_s^2)$ corrections (those enhanced by jet-veto or jet clustering logarithms), which matches the order to which they are currently known in the $\eta_{\text{cut}} \to \infty$ limit. Our results allow for carrying out the jet-veto resummation including jet rapidity cuts to the same order as is currently available without such cuts, which for color-singlet production is NNLL′+NNLO. (Reaching this level also requires the still unknown nonlogarithmic $\mathcal{O}(\alpha_s^2)$, which can be extracted numerically from the full NNLO calculation, as was done for $\eta_{\text{cut}} \to \infty$ in ref. [13]. Carrying out such an analysis is beyond the scope of this paper.)

The effect of a rapidity cut for transverse momentum vetoes has also been considered independently in refs. [33, 34] for dijet production, and more recently for the transverse energy event shape in Drell-Yan in ref. [35]. We compare their results to our results for the case of a sharp cut at η_{cut} and no measurement beyond in section 2.5.

The paper is organized as follows: in section 2, we discuss the parametric regimes and corresponding effective field theory (EFT) setups for a sharp cut on reconstructed jets at η_{cut} and no measurement beyond, as in the middle panel of figure 1. We give the

JHEP04(2019)142

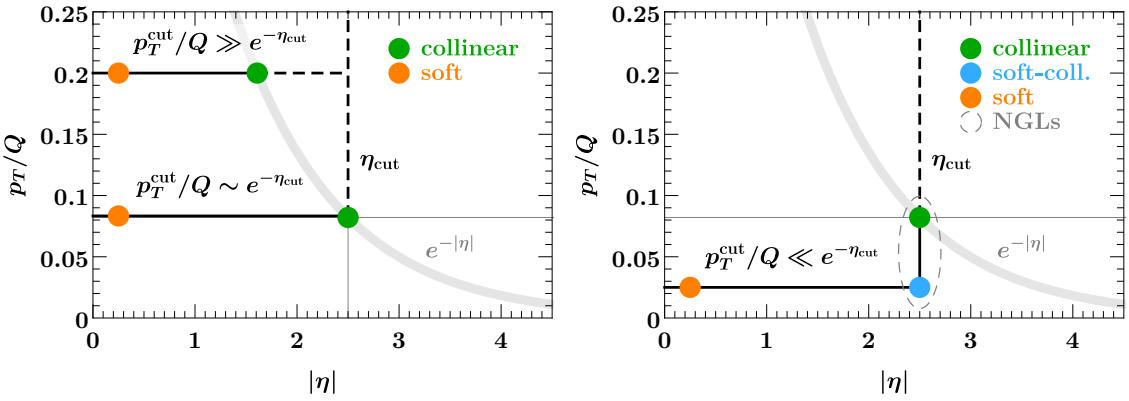

Figure 2. Illustration of the parametric regimes for a jet veto with a jet rapidity cut. Emissions above the black solid lines are vetoed as $p_T > p_T^{\rm cut}$ up to $|\eta| < \eta_{\rm cut} = 2.5$. The thick gray line corresponds to $p_T/Q = e^{-|\eta|}$, and emissions above and to the right of it are power suppressed. The colored circles indicate the relevant modes in the effective theory for a given hierarchy between $p_T^{\rm cut}/Q$ and $e^{-\eta_{\rm cut}}$. For $p_T^{\rm cut} = 25\,\text{GeV}$, the given examples for $p_T^{\rm cut}/Q$ correspond to $Q = 125\,\text{GeV}$ (left panel, upper case), $Q = 300\,\text{GeV}$ (left panel, lower case), $Q = 1\,\text{TeV}$ (right panel).

perturbative ingredients at $\mathcal{O}(\alpha_s)$ and the leading small-R clustering terms at $\mathcal{O}(\alpha_s^2)$ for all partonic channels. We numerically validate the EFT setup by comparing to the relevant singular limits of full QCD, and also compare the regimes to each other and identify their respective ranges of validity. In section 3, we generalize the results of section 2 to a step in the jet veto at $\eta_{\rm cut}$, as in the right panel of figure 1. In section 4, we illustrate the numerical impact of the rapidity cut at NLL′+NLO for Drell-Yan at $Q = m_Z$ and $Q = 1\,\text{TeV}$ and for $gg \to H$ at $m_H = 125\,\text{GeV}$ and $gg \to X$ at $m_X = 1\,\text{TeV}$ for different values of $\eta_{\rm cut}$. We conclude in section 5. Details of our calculations can be found in appendix A. In appendix B, we briefly discuss how an additional sharp rapidity cut affects the description of the rapidity-dependent jet vetoes introduced in ref. [16].

2 Factorization with no constraint beyond $\eta_{\rm cut}$ ($\tilde{p}_T^{\rm cut} = \infty$)

2.1 Overview of parametric regimes

We consider exclusive 0-jet cross sections, where the veto is applied by identifying jets with radius R (the details of the jet-clustering algorithm are not relevant at the order we are working) and cutting on the transverse momentum $p_T^{\rm jet}$ of the leading jet within $|\eta_{\rm jet}| < \eta_{\rm cut}$,

$$\max_{k\in\text{jets}:\,|\eta_k|<\eta_{\rm cut}} |\vec{p}_{T,k}| < p_T^{\rm cut}\,. \tag{2.1}$$

The resulting constraints on the rapidities and transverse momenta of initial-state radiation (ISR) are displayed as black lines in figure 2. We can identify two distinct power-counting parameters that govern the typical angular size of energetic collinear ISR with energy $E \sim Q$, where Q is the momentum transferred in the hard interaction: first, the p_T of the emissions is constrained by $p_T < p_T^{\rm cut}$ for $|\eta| < \eta_{\rm cut}$, corresponding to a maximum opening

JHEP04(2019)142

angle

$$\frac{p_T}{E} \lesssim \frac{p_T^{\text{cut}}}{Q}\,. \tag{2.2}$$

Second, the p_T of an energetic emission at rapidity η is parametrically $p_T \sim Qe^{-|\eta|}$. The rapidity cut removes the first constraint for $|\eta| > \eta_{\text{cut}}$. Hence, if η_{cut} is central enough, emissions beyond η_{cut} can reach a characteristic $p_T \lesssim Qe^{-|\eta_{\text{cut}}|}$, corresponding to a maximum opening angle

$$\frac{p_T}{E} \lesssim e^{-\eta_{\text{cut}}}\,. \tag{2.3}$$

There are three parametric regimes for p_T^{cut}/Q and $e^{-\eta_{\text{cut}}}$, which are illustrated in figure 2 for $\eta_{\text{cut}} = 2.5$. The thick black lines show the veto for different values of p_T^{cut}/Q. The thick gray curve shows the relation $p_T/Q = e^{-|\eta|}$, while the thin gray lines show the values of η_{cut} and $p_T/Q = e^{-\eta_{\text{cut}}}$.

The first parametric regime is $p_T^{\text{cut}}/Q \gg e^{-\eta_{\text{cut}}}$. As we will demonstrate in section 2.2, in this regime effects due to the rapidity cut are power suppressed by $Qe^{-\eta_{\text{cut}}}/p_T^{\text{cut}}$. Hence, they can be treated as a fixed-order power correction to the standard jet-veto resummation, which implicitly works in the limit $\eta_{\text{cut}} = \infty$. For Higgs measurements with $p_T^{\text{cut}} = 25\,\text{GeV}$, $\eta_{\text{cut}} = 4.5$, $Q \equiv m_H = 125\,\text{GeV}$, this parametric assumption is well justified, as $m_H e^{-\eta_{\text{cut}}}/p_T^{\text{cut}} \sim 5\%$.

For heavier final states and/or more central rapidity cuts the relevant parametric regime is $p_T^{\text{cut}}/Q \sim e^{-\eta_{\text{cut}}}$. This is the case for example for $Q = 1\,\text{TeV}$ and $\eta_{\text{cut}} = 4.5$ or $Q = 125\,\text{GeV}$ and $\eta_{\text{cut}} = 2.5$ at $p_T^{\text{cut}} = 25\,\text{GeV}$. In section 2.3, we show that in this regime the rapidity cut effects must be treated as a leading-power correction, and that they can be seamlessly incorporated into the existing jet-veto resummation without rapidity cut. We will see that they affect only the boundary terms in the resummed cross section, but not the anomalous dimensions and evolution factors. Hence, they start contributing at NLL′ or NNLL.

Finally in section 2.4, we discuss the parametric regime $p_T^{\text{cut}}/Q \ll e^{-\eta_{\text{cut}}}$. This case is conceptually interesting, since logarithms of the ratio of scales $Qe^{-\eta_{\text{cut}}}$ and p_T^{cut} appear, changing the logarithmic structure already at leading-logarithmic (LL) order. In addition, formally large nonglobal logarithms of the same ratio appear. This regime is of very limited phenomenological relevance for typical jet-binned analyses at the LHC. For example, for $\eta_{\text{cut}} = 2.3$ corresponding to $e^{-\eta_{\text{cut}}} = 0.1$, it would require an extremely tight jet veto $p_T^{\text{cut}} \ll 0.1\,Q$, which is unrealistic as it would leave almost no signal in the 0-jet cross section. For the purpose of explicitly probing this regime experimentally, one could lower $\eta_{\text{cut}} \simeq 1.0$–$1.5$, such that the jet veto only acts on radiation in the very central region.

2.2 Regime 1: $p_T^{\text{cut}}/Q \gg e^{-\eta_{\text{cut}}}$ (standard jet veto resummation)

As usual, the scaling of the modes in the EFT follows from the nontrivial constraints imposed on emissions by the measurement. Soft emissions at central rapidities are always restricted by the jet veto. Collinear emissions with energy $\sim Q$ and rapidity η have a transverse momentum $\sim Qe^{-|\eta|}$ and are constrained by the measurement if $Qe^{-|\eta|} \sim p_T^{\text{cut}}$, which determines their scaling. Since $Qe^{-\eta_{\text{cut}}} \ll p_T^{\text{cut}}$, these collinear modes are parametrically

JHEP04(2019)142

not forward enough to be sensitive to the rapidity cut, such that the description of their dynamics is simply governed by the power counting in $p_T^{\rm cut}/Q$. The relevant EFT modes in this regime are thus the same as for a jet veto without any rapidity cut,

$$\begin{aligned} \text{soft:} \quad & p^\mu \sim \left(p_T^{\rm cut}, p_T^{\rm cut}, p_T^{\rm cut}\right), \\ n_a\text{-collinear:} \quad & p^\mu \sim \left(\frac{(p_T^{\rm cut})^2}{Q}, Q, p_T^{\rm cut}\right), \\ n_b\text{-collinear:} \quad & p^\mu \sim \left(Q, \frac{(p_T^{\rm cut})^2}{Q}, p_T^{\rm cut}\right). \end{aligned} \tag{2.4}$$

Here and below, we give the scaling of momenta in terms of light-cone components defined as (with $n \equiv n_a$, $\bar{n} \equiv n_b$),

$$p^\mu = \bar{n}\cdot p\,\frac{n^\mu}{2} + n\cdot p\,\frac{\bar{n}^\mu}{2} + p_\perp^\mu \equiv (n\cdot p, \bar{n}\cdot p, \vec{p}_\perp) \equiv (p^+, p^-, \vec{p}_\perp)\,. \tag{2.5}$$

In addition, there are the usual inclusive collinear modes that describe the initial protons at the scale $\Lambda_{\rm QCD}$, and which are not specific to our discussion here.

In principle, we can consider collinear emissions that are forward enough to resolve rapidities $|\eta| \sim \eta_{\rm cut}$,

$$\begin{aligned} n_a\text{-collinear } (\eta_{\rm cut}): \quad & p^\mu \sim \left(Qe^{-2\eta_{\rm cut}}, Q, Qe^{-\eta_{\rm cut}}\right), \\ n_b\text{-collinear } (\eta_{\rm cut}): \quad & p^\mu \sim \left(Q, Qe^{-2\eta_{\rm cut}}, Qe^{-\eta_{\rm cut}}\right). \end{aligned} \tag{2.6}$$

However, since $Qe^{-\eta_{\rm cut}} \ll p_T^{\rm cut}$, these emissions have too little transverse momentum to be affected by the jet veto, and are therefore unconstrained and integrated over without requiring additional modes in the EFT. To explicitly see that the $\eta_{\rm cut}$ dependence is power suppressed, note that the full jet-veto measurement for the collinear modes contains a θ function

$$\theta(\eta_{\rm cut} - |\eta|) = \theta(1 - e^{|\eta| - \eta_{\rm cut}}) = 1 + \mathcal{O}(Qe^{-\eta_{\rm cut}}/p_T^{\rm cut})\,, \tag{2.7}$$

which thus only induces power corrections in $Qe^{-\eta_{\rm cut}}/p_T^{\rm cut}$.

Therefore, at leading order in the power expansion,[1] we recover the factorization for the 0-jet cross section with $\eta_{\rm cut} = \infty$ [7, 8, 13],

$$\begin{aligned} \sigma_0(p_T^{\rm cut}, \eta_{\rm cut}, R, \Phi) = {} & H_\kappa(\Phi, \mu)\, B_a(p_T^{\rm cut}, R, \omega_a, \mu, \nu)\, B_b(p_T^{\rm cut}, R, \omega_b, \mu, \nu)\, S_\kappa(p_T^{\rm cut}, R, \mu, \nu) \\ & \times \left[1 + \mathcal{O}\Big(\frac{p_T^{\rm cut}}{Q}, \frac{Qe^{-\eta_{\rm cut}}}{p_T^{\rm cut}}, R^2\Big)\right]. \end{aligned} \tag{2.8}$$

The hard function H_κ contains the short-distance matrix element for producing a color-singlet final state and depends on the hard kinematic phase space Φ, which encodes e.g. the total rapidity Y and invariant mass Q of the color-singlet final state. The soft function S_κ encodes soft radiation restricted by $p_T^{\rm cut}$. The partonic channel is denoted by κ and is

[1] As discussed in refs. [8, 13], one formally needs to count $R \ll 1$ to avoid soft-collinear mixing terms of $\mathcal{O}(R^2)$. A detailed discussion of possible approaches to include them at $\mathcal{O}(\alpha_s^2)$ can be found in ref. [28].

JHEP04(2019)142

implicitly summed over (if necessary). The beam functions $B_{a,b}$ are forward proton matrix elements of collinear SCET fields and encode the perturbative collinear ISR constrained by $p_T^{\rm cut}$ as well as the unconstrained ISR below that scale down to the nonperturbative scale of the PDFs [4]. In eq. (2.8), they are evaluated at $\omega_{a,b} = Qe^{\pm Y}$. They are given by a convolution of perturbative matching coefficients $\mathcal{I}_{ij}$, which encode the $p_T^{\rm cut}$ constraint, and the standard inclusive quark and gluon PDFs f_j,

$$B_i(p_T^{\rm cut}, R, \omega, \mu, \nu) = \sum_j \int_x^1 \frac{\mathrm{d}z}{z}\, \mathcal{I}_{ij}(p_T^{\rm cut}, R, \omega, z, \mu, \nu)\, f_j\left(\frac{\omega}{zE_{\rm cm}}, \mu\right) \left[1 + \mathcal{O}\left(\frac{\Lambda_{\rm QCD}}{p_T^{\rm cut}}\right)\right]. \tag{2.9}$$

As discussed in detail in ref. [13], all logarithms of the ratio $p_T^{\rm cut}/Q$ in eq. (2.8) are resummed by evaluating each of the hard, beam, and soft functions at their characteristic virtuality and rapidity scales,

$$\mu_H \sim Q = \sqrt{\omega_a \omega_b}\,, \quad \mu_B \sim \mu_S \sim p_T^{\rm cut}\,, \quad \nu_B \sim Q\,, \quad \nu_S \sim p_T^{\rm cut}\,, \tag{2.10}$$

and evolving them to common scales μ, ν using renormalization group (RG) evolution. The power corrections in eq. (2.8) can be included at fixed order in α_s by matching the resummed result to the corresponding fixed-order result in full QCD. The $\mathcal{O}(Qe^{-\eta_{\rm cut}}/p_T^{\rm cut})$ corrections stop being suppressed for large Q, small $p_T^{\rm cut}$, or central $\eta_{\rm cut}$. In the next section, we show that they can be incorporated into the beam functions in eq. (2.9).

2.3 Regime 2: $p_T^{\rm cut}/Q \sim e^{-\eta_{\rm cut}}$ ($\eta_{\rm cut}$ dependent beam functions)

In this regime, the scaling of soft and collinear modes is unchanged from the previous case. However, the characteristic rapidity of the collinear modes now coincides parametrically with $\eta_{\rm cut}$, i.e.,

$$\begin{aligned}
\text{soft:} \quad & p^\mu \sim \left(p_T^{\rm cut}, p_T^{\rm cut}, p_T^{\rm cut}\right), \\
n_a\text{-collinear:} \quad & p^\mu \sim \left(\frac{(p_T^{\rm cut})^2}{Q}, Q, p_T^{\rm cut}\right) \sim \left(Qe^{-2\eta_{\rm cut}}, Q, Qe^{-\eta_{\rm cut}}\right), \\
n_b\text{-collinear:} \quad & p^\mu \sim \left(Q, \frac{(p_T^{\rm cut})^2}{Q}, p_T^{\rm cut}\right) \sim \left(Q, Qe^{-2\eta_{\rm cut}}, Qe^{-\eta_{\rm cut}}\right).
\end{aligned} \tag{2.11}$$

Thus, collinear emissions resolve the rapidity cut, and are constrained by the jet veto for $|\eta| < \eta_{\rm cut}$, while for $|\eta| > \eta_{\rm cut}$ they are unconstrained. As a result, the cross section factorizes at leading power as

$$\begin{aligned}
\sigma_0(p_T^{\rm cut}, \eta_{\rm cut}, R, \Phi) = {} & H_\kappa(\Phi, \mu)\, B_a(p_T^{\rm cut}, \eta_{\rm cut}, R, \omega_a, \mu, \nu)\, B_b(p_T^{\rm cut}, \eta_{\rm cut}, R, \omega_b, \mu, \nu) \\
& \times S_\kappa(p_T^{\rm cut}, \mu, \nu) \left[1 + \mathcal{O}\left(\frac{p_T^{\rm cut}}{Q}, e^{-\eta_{\rm cut}}, R^2\right)\right].
\end{aligned} \tag{2.12}$$

The beam functions now explicitly depend on both $p_T^{\rm cut}$ and $\eta_{\rm cut}$, while the hard and soft functions are unchanged (with their characteristic scales still given by eq. (2.10)). The RG consistency of the cross section fixes the anomalous dimensions of the beam function in

JHEP04(2019)142

terms of those for the soft and hard functions. Thus, the $\eta_{\rm cut}$ dependence cannot change the renormalization of the beam function, i.e.,

$$\begin{aligned}\mu\frac{\mathrm{d}}{\mathrm{d}\mu}\ln B_i(p_T^{\rm cut},\eta_{\rm cut},R,\omega,x,\mu,\nu) &= \gamma_B^i(\omega,\mu,\nu)\,,\\ \nu\frac{\mathrm{d}}{\mathrm{d}\nu}\ln B_i(p_T^{\rm cut},\eta_{\rm cut},R,\omega,x,\mu,\nu) &= \gamma_{\nu,B}^i(p_T^{\rm cut},R,\mu)\,,\end{aligned} \tag{2.13}$$

where the anomalous dimensions are the same as in the $\eta_{\rm cut}\to\infty$ limit [8, 13],

$$\begin{aligned}\gamma_B^i(\omega,\mu,\nu) &= 2\Gamma^i_{\rm cusp}[\alpha_s(\mu)]\,\ln\frac{\nu}{\omega}+\gamma_B^i[\alpha_s(\mu)]\,,\\ \gamma_{\nu,B}^i(p_T^{\rm cut},R,\mu) &= 2\eta_\Gamma^i(p_T^{\rm cut},\mu)+\gamma_{\nu,B}^i[\alpha_s(p_T^{\rm cut}),R]\,,\end{aligned} \tag{2.14}$$

and η_Γ^i in the resummed rapidity anomalous dimension is given by

$$\eta_\Gamma^i(\mu_0,\mu) = \int_{\mu_0}^{\mu}\frac{\mathrm{d}\mu'}{\mu'}\,\Gamma^i_{\rm cusp}[\alpha_s(\mu')]\,. \tag{2.15}$$

Hence, the $\eta_{\rm cut}$ effects do not affect the RG evolution itself, but only change the beam function boundary conditions, and therefore first appear at NLL′. The RG evolution between $\mu_B\sim p_T^{\rm cut}\sim Qe^{-\eta_{\rm cut}}$ and $\mu_H\sim Q$ now resums all large logarithms of $\mu_B/\mu_H\sim p_T^{\rm cut}/Q\sim e^{-\eta_{\rm cut}}$, while the beam function boundary condition now explicitly depends on the ratio $Qe^{-\eta_{\rm cut}}/p_T^{\rm cut}\sim\mathcal{O}(1)$, which in contrast to regime 1 is not power suppressed anymore.

In analogy to eq. (2.9) the beam functions can be factorized into collinear matching coefficients, which now also depend on $\eta_{\rm cut}$, and the PDFs. We write the matching coefficients as the sum of the usual $\eta_{\rm cut}$-independent matching coefficients plus a correction term that encodes the $\eta_{\rm cut}$ dependence,

$$\mathcal{I}_{ij}(p_T^{\rm cut},\eta_{\rm cut},R,\omega,z,\mu,\nu) = \mathcal{I}_{ij}(p_T^{\rm cut},R,\omega,z,\mu,\nu)+\Delta\mathcal{I}_{ij}(p_T^{\rm cut},\eta_{\rm cut},R,\omega,z,\mu,\nu)\,. \tag{2.16}$$

The $\eta_{\rm cut}$-independent $\mathcal{I}_{ij}$ are given in appendix A.2, and in the following we focus on the $\Delta\mathcal{I}_{ij}$.

Consistency between the cross sections in eqs. (2.8) and (2.12) implies that $\Delta\mathcal{I}_{ij}$ vanishes as $\eta_{\rm cut}\to\infty$. Specifically, defining

$$\zeta_{\rm cut}\equiv\omega e^{-\eta_{\rm cut}}/p_T^{\rm cut}\,, \tag{2.17}$$

the $\Delta\mathcal{I}_{ij}$ scale like

$$\Delta\mathcal{I}_{ij}\big(p_T^{\rm cut},\eta_{\rm cut},R,\omega,z,\mu,\nu\big)\sim\mathcal{O}(\zeta_{\rm cut})\qquad\text{for }\zeta_{\rm cut}\to 0\,, \tag{2.18}$$

which is simply the statement from the previous subsection that the $\eta_{\rm cut}$ effects are power suppressed in $\zeta_{\rm cut}$ for $\zeta_{\rm cut}\ll 1$.

In fact, $\Delta\mathcal{I}_{ij}$ vanishes altogether for $z>\zeta_{\rm cut}/(1+\zeta_{\rm cut})$, which can be seen from purely kinematic considerations as follows: for the n-collinear sector the term $\Delta\mathcal{I}_{ij}$ accounts for the case where at least one jet with $p_T^{\rm jet}\geq p_T^{\rm cut}$ and $\eta_{\rm jet}\geq\eta_{\rm cut}$ is reconstructed (and no

JHEP04(2019)142

jet with $\eta_{\text{jet}} < \eta_{\text{cut}}$). For $R \ll 1$ all radiation in this jet has $\eta \geq \eta_{\text{cut}}$, as well. Thus, contributions to $\Delta\mathcal{I}_{ij}$ can only appear if

$$p_T^{\text{cut}} \leq |\vec{p}_T^{\,\text{jet}}| \leq \sum_{k\in\text{jets}} |\vec{p}_{T,k}| = \sum_{k\in\text{jets}} p_k^- e^{-\eta_k}\,, \tag{2.19}$$

where the second equality follows from the jets being massless for $R \ll 1$. Rewriting this in terms of momentum fractions $p_k^- = z_k\, P_n^- = z_k\,\omega/z$ yields, with $\sum_k z_k + z = 1$ and P_n^- the momentum of the initial state proton,

$$p_T^{\text{cut}} \leq \sum_{k\in\text{jets}} \frac{z_k}{z}\,\omega e^{-\eta_k} \leq \frac{1-z}{z}\,\omega e^{-\eta_{\text{cut}}}\,. \tag{2.20}$$

The second inequality follows from all reconstructed n-collinear jets having $\eta_k > \eta_{\text{cut}}$. This implies that eq. (2.18) is trivially satisfied since the domain of integration in z scales as $x \leq z \lesssim \zeta_{\text{cut}}$. Hence $\Delta\mathcal{I}_{ij}$ is parametrically important for $\zeta_{\text{cut}} \sim z \sim 1$, but vanishes in the threshold limit $z \to 1$. This leads to an additional numerical suppression due to the falloff of the PDFs towards larger partonic momentum fractions.

The RGE of $\Delta\mathcal{I}_{ij}$ follows from the beam-function RGE eq. (2.13) and the analogue of the matching onto the PDFs in eq. (2.9). It is given by (with the remaining arguments of $\Delta\mathcal{I}_{ij}$ understood)

$$\begin{aligned}
\mu\frac{\mathrm{d}}{\mathrm{d}\mu}\Delta\mathcal{I}_{ij}(z,\mu,\nu) &= \gamma_B^i(\omega,\mu,\nu)\,\Delta\mathcal{I}_{ij}(z,\mu,\nu) - \sum_k \Delta\mathcal{I}_{ik}(z,\mu,\nu)\otimes_z 2P_{kj}[\alpha_s(\mu),z]\,,\\
\nu\frac{\mathrm{d}}{\mathrm{d}\nu}\Delta\mathcal{I}_{ij}(z,\mu,\nu) &= \gamma_{\nu,B}^i(p_T^{\text{cut}},R,\mu)\,\Delta\mathcal{I}_{ij}(z,\mu,\nu)\,.
\end{aligned} \tag{2.21}$$

The Mellin convolution $\otimes_z$ is defined as

$$g(z)\otimes_z h(z) = \int_z^1 \frac{\mathrm{d}\xi}{\xi}\, g(\xi)\, h\Big(\frac{z}{\xi}\Big)\,, \tag{2.22}$$

and $2P_{ij}(\alpha_s,z)$ is the standard PDF anomalous dimension with respect to μ,

$$\mu\frac{\mathrm{d}}{\mathrm{d}\mu} f_i(x,\mu) = \sum_j \int_x^1 \frac{\mathrm{d}z}{z}\, 2P_{ij}[\alpha_s(\mu),z]\, f_j\Big(\frac{x}{z},\mu\Big)\,. \tag{2.23}$$

Note that the RGE in eq. (2.21) does not mix $\Delta\mathcal{I}_{ij}$ with $\mathcal{I}_{ij}$ and therefore does not change the ζ_{cut} scaling in eq. (2.18). Solving eq. (2.21) order by order in perturbation theory, we find the following structure through two loops:

$$\begin{aligned}
\Delta\mathcal{I}_{ij}(z) &= \frac{\alpha_s(\mu)}{4\pi}\,\Delta\mathcal{I}_{ij}^{(1)}(z) + \frac{\alpha_s^2(\mu)}{(4\pi)^2}\,\Delta\mathcal{I}_{ij}^{(2)}(z) + \mathcal{O}(\alpha_s^3)\,,\\
\Delta\mathcal{I}_{ij}^{(1)}(z) &= \Delta I_{ij}^{(1)}\left(\frac{\omega e^{-\eta_{\text{cut}}}}{p_T^{\text{cut}}},z\right),\\
\Delta\mathcal{I}_{ij}^{(2)}(z) &= \ln\frac{\mu}{p_T^{\text{cut}}}\left[2\Gamma_0^i\ln\frac{\nu}{\omega} + 2\beta_0 + \gamma_{B\,0}^i\right]\Delta I_{ij}^{(1)}\left(\frac{\omega e^{-\eta_{\text{cut}}}}{p_T^{\text{cut}}},z\right)\\
&\quad - 2\ln\frac{\mu}{p_T^{\text{cut}}}\sum_k \Delta I_{ik}^{(1)}\left(\frac{\omega e^{-\eta_{\text{cut}}}}{p_T^{\text{cut}}},z\right)\otimes_z P_{kj}^{(0)}(z) + \Delta I_{ij}^{(2)}\left(\frac{\omega e^{-\eta_{\text{cut}}}}{p_T^{\text{cut}}},R,z\right),
\end{aligned} \tag{2.24}$$

JHEP04(2019)142

where $\Delta I_{ij}^{(n)}$ is the boundary condition of the RGE at $\mu = p_T^{\text{cut}}$, $\nu = \omega$, and the required anomalous dimension coefficients are collected in appendix A.1. By dimensional analysis and boost invariance, $\Delta I_{ij}^{(n)}$ can only depend on $\zeta_{\text{cut}} = \omega e^{-\eta_{\text{cut}}}/p_T^{\text{cut}}$ in addition to R and z.

In appendix A.3 we determine the one-loop contribution $\Delta I_{ij}^{(1)}$, which has the simple form

$$\Delta I_{ij}^{(1)}(\zeta_{\text{cut}}, z) = \theta\left(\frac{\zeta_{\text{cut}}}{1+\zeta_{\text{cut}}} - z\right) 2P_{ij}^{(0)}(z) \ln\frac{\zeta_{\text{cut}}(1-z)}{z}\,, \tag{2.25}$$

with the one-loop splitting functions $P_{ij}^{(0)}(z)$ as given in eq. (A.6). The correction vanishes at the kinematic threshold encoded in the overall θ-function, which also cuts off the singular distributions in $P_{ij}^{(0)}(z)$ at $z = 1$. The Mellin convolutions of $\Delta I_{ik}^{(1)} \otimes_z P_{kj}^{(0)}$ appearing in the coefficient of $\ln(\mu/p_T^{\text{cut}})$ in $\Delta\mathcal{I}_{ij}^{(2)}(z)$ are given in appendix A.6.

While the computation of the full two-loop contribution $\Delta I_{ij}^{(2)}$ is beyond the scope of this paper, we analytically compute its leading contribution in the small-R limit, which contains a clustering logarithm of R. We write the full two-loop result as

$$\Delta I_{ij}^{(2)}(\zeta_{\text{cut}}, R, z) = \ln R\, \Delta I_{ij}^{(2,\ln R)}(\zeta_{\text{cut}}, z) + \Delta I_{ij}^{(2,c)}(\zeta_{\text{cut}}, z) + \mathcal{O}(R^2)\,. \tag{2.26}$$

In the limit $R \ll 1$, we exploit that for the emission of two close-by collinear partons with relative rapidity $\Delta\eta \sim R$, the collinear matrix element factorizes into two sequential collinear splittings at the scale $\mu \sim p_T^{\text{cut}}$ and $\mu \sim p_T^{\text{cut}} R$, respectively. This allows us to evaluate the coefficient of $\ln R$ in a generic two-loop beam function as a convolution of a primary on-shell emission and (the anomalous dimension of) the semi-inclusive jet function of ref. [36]. Specifically, for the case of $\Delta I_{ij}^{(2)}$ we find

$$\Delta I_{ij}^{(2,\ln R)}(\zeta_{\text{cut}}, z) = \theta\left(\frac{\zeta_{\text{cut}}}{1+\zeta_{\text{cut}}} - z\right) 2P_{ij}^{(0)}(z) \left[\theta\left(z - \frac{\zeta_{\text{cut}}}{2+\zeta_{\text{cut}}}\right) c_{ij}^{R,\text{cut}}\left(\frac{z}{\zeta_{\text{cut}}(1-z)}\right) - c_{ij}^{R}\right], \tag{2.27}$$

where the coefficient functions $c_{ij}^{R,\text{cut}}$ are given by

$$\begin{aligned} c_{gg}^{R,\text{cut}}(x) = c_{qq}^{R,\text{cut}}(x) &= -2\int_{1/2}^{x}\frac{\mathrm{d}z}{z}\int_{1/2}^{z}\mathrm{d}z_J\left[P_{gg}^{(0)}(z_J) + 2n_f P_{qg}^{(0)}(z_J)\right], \\ c_{gq}^{R,\text{cut}}(x) = c_{qg}^{R,\text{cut}}(x) &= -2\int_{1/2}^{x}\frac{\mathrm{d}z}{z}\int_{1/2}^{z}\mathrm{d}z_J\left[P_{qq}^{(0)}(z_J) + P_{gq}^{(0)}(z_J)\right], \end{aligned} \tag{2.28}$$

depending on whether the primary emission we split is a gluon (first line) or a quark (second line). Their explicit expressions read

$$\begin{aligned} c_{gg}^{R,\text{cut}}(x) = c_{qq}^{R,\text{cut}}(x) &= 2C_A\left[\frac{5}{8} + \frac{\pi^2}{3} - 3x + \frac{9}{2}x^2 - 2x^3 - 2\ln^2 x - 4\,\text{Li}_2(x)\right] \\ &\quad + 2\beta_0\left[-\frac{29}{24} - \ln 2 + 3x - \frac{3}{2}x^2 + \frac{2}{3}x^3 - \ln x\right], \\ c_{gq}^{R,\text{cut}}(x) = c_{qg}^{R,\text{cut}}(x) &= 2C_F\left[-3 + \frac{\pi^2}{3} - 3\ln 2 + 6x - 3\ln x - 2\ln^2 x - 4\,\text{Li}_2(x)\right]. \end{aligned} \tag{2.29}$$

JHEP04(2019)142

The coefficients c_{ij}^R in eq. (2.27) are the (in principle known) coefficients of $\ln R$ in the η_{cut}-independent two-loop beam function [13, 19], which we also verified.[2] They satisfy

$$c_{ij}^R = \lim_{x\to 1} c_{ij}^{R,\text{cut}}(x)\,, \tag{2.30}$$

and are given by

$$\begin{aligned} c_{gg}^R &= c_{qq}^R = \frac{1}{4}\left[\left(1-\frac{8\pi^2}{3}\right)C_A + \left(\frac{23}{3}-8\ln 2\right)\beta_0\right], \\ c_{qg}^R &= c_{gq}^R = 2C_F\left(3-\frac{\pi^2}{3}-3\ln 2\right). \end{aligned} \tag{2.31}$$

Our general setup for computing the small-R clustering contributions implies that the coefficient of the $\ln R$ terms of the two-loop rapidity anomalous dimension must be equal to $c_{gg}^R = c_{qq}^R$, in agreement with the corresponding result given in refs. [8, 13]. In addition, it also applies to the leading $\ln^2 R$ and $\ln R$ terms in the beam functions for rapidity dependent jet vetoes in ref. [28], with which we agree as well.

The R-independent term $\Delta I_{ik}^{(2,c)}(\zeta_{\text{cut}}, z)$ and the $\mathcal{O}(R^2)$ terms in eq. (2.26) are currently unknown. Their contribution to the cross section can in principle be obtained numerically from the singular limit of the full-theory calculation at $\mathcal{O}(\alpha_s^2)$, as was done for the corresponding η_{cut}-independent pieces in ref. [13].

Numerical validation. To validate our results numerically and highlight the differences in the singular behavior for regimes 1 and 2, we consider the fixed $\mathcal{O}(\alpha_s)$ p_T^{jet} spectrum, $\mathrm{d}\sigma/\mathrm{d}p_T^{\text{jet}}$, where p_T^{jet} is the transverse momentum of the leading jet within $|\eta_{\text{jet}}| < \eta_{\text{cut}}$. Its relation to the jet veto cross section with a jet rapidity cut is simply

$$\sigma_0(p_T^{\text{cut}}, \eta_{\text{cut}}, R) = \int_0^{p_T^{\text{cut}}} \mathrm{d}p_T^{\text{jet}}\, \frac{\mathrm{d}\sigma(\eta_{\text{cut}}, R)}{\mathrm{d}p_T^{\text{jet}}}\,. \tag{2.32}$$

At leading power in p_T^{jet}/Q, we obtain it by taking the derivative with respect to p_T^{cut} of either eq. (2.12), retaining the exact dependence on η_{cut} in the beam functions (regime 2), or of eq. (2.8), incurring power corrections in $Qe^{-\eta_{\text{cut}}}/p_T^{\text{jet}}$ (regime 1). The numerical results for all singular spectra are obtained with the help of `SCETlib` [37]. The $\mathcal{O}(\alpha_s)$ spectra in full QCD are obtained from `MCFM 8.0` [38–40].

As representative gluon-induced processes, we consider gluon-fusion Higgs production $gg \to H$ at $m_H = 125\,\text{GeV}$ in the infinite top-mass limit, rescaled with the exact LO top-mass dependence for $m_t = 172.5\,\text{GeV}$ (rEFT). In addition, we consider gluon fusion to a hypothetical heavy color-singlet scalar X, $gg \to X$, mediated by the contact operator

$$\mathcal{L}_{\text{eff}} = -\frac{C_X}{\Lambda}\,\alpha_s\, G_{\mu\nu}^a G^{a,\mu\nu} X\,. \tag{2.33}$$

[2] The coefficient of the c_{gq}^R contribution in eq. (39) of ref. [13] has a typo, missing an overall factor of 2. We also find that the C_A term of the coefficient c_{qq}^R in eq. (9) of ref. [19] misses a factor of 1/2 compared to ref. [13] and our result.

JHEP04(2019)142

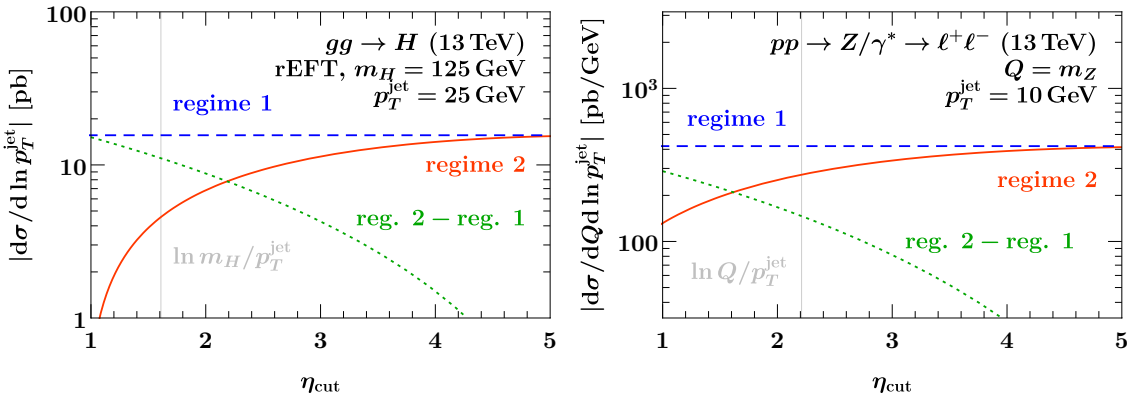

Figure 3. Comparison of the singular contributions to the fixed $\mathcal{O}(\alpha_s)$ (LO_1) $p_T^{\rm jet}$ spectrum for $gg \to H$ (left) and Drell-Yan (right). The orange solid lines show the singular contributions in regime 2 with $\eta_{\rm cut}$ dependent beam functions. The dashed blue lines show the singular contributions in regime 1 in the limit $\eta_{\rm cut} = \infty$, $p_T^{\rm cut} \gg Qe^{-\eta_{\rm cut}}$. Their difference, shown by the dotted green lines, correctly scales as a power in $Qe^{-\eta_{\rm cut}}/p_T^{\rm jet}$. The vertical lines indicate the point $p_T^{\rm jet} = Qe^{-\eta_{\rm cut}}$.

We always choose $m_X = 1\,\mathrm{TeV}$, $\Lambda = 1\,\mathrm{TeV}$, and divide the cross section by $|C_X|^2$. To the order we are working, this is equivalent to setting $C_X \equiv 1$, since C_X only starts to run at $\mathcal{O}(\alpha_s^2)$.[3] For quark-induced processes we consider Drell-Yan $pp \to Z/\gamma^* \to \ell^+\ell^-$ at the Z pole ($Q = m_Z$) and at $Q = 1\,\mathrm{TeV}$, where $Q = m_{\ell\ell}$ is the invariant mass of the lepton pair. Here we set all scales to $\mu_{\rm FO} = m_H$, m_X, or Q, respectively. We use `PDF4LHC_nnlo_100` [45–50] NNLO PDFs with $\alpha_s(m_Z) = 0.118$ throughout.

In figure 3, we compare the regime 2 and regime 1 leading-power (singular) results for $\mathrm{d}\sigma/\mathrm{d}p_T^{\rm jet}$ at fixed $p_T^{\rm jet}$ as a function of $\eta_{\rm cut}$ for $gg \to H$ and Drell-Yan. The regime 1 result (dashed blue) does not depend on $\eta_{\rm cut}$, while the regime 2 result (solid orange) decreases as $\eta_{\rm cut}$ becomes more central. The difference between the two (dotted green) has the expected behavior, vanishing as $Qe^{-\eta_{\rm cut}}/p_T^{\rm jet}$ for $\eta_{\rm cut} \to \infty$. We observe that regime 1 is applicable beyond $\eta_{\rm cut} \gtrsim 4$, where the difference to regime 2 is suppressed by an order of magnitude.

Another check is provided by comparing the regime 1 and regime 2 singular results to the full QCD result, which is shown in figures 4 and 5 for gluon-fusion and Drell-Yan. For $\eta_{\rm cut} = 2.5$ (left panels), it is clear that regime 1 (dashed gray) fails to describe the singular limit of full QCD, with their difference (dotted gray) diverging for $p_T^{\rm jet} \to 0$ like an inverse power of $p_T^{\rm jet}$ as expected. While the singular mismatch becomes less pronounced for $\eta_{\rm cut} = 4.5$ (right panels), the uncanceled singular contributions are still clearly visible in the difference. On the other hand, regime 2 (dashed blue) correctly reproduces the singular limit $p_T^{\rm jet} \to 0$, with the difference (dotted green) vanishing like a power of $p_T^{\rm jet}$ as it must. This provides a strong check of the intricate $p_T^{\rm cut}$ dependence encoded in our $\mathcal{O}(\alpha_s)$ results for $\Delta\mathcal{I}_{ij}$. (The power corrections in $e^{-\eta_{\rm cut}}$, which are present in regime 2, drop out when taking the derivative of the fixed-order cumulant with respect to $p_T^{\rm cut}$.)

[3] In `MCFM 8.0` we mock up this process using a standard-model Higgs with $m_H = 1\,\mathrm{TeV}$ and manually account for the nonzero one-loop contribution from integrating out the top quark in the SM, which differs from our choice of $C_X = 1 + \mathcal{O}(\alpha_s^2)$ for the effective coupling of X to gluons. We also checked the results against the native $gg \to X$ support of `SusHi 1.6.1` [41–44].

JHEP04(2019)142

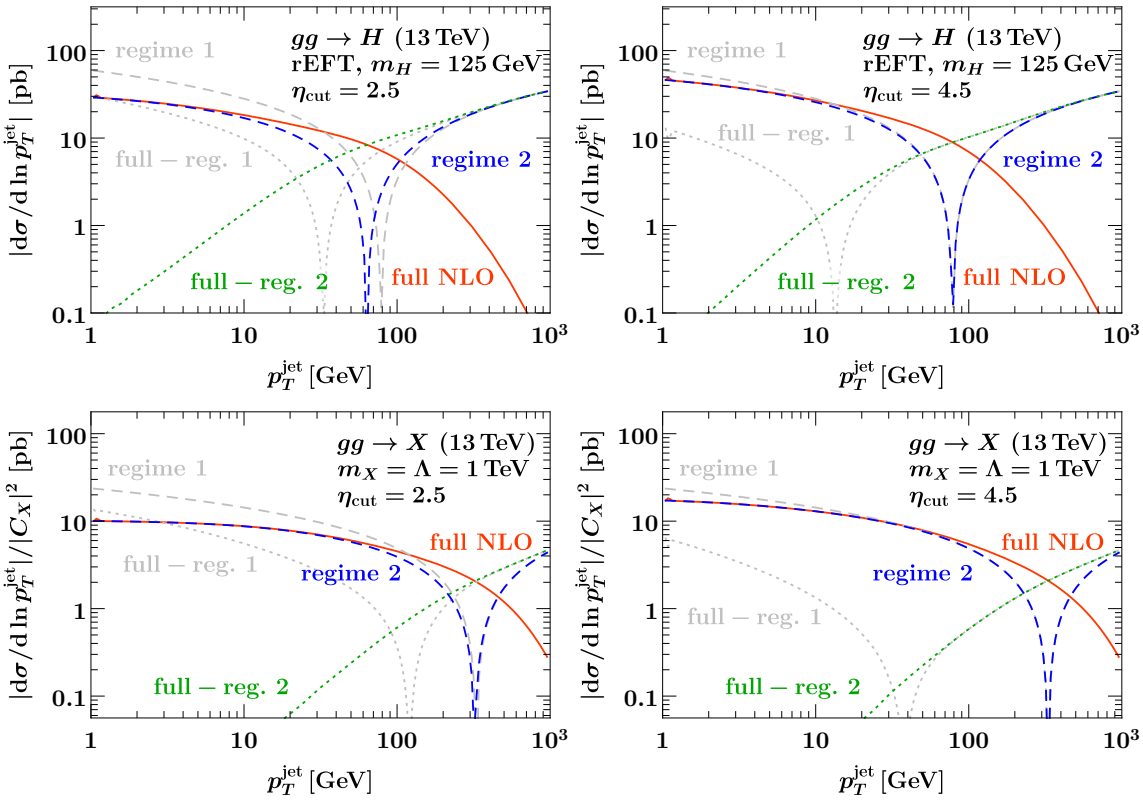

Figure 4. Comparison of singular and nonsingular contributions to the fixed $\mathcal{O}(\alpha_s)$ (LO_1) $p_T^{\rm jet}$ spectrum with rapidity cut $|\eta_{\rm jet}| < \eta_{\rm cut}$ for $gg \to H$ (top row) and $gg \to X$ (bottom row), $\eta_{\rm cut} = 2.5$ (left) and $\eta_{\rm cut} = 4.5$ (right). The orange solid lines show the full results, the dashed blue lines the regime 2 results with $\eta_{\rm cut}$ dependent beam functions, and the dotted green lines their difference. The dashed and dotted gray lines show the corresponding regime 1 results, which do not describe the singular behavior of the full cross section for finite $\eta_{\rm cut}$.

Note that at $m_X = 1\,\mathrm{TeV}$ or $Q = 1\,\mathrm{TeV}$, the fixed-order spectrum is completely dominated by the rapidity-cut dependent singular result up to $p_T^{\rm jet} \lesssim 100\,\mathrm{GeV}$. Hence, the resummation should provide a significant improvement over the fixed-order result for typical $p_T^{\rm cut} \sim 50\,\mathrm{GeV}$, which we will indeed find in section 4.

2.4 Regime 3: $p_T^{\rm cut}/Q \ll e^{-\eta_{\rm cut}}$ (collinear NGLs)

The hierarchy $p_T^{\rm cut} \ll Q e^{-\eta_{\rm cut}}$ (with $e^{-\eta_{\rm cut}} \ll 1$) exhibits different features than the regimes discussed before. The typical transverse momentum for emissions with $|\eta| > \eta_{\rm cut}$ is parametrically $Q e^{-|\eta|}$, indicated by the horizontal gray line in figure 2, which is now much larger than for the strongly constrained emissions at $|\eta| < \eta_{\rm cut}$. While the soft modes at central rapidities are not affected, there are now two types of collinear modes at forward rapidities with $|\eta| \sim \eta_{\rm cut}$,

$$\begin{aligned} n_a\text{-collinear:} \quad & p^\mu \sim Q\left(e^{-2\eta_{\rm cut}}, 1, e^{-\eta_{\rm cut}}\right), \\ n_a\text{-soft-collinear:} \quad & p^\mu \sim \left(p_T^{\rm cut} e^{-\eta_{\rm cut}}, p_T^{\rm cut} e^{\eta_{\rm cut}}, p_T^{\rm cut}\right) = p_T^{\rm cut} e^{\eta_{\rm cut}}\left(e^{-2\eta_{\rm cut}}, 1, e^{-\eta_{\rm cut}}\right), \end{aligned} \tag{2.34}$$

and analogously for the n_b-collinear sector.

JHEP04(2019)142

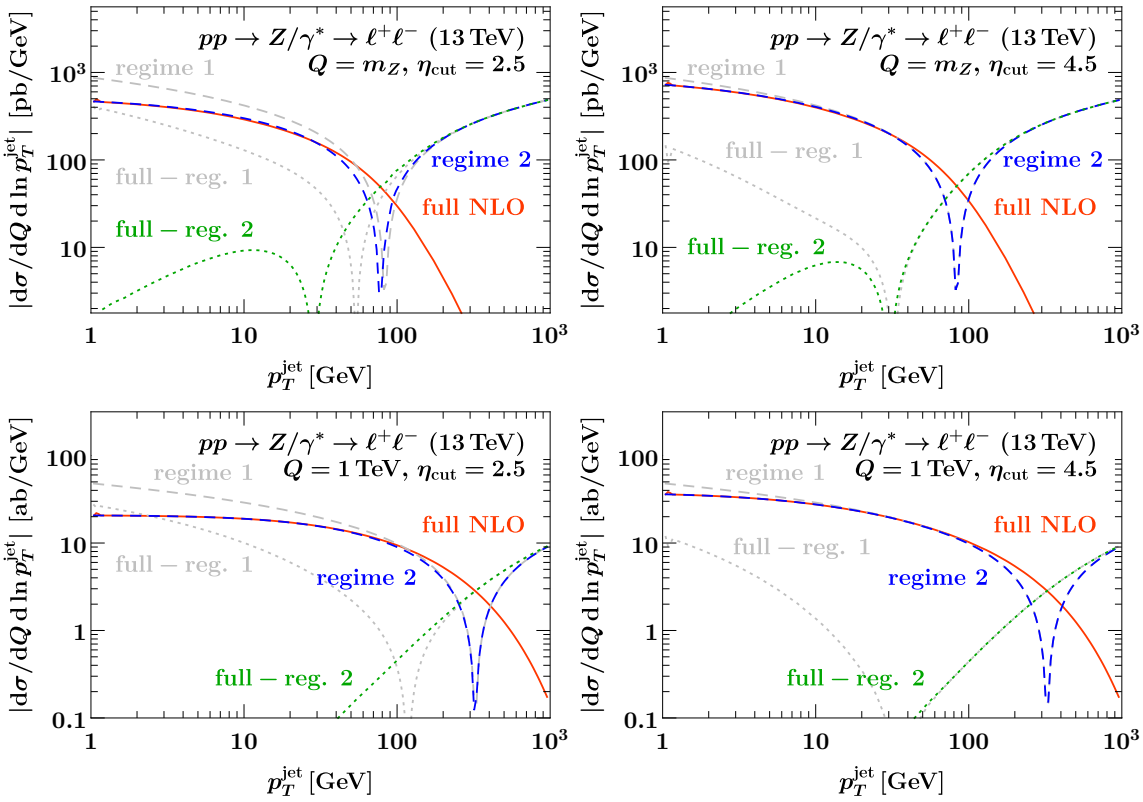

Figure 5. Comparison of singular and nonsingular contributions to the fixed $\mathcal{O}(\alpha_s)$ (LO_1) $p_T^{\rm jet}$ spectrum with rapidity cut $|\eta_{\rm jet}| < \eta_{\rm cut}$ for Drell-Yan at $Q = m_Z$ (top row) and $Q = 1\,\mathrm{TeV}$ (bottom row), $\eta_{\rm cut} = 2.5$ (left) and $\eta_{\rm cut} = 4.5$ (right). The meaning of the curves are as in figure 4.

The collinear and soft-collinear modes have the same angular resolution and only differ in their energy. This makes their all-order factorization challenging and leads to the appearance of nonglobal logarithms $\ln(Qe^{-\eta_{\rm cut}}/p_T^{\rm cut})$ starting at $\mathcal{O}(\alpha_s^2)$. Their factorization and resummation requires the marginalization over all possible configurations of energetic collinear emissions, involving soft-collinear matrix elements with a separate Wilson line along each individual energetic collinear emission, see e.g. refs. [51–54].

Since this regime has no immediate phenomenological relevance, we will not carry out this complete procedure but restrict ourselves to the configuration with soft-collinear Wilson lines along n and $\bar{n}$, i.e, along the two main collinear emitters. This is sufficient for the LL resummation, for isolating the nonglobal effects, and for discussing the relation to the other regimes. Our discussion here is in close analogy to the regime 3 in the factorization of the exclusive jet mass spectrum with small jet radius R in ref. [55], where the rapidity cut $e^{-\eta_{\rm cut}}$ here takes the role of R there.[4]

[4]The main difference is that here, emissions for $|\eta| < \eta_{\rm cut}$ are constrained by their p_T relative to the same collinear (beam) direction. In the jet mass case, emissions outside the jet are not constrained by their p_T relative to the same collinear (jet) direction (but also relative to the beam direction).

JHEP04(2019)142

The factorized cross section takes the form

$$\sigma_0(p_T^{\text{cut}},\eta_{\text{cut}},R,\Phi) = H_\kappa(\Phi,\mu)\,\mathcal{B}_a(p_T^{\text{cut}},\eta_{\text{cut}},R,\omega_a,\mu,\nu)\,\mathcal{B}_b(p_T^{\text{cut}},\eta_{\text{cut}},R,\omega_b,\mu,\nu) \times S_\kappa(p_T^{\text{cut}},R,\mu,\nu)\,\left[1+\mathcal{O}\left(\frac{p_T^{\text{cut}}}{Qe^{-\eta_{\text{cut}}}},e^{-\eta_{\text{cut}}},R^2\right)\right]. \tag{2.35}$$

The initial-state collinear functions $\mathcal{B}_i$ encode the contributions of both soft-collinear and energetic collinear modes. They are related to the η_{cut} dependent beam functions B_i in eq. (2.12) by an expansion in the limit $p_T^{\text{cut}}/(\omega e^{-\eta_{\text{cut}}}) \ll 1$,

$$B_i(p_T^{\text{cut}},\eta_{\text{cut}},R,\omega,\mu,\nu) = \mathcal{B}_i(p_T^{\text{cut}},\eta_{\text{cut}},R,\omega,\mu,\nu)\left[1+\mathcal{O}\left(\frac{p_T^{\text{cut}}}{\omega e^{-\eta_{\text{cut}}}}\right)\right]. \tag{2.36}$$

Without further factorization, $\mathcal{B}_i$ contains large unresummed Sudakov double logarithms $\alpha_s^n \ln^{2n}(p_T^{\text{cut}}/\omega e^{-\eta_{\text{cut}}})$. To resum the leading double logarithms, we can decompose $\mathcal{B}_i$ as

$$\mathcal{B}_i(p_T^{\text{cut}},\eta_{\text{cut}},R,\omega,\mu,\nu) = B_i^{(\text{cut})}(\eta_{\text{cut}},\omega,\mu)\,\mathcal{S}_i^{(\text{cut})}(p_T^{\text{cut}},\eta_{\text{cut}},R,\mu,\nu) \times\left[1+\mathcal{B}_i^{(\text{NG})}\left(\frac{p_T^{\text{cut}}}{\omega e^{-\eta_{\text{cut}}}},\omega,R\right)\right]. \tag{2.37}$$

The function $B_i^{(\text{cut})}$ mainly describes contributions from the energetic collinear modes. It was dubbed "unmeasured" beam function in refs. [33, 34], in analogy to the unmeasured jet function [56]. At one loop its matching coefficients account for an energetic collinear emission with $|\eta| > \eta_{\text{cut}}$. They are calculated in appendix A.3 and read

$$\begin{aligned}
\mathcal{I}_{gg}^{(\text{cut})}(\eta_{\text{cut}},\omega,z,\mu) &= \delta(1-z) + \frac{\alpha_s(\mu)\,C_A}{4\pi}\left[\delta(1-z)\left(4\ln^2\frac{\omega e^{-\eta_{\text{cut}}}}{\mu}-\frac{\pi^2}{6}\right)\right.\\
&\quad\left.+4P_{gg}(z)\ln\frac{\omega e^{-\eta_{\text{cut}}}}{\mu\,z}+8\mathcal{L}_1(1-z)+8\Big(\frac{1}{z}-2+z-z^2\Big)\ln(1-z)\right]\\
&\quad+\mathcal{O}(\alpha_s^2)\,,\\
\mathcal{I}_{gq}^{(\text{cut})}(\eta_{\text{cut}},\omega,z,\mu) &= \frac{\alpha_s(\mu)\,C_F}{4\pi}\left[4P_{gq}(z)\ln\frac{\omega e^{-\eta_{\text{cut}}}(1-z)}{\mu\,z}+2z\right]+\mathcal{O}(\alpha_s^2)\,,\\
\mathcal{I}_{qq}^{(\text{cut})}(\eta_{\text{cut}},\omega,z,\mu) &= \delta(1-z) + \frac{\alpha_s(\mu)\,C_F}{4\pi}\left[\delta(1-z)\left(4\ln^2\frac{\omega e^{-\eta_{\text{cut}}}}{\mu}-6\ln\frac{\omega e^{-\eta_{\text{cut}}}}{\mu}-\frac{\pi^2}{6}\right)\right.\\
&\quad\left.+4P_{qq}(z)\ln\frac{\omega e^{-\eta_{\text{cut}}}}{\mu\,z}+8\mathcal{L}_1(1-z)-4(1+z)\ln(1-z)+2(1-z)\right]\\
&\quad+\mathcal{O}(\alpha_s^2)\,,\\
\mathcal{I}_{qg}^{(\text{cut})}(\eta_{\text{cut}},\omega,z,\mu) &= \frac{\alpha_s(\mu)\,T_F}{4\pi}\left[4P_{qg}(z)\ln\frac{\omega e^{-\eta_{\text{cut}}}(1-z)}{\mu\,z}+4z(1-z)\right]+\mathcal{O}(\alpha_s^2)\,,
\end{aligned} \tag{2.38}$$

where $\mathcal{L}_n(1-z) \equiv [\ln^n(1-z)/(1-z)]_+$, $P_{ij}(z)$ are the color-stripped LO splitting functions given in eq. (A.7), and the flavor structure is trivial,

$$\mathcal{I}_{\bar{q}_i\bar{q}_j}^{(\text{cut})} = \mathcal{I}_{q_iq_j}^{(\text{cut})} = \delta_{ij}\mathcal{I}_{qq}^{(\text{cut})}+\mathcal{O}(\alpha_s^2)\,, \qquad \mathcal{I}_{q_i\bar{q}_j}^{(\text{cut})} = \mathcal{I}_{\bar{q}_iq_j}^{(\text{cut})} = \mathcal{O}(\alpha_s^2)\,. \tag{2.39}$$

As argued in ref. [33] the results are directly related to the matching coefficients for fragmenting jet functions in ref. [57].

JHEP04(2019)142

The function $\mathcal{S}_i^{(\mathrm{cut})}$ in eq. (2.37) mainly describes contributions from soft-collinear modes. At one loop it accounts for a soft-collinear emission that couples eikonally to the incoming collinear parton i. The emission is constrained to $p_T < p_T^{\mathrm{cut}}$ for $|\eta| < \eta_{\mathrm{cut}}$ by the jet veto, and is unconstrained for $|\eta| > \eta_{\mathrm{cut}}$. Using the η regulator [58, 59] it is given by (see appendix A.4)

$$\begin{aligned}
\mathcal{S}_i^{(\mathrm{cut})}(p_T^{\mathrm{cut}}, \eta_{\mathrm{cut}}, R, \mu, \nu) &= 1 + \frac{\alpha_s(\mu)}{4\pi}\,\mathcal{S}_i^{(\mathrm{cut},1)} + \frac{\alpha_s^2(\mu)}{(4\pi)^2}\,\mathcal{S}^{(\mathrm{cut},2)} + \mathcal{O}(\alpha_s^3)\,, \\
\mathcal{S}_i^{(\mathrm{cut},1)}(p_T^{\mathrm{cut}}, \eta_{\mathrm{cut}}, R, \mu, \nu) &= C_i\left(4\ln^2\frac{p_T^{\mathrm{cut}}}{\mu} - 8\ln\frac{p_T^{\mathrm{cut}}}{\mu}\ln\frac{\nu e^{-\eta_{\mathrm{cut}}}}{\mu} + \frac{\pi^2}{6}\right),
\end{aligned} \tag{2.40}$$

where $C_i = C_F$ for an incoming quark or antiquark and C_A for an incoming gluon. We checked explicitly that the above results obey the consistency constraint in eq. (2.36). For this purpose, one has to note that eq. (2.25) becomes distribution valued in $(1-z)$ when taking the limit $\zeta_{\mathrm{cut}} \gg 1$.

At two loops $\mathcal{S}_i^{(\mathrm{cut})}$ contains a $\ln R$ enhanced term. Focusing on the constant terms not predicted by the RG evolution, we have

$$\mathcal{S}_i^{(\mathrm{cut},2)}(p_T^{\mathrm{cut}}, \eta_{\mathrm{cut}}, R, \mu = p_T^{\mathrm{cut}}, \nu = \mu e^{\eta_{\mathrm{cut}}}) = \ln R\,\mathcal{S}_i^{(\mathrm{cut},2,\ln R)} + \mathcal{S}_i^{(\mathrm{cut},2,c)} + \mathcal{O}(R^2)\,, \tag{2.41}$$

with $\mathcal{S}_i^{(\mathrm{cut},2,c)}$ an unknown two-loop constant. The coefficient of $\ln R$ is obtained by expanding the $\ln R$ coefficient in the η_{cut} dependent beam function [see eqs. (2.27) and (A.21)] to leading power in $1/\zeta_{\mathrm{cut}}$. In the limit $\zeta_{\mathrm{cut}} \gg 1$, the sum $I_{ij}^{(2,\ln R)} + \Delta I_{ij}^{(2,\ln R)}$ becomes proportional to $\delta(1-z)$, as the arguments of both θ-functions in eq. (2.27) approach $z = 1$. The coefficient of $\delta(1-z)$ is then given by the $\zeta_{\mathrm{cut}} \to \infty$ limit of the integral of $\Delta I_{ij}^{(2,\ln R)}$, which vanishes for $i \neq j$ and for $i = j$ leaves

$$\begin{aligned}
\mathcal{S}_i^{(\mathrm{cut},2,\ln R)} &= 8C_i \int_{1/2}^1 \frac{\mathrm{d}x}{x} c_{ii}^{R,\mathrm{cut}}(x) \\
&= C_i\left\{C_A\left[\frac{1622}{27} - \frac{548}{9}\ln 2 - \frac{88}{3}\ln^2 2 - 8\zeta_3\right] + n_f T_F\left[-\frac{652}{27} + \frac{232}{9}\ln 2 + \frac{32}{3}\ln^2 2\right]\right\}.
\end{aligned} \tag{2.42}$$

The anomalous dimensions of $B_i^{(\mathrm{cut})}$ and $\mathcal{S}_i^{(\mathrm{cut})}$ have the general structure

$$\begin{aligned}
\gamma^i_{\mathcal{S}^{\mathrm{cut}}}(\eta_{\mathrm{cut}}, \mu, \nu) &= 2\Gamma^i_{\mathrm{cusp}}[\alpha_s(\mu)]\,\ln\frac{\nu e^{-\eta_{\mathrm{cut}}}}{\mu} + \gamma^i_{\mathcal{S}^{\mathrm{cut}}}[\alpha_s(\mu)]\,, \\
\gamma^i_{\nu,\mathcal{S}^{\mathrm{cut}}}(p_T^{\mathrm{cut}}, R, \mu) &= 2\eta^i_\Gamma(p_T^{\mathrm{cut}}, \mu) + \gamma^i_{\nu,\mathcal{S}^{\mathrm{cut}}}[\alpha_s(p_T^{\mathrm{cut}}), R]\,, \\
\gamma^i_{B^{\mathrm{cut}}}(\omega e^{-\eta_{\mathrm{cut}}}, \mu) &= 2\Gamma^i_{\mathrm{cusp}}[\alpha_s(\mu)]\,\ln\frac{\mu}{\omega e^{-\eta_{\mathrm{cut}}}} + \gamma^i_{B^{\mathrm{cut}}}[\alpha_s(\mu)]\,,
\end{aligned} \tag{2.43}$$

where the coefficients of the cusp anomalous dimension follow from our explicit one-loop calculation. Consistency with eq. (2.14) implies

$$\begin{aligned}
\gamma^i_{\mathcal{S}^{\mathrm{cut}}}(\alpha_s) + \gamma^i_{B^{\mathrm{cut}}}(\alpha_s) &= \gamma^i_B(\alpha_s)\,, \\
\gamma^i_{\nu,\mathcal{S}^{\mathrm{cut}}}(\alpha_s, R) &= \gamma^i_{\nu,B}(\alpha_s, R) = -\frac{1}{2}\gamma^i_\nu(\alpha_s, R)\,.
\end{aligned} \tag{2.44}$$

JHEP04(2019)142

All of the above noncusp anomalous dimensions vanish at one loop. The canonical scales for $B_i^{(\mathrm{cut})}$ and $\mathcal{S}_i^{(\mathrm{cut})}$ are

$$\mu_B^{(\mathrm{cut})} \sim Q e^{-\eta_{\mathrm{cut}}}\,, \quad \mu_{\mathcal{S}}^{(\mathrm{cut})} \sim p_T^{\mathrm{cut}}\,, \quad \nu_{\mathcal{S}}^{(\mathrm{cut})} \sim p_T^{\mathrm{cut}} e^{\eta_{\mathrm{cut}}}\,. \tag{2.45}$$

With these choices and the anomalous dimensions in eq. (2.43) one may resum logarithms of $e^{\eta_{\mathrm{cut}}}$, p_T^{cut}/Q to any logarithmic order, and at LL also logarithms of $p_T^{\mathrm{cut}}/Qe^{-\eta_{\mathrm{cut}}}$.

Starting at $\mathcal{O}(\alpha_s^2)$, the $\mathcal{B}_i^{(\mathrm{NG})}$ term in eq. (2.37) contains nonglobal logarithms of the form $\alpha_s^n \ln^n(p_T^{\mathrm{cut}}/Qe^{-\eta_{\mathrm{cut}}})$. A boost by η_{cut} translates the measurement into two hemispheres with one loose ($\eta > \eta_{\mathrm{cut}}$) and one tight constraint ($\eta < \eta_{\mathrm{cut}}$) on emissions. The nonglobal structure in such a scenario is well understood [60]. Depending on the desired accuracy, the NGLs may be included at fixed order via $\mathcal{B}_i^{(\mathrm{NG})}$ as indicated in eq. (2.37), or (partially) summed using more steps in a dressed parton expansion [53].

Note that beyond one loop there is some freedom in the choice of measurement that defines the $B_i^{(\mathrm{cut})}$ and $\mathcal{S}_i^{(\mathrm{cut})}$. In particular, different measurements that reduce to eqs. (2.38) and (2.40) for a single emission could give rise to different results for the two-loop noncusp anomalous dimensions and finite terms because the difference can be absorbed into $\mathcal{B}_i^{(\mathrm{NG})}$. We stress that the result eq. (2.42) for the $\ln R$ coefficient in the two-loop soft-collinear function is, however, still unique. This is because a $\ln R$ contribution to $\mathcal{B}^{(\mathrm{NG})}$ requires a collinear parton in the unconstrained region to emit a soft-collinear gluon into the constrained region, which then undergoes a further collinear splitting. This is only possible starting at $\mathcal{O}(\alpha_s^3)$.

Numerical validation. To illustrate the numerical relevance of regime 3, we again consider the fixed $\mathcal{O}(\alpha_s)$ p_T^{jet} spectrum. In regime 2, it is given to leading power in p_T^{jet}/Q by the derivative of eq. (2.12), while in regime 3, it is given to leading power in $p_T^{\mathrm{jet}}/(Qe^{-\eta_{\mathrm{cut}}})$ by the derivative of eq. (2.35).

In figure 6 we compare the two results for $\eta_{\mathrm{cut}} = 2.5$. In regime 3, the 0-jet cross section at $\mathcal{O}(\alpha_s)$ contains only single logarithms of p_T^{cut}, because the double logarithms cancel between the soft and soft-collinear functions. For this reason, the dashed-blue regime 3 spectrum with respect to $\ln p_T^{\mathrm{jet}}$ is just a constant. The exact regime 2 result (solid orange) becomes well approximated by the further factorized regime 3 expression for $p_T^{\mathrm{jet}} \to 0$, with their difference (dotted green) behaving like a power in p_T^{jet}. This provides a strong check of the regime 3 ingredients, more precisely, of the p_T^{cut} dependence encoded in the soft-collinear function. (Since the beam function in regime 3 is independent of p_T^{cut}, it drops out when computing the fixed-order spectrum.)

We also observe that for $gg \to H$ and Drell-Yan at $Q = m_Z$, the regime 3 limit is applicable only at very small $p_T^{\mathrm{jet}} \lesssim 1\,\mathrm{GeV}$ and already at $p_T^{\mathrm{jet}} \sim 10$–$20\,\mathrm{GeV}$ the power corrections with respect to regime 2 are of the same size as the full regime 2 result. This means that one would have to turn off the additional regime 3 resummation above this region. For $gg \to X$ with $m_X = 1\,\mathrm{TeV}$ and Drell-Yan at $Q = 1\,\mathrm{TeV}$, the canonical regime 3 resummation region, i.e., the region where the regime 3 singular corrections clearly dominate, extends up to $p_T^{\mathrm{jet}} \lesssim 10\,\mathrm{GeV}$, while regime 2 power corrections become $\mathcal{O}(1)$ around $p_T^{\mathrm{jet}} \sim 60\,\mathrm{GeV}$.

JHEP04(2019)142

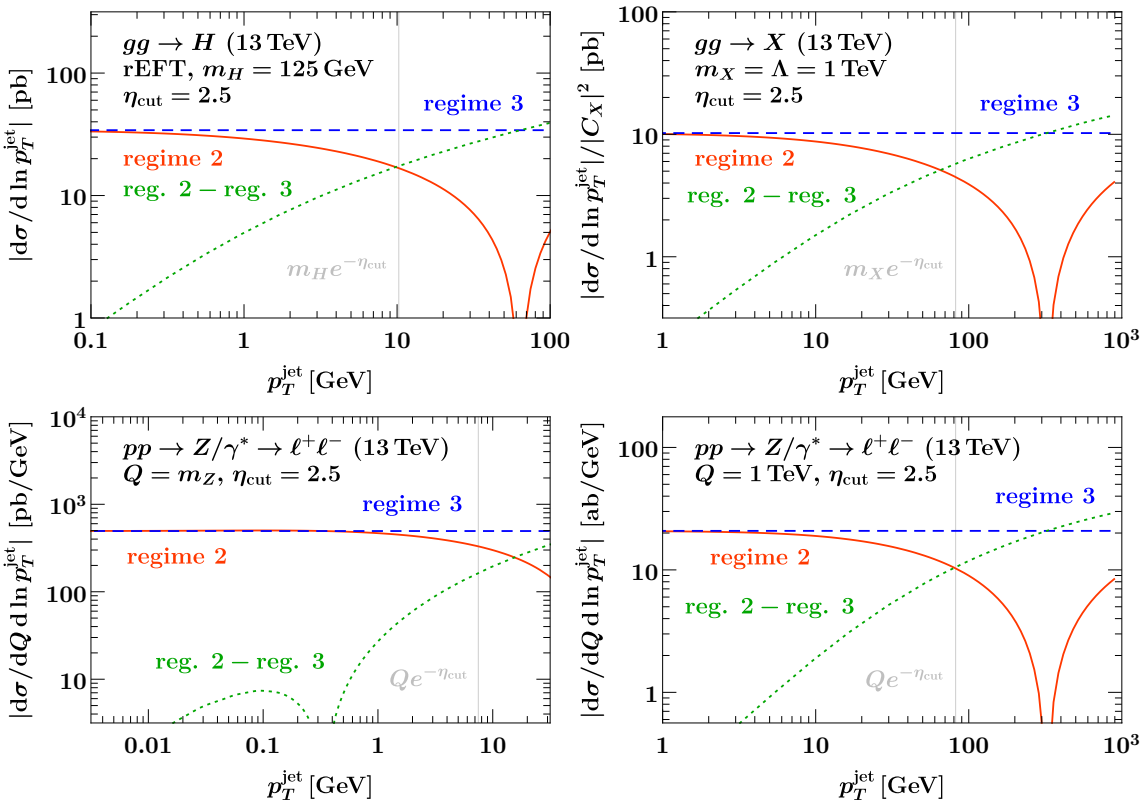

Figure 6. Comparison of the singular contributions to the fixed $\mathcal{O}(\alpha_s)$ $p_T^{\rm jet}$ spectrum for $gg \to H$ (top left), $gg \to X$ (top right), and Drell-Yan at $Q = m_Z$ (bottom left) and $Q = 1\,\text{TeV}$ (bottom right). The solid orange lines show the full regime 2 singular spectrum, the blue dashed lines the further factorized regime 3 result. Their difference shown by the dotted green lines vanishes as a power in $p_T^{\rm jet}/Qe^{-\eta_{\rm cut}}$ for small $p_T^{\rm jet}$. The vertical lines indicate where the relation $p_T^{\rm jet} = Qe^{-\eta_{\rm cut}}$ is satisfied.

Hence, we find that the additional resummation of logarithms of $p_T^{\rm jet}/(Qe^{-\eta_{\rm cut}})$ in regime 3 is not relevant for jet veto analyses at the LHC, where the lowest jet cuts are $p_T^{\rm cut} \sim 25\,\text{GeV}$, for $\eta_{\rm cut} = 2.5$ and final states in the $Q \sim 100\,\text{GeV}$ range. This also holds for final states at very high invariant mass, e.g. in new physics searches, since in this case one would typically also apply higher jet thresholds to retain enough signal in the 0-jet bin. Realistically, one would not go below $p_T^{\rm cut} \sim 0.1Q$, which means one never enters the limit where the regime 3 resummation is necessary. This of course does not exclude the possibility that measurements designed to probe simultaneously very high Q and very low $p_T^{\rm jet}$ could benefit from the regime 3 resummation. To explicitly explore this regime experimentally, the best option is to restrict the jet veto to the very central region with $\eta_{\rm cut} \sim 1$–1.5.

2.5 Comparison to the literature

Jet vetoes in a restricted rapidity range were already encountered in ref. [33] for the case of dijet production. Without spelling it out explicitly, ref. [33] used a factorization for

JHEP04(2019)142

the regime 3 hierarchy $p_T^{\text{cut}} \ll Qe^{-\eta_{\text{cut}}} \ll Q$, but did not distinguish between the soft and soft-collinear modes necessary in this regime. As a result, parametrically large rapidity logarithms $\ln e^{\eta_{\text{cut}}}$ were not captured, which are relevant starting at NLL. The numerical results in ref. [33] were obtained for $Q \sim 1\,\text{TeV}$, $\eta_{\text{cut}} = 5$, and $p_T^{\text{cut}} = 20\,\text{GeV}$, which rather corresponds to the opposite regime 1, $p_T^{\text{cut}} \gg Qe^{-\eta_{\text{cut}}}$. The difference between regimes 1 and 3 already matters at LL.

In ref. [34], the soft and soft-collinear modes in regime 3 are distinguished and the presence of nonglobal logarithms in this regime is recognized. Their factorization for dijet production is carried out at a level analogous to ours in the previous subsection. That is, at NLL and beyond it only captures logarithms of "global" origin, but does not capture nonglobal logarithms that are parametrically of the same size. Our results for the one-loop quark matching coefficients in eq. (2.38) and the one-loop soft-collinear function in eq. (2.40) agree with ref. [34] [see their eqs. (3.27), (B.3), and (B.5)]. Our results for the gluon channels and the two-loop clustering corrections are new.

Ref. [34] does not consider regime 2 as a separate parametric regime. Instead, it attempts to extend the validity of the regime 3 factorization into regime 2. This is done by effectively adding the regime 2 nonsingular corrections appearing in eq. (2.36) to the unmeasured beam functions. Since some of the regime 3 modes become redundant in regime 2, this also requires them to account for a nontrivial soft-collinear zero bin. At fixed order, the sum of all their contributions must reproduce our result for the regime 2 beam function; in appendix A.5 we check that this is indeed the case for the quark matrix elements given in ref. [34]. As we have seen in figure 6, outside the canonical regime 3, there are large cancellations between the terms that are singular in the regime 3 limit and the remaining regime 2 nonsingular contributions. This means that the distinction between these contributions becomes arbitrary in regime 2 and that they must not be treated differently, as otherwise one risks inducing large miscancellations. (This is completely analogous to the situation when matching to full QCD, in which case the p_T^{cut} resummation must be turned off when entering the fixed-order region at large p_T^{cut} to properly recover the full-QCD result.) In particular, in regime 2 all contributions that belong to the full η_{cut}-dependent regime 2 beam function must be evaluated at a common scale $\mu \simeq p_T^{\text{cut}}$ and evolved together according to eq. (2.13). This is not the case in ref. [34], where individual contributions to the regime 2 beam function are evaluated at different scales throughout (μ_B^{cut} and μ_S^{cut} in our notation).

Recently, the setup of ref. [34] was applied in ref. [35] to the case of transverse energy E_T in a restricted rapidity range in Drell-Yan. In ref. [35], profile scales are used to combine regimes 3 and 1, requiring that asymptotically $\mu_B^{(\text{cut})} = \mu_S^{(\text{cut})}$ in the regime 1 limit $E_T \gg Qe^{-\eta_{\text{cut}}}$. While this can alleviate the issue raised above, formally this relation must be satisfied already in regime 2 for $E_T \sim Qe^{-\eta_{\text{cut}}}$.

As we have seen in section 2.3, there is no need to distinguish collinear and soft-collinear modes in regime 2. Since for jet-veto analyses regimes 1 and 2 are the phenomenologically relevant ones, doing so unnecessarily complicates the description. Recovering the NNLL′ structure in regime 2 [see eq. (2.24)] based on regime 3 would be quite challenging due to the intricate nonglobal structure in regime 3. Our dedicated treatment of regime 2 makes

JHEP04(2019)142

the absence of nonglobal logarithms manifest, avoiding the associated complications, and automatically ensures the correct treatment of the regime 2 nonsingular terms. Furthermore, it shows how regime 2 generalizes the well-understood regime 1, and as we will see in the next section allows for the generalization to a step in the jet veto.

Concerning regime 1, ref. [35] also gave an argument that regime 1 holds up to power corrections in $Qe^{-\eta_{\rm cut}}/E_T$, which was more intricate due to immediately comparing regime 1 to regime 3. The power suppression of $\eta_{\rm cut}$ effects at sufficiently large $\eta_{\rm cut}$ was also pointed out briefly in a somewhat different context in ref. [61].

3 Generalization to a step in the jet veto at $\eta_{\rm cut}$

3.1 Overview of parametric regimes

We now generalize our results to the experimentally relevant scenario of the step-like jet veto illustrated in the right panel of figure 1. Here, jets with $p_T^{\rm jet} > p_T^{\rm cut}$ are vetoed if $|\eta_{\rm jet}| < \eta_{\rm cut}$, while for $|\eta_{\rm jet}| > \eta_{\rm cut}$ the veto is loosened to $p_T^{\rm jet} > \tilde{p}_T^{\rm cut} > p_T^{\rm cut}$. The 0-jet cross section is thus defined by the following measurement:

$$\max_{k\in\text{jets: }|\eta_k|<\eta_{\rm cut}} |\vec{p}_{T,k}| < p_T^{\rm cut} \qquad \text{and} \qquad \max_{k\in\text{jets: }|\eta_k|>\eta_{\rm cut}} |\vec{p}_{T,k}| < \tilde{p}_T^{\rm cut}\,. \tag{3.1}$$

There are now three relevant power-counting parameters $p_T^{\rm cut}/Q$, $\tilde{p}_T^{\rm cut}/Q$, and $e^{-\eta_{\rm cut}}$ with four distinct parametric regimes (assuming $p_T^{\rm cut} \le \tilde{p}_T^{\rm cut}$), illustrated in figure 7:

- $p_T^{\rm cut}/Q \sim \tilde{p}_T^{\rm cut}/Q \sim e^{-\eta_{\rm cut}}$ (collinear step, top left),
- $p_T^{\rm cut}/Q \ll \tilde{p}_T^{\rm cut}/Q \sim e^{-\eta_{\rm cut}}$ (collinear NGLs, top right),
- $p_T^{\rm cut}/Q \sim \tilde{p}_T^{\rm cut}/Q \ll e^{-\eta_{\rm cut}}$ (soft-collinear step, bottom left),
- $p_T^{\rm cut}/Q \ll \tilde{p}_T^{\rm cut}/Q \ll e^{-\eta_{\rm cut}}$ (soft-collinear NGLs, bottom right).

We discuss each of them in turn in the following subsections. For $p_T^{\rm cut}/Q \sim e^{-\eta_{\rm cut}}$ (top left) the only relevant case is $\tilde{p}_T^{\rm cut} \sim p_T^{\rm cut}$, leading to a modified measurement on the collinear modes, a collinear step, compared to the case without a step ($\tilde{p}_T^{\rm cut} = p_T^{\rm cut}$).

For $p_T^{\rm cut}/Q \ll e^{-\eta_{\rm cut}}$, we have to distinguish three cases depending on $\tilde{p}_T^{\rm cut}$. Keeping $\tilde{p}_T^{\rm cut} \sim e^{-\eta_{\rm cut}}$ implies the hierarchy $p_T^{\rm cut}/Q \ll \tilde{p}_T^{\rm cut}/Q \sim e^{-\eta_{\rm cut}}$ (top right). Here, the mode setup is the same as for regime 3 without step (corresponding to $\tilde{p}_T^{\rm cut} = \infty$). As in that case, the large difference in the constraints on collinear radiation above and below $\eta_{\rm cut}$ gives rise to collinear NGLs.

For $\tilde{p}_T^{\rm cut}/Q \ll e^{-\eta_{\rm cut}}$, we can then have either $p_T^{\rm cut}/Q \sim \tilde{p}_T^{\rm cut}/Q \ll e^{-\eta_{\rm cut}}$ (bottom left) or $p_T^{\rm cut}/Q \ll \tilde{p}_T^{\rm cut}/Q \ll e^{-\eta_{\rm cut}}$ (bottom right). For the former, the standard jet veto factorization is recovered except that there are additional soft-collinear modes that resolve the shallow step at $\eta_{\rm cut}$. For the latter, the steep step $p_T^{\rm cut} \ll \tilde{p}_T^{\rm cut}$ at $\eta_{\rm cut}$ gives rise to two distinct sets of soft-collinear modes with parametrically large soft-collinear NGLs between them.

JHEP04(2019)142

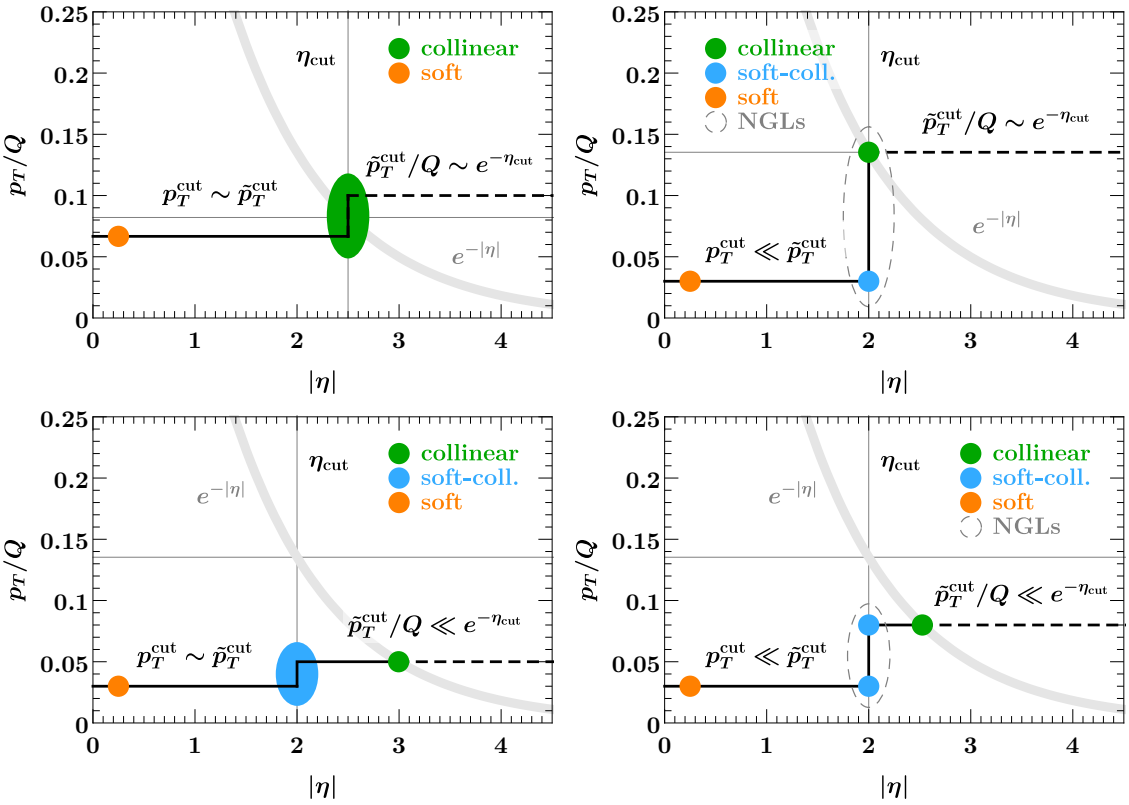

Figure 7. Illustration of the parametric regimes for a jet veto with a step. Emissions above the black lines are vetoed, and the thick gray line corresponds to $p_T/Q = e^{-|\eta|}$. The colored circles indicate the relevant modes in the effective theory. The regimes in the top row are characterized by $\tilde{p}_T^{\rm cut} \sim e^{-\eta_{\rm cut}}$, while those in the bottom row have $\tilde{p}_T^{\rm cut} \ll e^{-\eta_{\rm cut}}$. The regimes on the left have $p_T^{\rm cut} \sim \tilde{p}_T^{\rm cut}$, while those on the right have $p_T^{\rm cut} \ll \tilde{p}_T^{\rm cut}$ and involve parametrically large non-global logarithms.

3.2 $p_T^{\rm cut}/Q \sim \tilde{p}_T^{\rm cut}/Q \sim e^{-\eta_{\rm cut}}$ (collinear step)

We first note that the hierarchy $p_T^{\rm cut}/Q \sim e^{-\eta_{\rm cut}} \ll \tilde{p}_T^{\rm cut}/Q$ is effectively equivalent to the case without any jet veto beyond $\eta_{\rm cut}$ (regime 2 in section 2.3). Since collinear emissions with $|\eta| > \eta_{\rm cut}$ cannot resolve the loose veto at $\tilde{p}_T^{\rm cut}$, its effect is suppressed by $1/\tilde{p}_T^{\rm cut}$ and vanishes for $\tilde{p}_T^{\rm cut} \to \infty$.

The first nontrivial hierarchy is $p_T^{\rm cut}/Q \sim \tilde{p}_T^{\rm cut}/Q \sim e^{-\eta_{\rm cut}}$, illustrated in the top left panel of figure 7. In this regime, the required modes are the same as in regime 2 in section 2.3. The collinear radiation resolves the step at $\eta_{\rm cut}$ while soft emissions are insensitive to it, leading to a generalization of eq. (2.12),

$$\begin{aligned}\sigma_0(p_T^{\rm cut}, \tilde{p}_T^{\rm cut}, \eta_{\rm cut}, R, \Phi) = {}& H_\kappa(\Phi, \mu) \\ & \times B_a(p_T^{\rm cut}, \tilde{p}_T^{\rm cut}, \eta_{\rm cut}, R, \omega_a, \mu, \nu)\, B_b(p_T^{\rm cut}, \tilde{p}_T^{\rm cut}, \eta_{\rm cut}, R, \omega_b, \mu, \nu) \\ & \times S_\kappa(p_T^{\rm cut}, R, \mu, \nu) \left[1 + \mathcal{O}\left(\frac{p_T^{\rm cut}}{Q}, \frac{\tilde{p}_T^{\rm cut}}{Q}, e^{-\eta_{\rm cut}}, R^2\right)\right], \end{aligned} \tag{3.2}$$

JHEP04(2019)142

with the beam functions now additionally depending on $\tilde{p}_T^{\text{cut}}$. In analogy to eq. (2.16) we write the modified beam function matching coefficients as

$$\mathcal{I}_{ij}(p_T^{\text{cut}}, \tilde{p}_T^{\text{cut}}, \eta_{\text{cut}}, R, \omega, z, \mu, \nu) = \mathcal{I}_{ij}(p_T^{\text{cut}}, R, \omega, z, \mu, \nu) + \Delta\mathcal{I}_{ij}(p_T^{\text{cut}}, \tilde{p}_T^{\text{cut}}, \eta_{\text{cut}}, R, \omega, z, \mu, \nu)\,. \tag{3.3}$$

The first term on the right-hand side is again the matching coefficient for a single veto at p_T^{cut} without any rapidity dependence. The second term is the correction due to the step in the jet veto at $|\eta| = \eta_{\text{cut}}$, which vanishes for $p_T^{\text{cut}} = \tilde{p}_T^{\text{cut}}$. The correction is again renormalized according to eq. (2.21), which as before follows from RG consistency. In particular, its two-loop structure predicted by the RGE is the same as in eq. (2.24), where the finite terms now depend on two dimensionless ratios,

$$\zeta_{\text{cut}} = \frac{\omega e^{-\eta_{\text{cut}}}}{p_T^{\text{cut}}}\,, \qquad \tilde{\zeta}_{\text{cut}} = \frac{\omega e^{-\eta_{\text{cut}}}}{\tilde{p}_T^{\text{cut}}}\,. \tag{3.4}$$

The one-loop and $\ln R$ enhanced two-loop finite terms in $\Delta\mathcal{I}_{ij}$ can be written in terms of the results in eqs. (2.25) and (2.27) as

$$\begin{aligned}
\Delta I_{ij}^{(1)}(\zeta_{\text{cut}}, \tilde{\zeta}_{\text{cut}}, z) &= \Delta I_{ij}^{(1)}(\zeta_{\text{cut}}, z) - \Delta I_{ij}^{(1)}(\tilde{\zeta}_{\text{cut}}, z)\,, \\
\Delta I_{ij}^{(2)}(\zeta_{\text{cut}}, \tilde{\zeta}_{\text{cut}}, R, z) &= \ln R \left[\Delta I_{ij}^{(2,\ln R)}(\zeta_{\text{cut}}, z) - \Delta I_{ij}^{(2,\ln R)}(\tilde{\zeta}_{\text{cut}}, z)\right], \\
&\quad + \Delta I_{ij}^{(2,c)}(\zeta_{\text{cut}}, \tilde{\zeta}_{\text{cut}}, z) + \mathcal{O}(R^2)\,,
\end{aligned} \tag{3.5}$$

since for a single (primary) n_a-collinear emission at (η, p_T) the measurement function for the step correction can be rewritten as

$$\begin{aligned}
&\theta(\eta - \eta_{\text{cut}})\big[\theta(\tilde{p}_T^{\text{cut}} - p_T) - \theta(p_T^{\text{cut}} - p_T)\big] \\
&\quad = \theta(\eta - \eta_{\text{cut}})\,\theta(p_T - p_T^{\text{cut}}) - \theta(\eta - \eta_{\text{cut}})\,\theta(p_T - \tilde{p}_T^{\text{cut}})\,.
\end{aligned} \tag{3.6}$$

Due to the presence of correlated emissions with rapidities smaller and larger than η_{cut} at two loops, this decomposition no longer applies for the full two-loop finite term $\Delta I_{ij}^{(2,c)}$, which therefore needs to be determined separately.

This regime is free of large nonglobal logarithms and is of direct phenomenological interest. The parametric assumptions are satisfied e.g. for high-mass searches, $Q \gtrsim 300\,\text{GeV}$, a realistic rapidity cut $\eta_{\text{cut}} = 2.5$, and veto parameters $p_T^{\text{cut}} = 25\,\text{GeV}$, $\tilde{p}_T^{\text{cut}} = 50\,\text{GeV}$, which clearly warrant resummation of logarithms of $p_T^{\text{cut}}/Q \sim \tilde{p}_T^{\text{cut}}/Q \sim e^{-\eta_{\text{cut}}}$. Evolving the beam function from $\mu_B \sim p_T^{\text{cut}} \sim \tilde{p}_T^{\text{cut}} \sim Qe^{-\eta_{\text{cut}}}$ to $\mu_H \sim Q$ achieves this resummation for all of the above large ratios in the cross section, while the full (logarithmic and nonlogarithmic) dependence on all of the $\mathcal{O}(1)$ ratios $p_T^{\text{cut}}/\tilde{p}_T^{\text{cut}}$, $Qe^{-\eta_{\text{cut}}}/p_T^{\text{cut}}$, and $Qe^{-\eta_{\text{cut}}}/\tilde{p}_T^{\text{cut}}$ is included at fixed order via the beam function boundary condition.

Numerical validation. We now check that the factorized 0-jet cross section in eq. (3.2) reproduces the singular limit of full QCD. For this purpose, we construct an observable that simultaneously forces $p_T^{\text{cut}} \to 0$ and $\tilde{p}_T^{\text{cut}} \to 0$ as it approaches its singular limit. Following the rapidity-dependent jet vetoes in ref. [16], we define

$$\mathcal{T}_{\text{step}} = \max_{k \in \text{jets}} |\vec{p}_{T,k}| f_{\text{step}}(\eta_k)\,, \qquad f_{\text{step}}(\eta) = \begin{cases} \frac{1}{\rho}, & |\eta| > \eta_{\text{cut}}\,, \\ 1, & |\eta| < \eta_{\text{cut}}\,, \end{cases} \tag{3.7}$$

JHEP04(2019)142

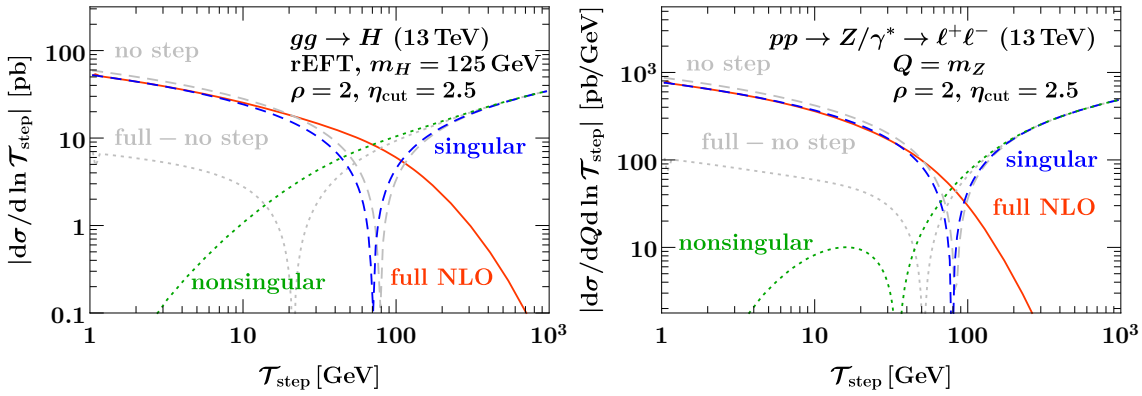

Figure 8. Comparison of singular and nonsingular contributions to the fixed $\mathcal{O}(\alpha_s)$ (LO_1) $\mathcal{T}_{\rm step}$ spectrum with a step at $\eta_{\rm cut} = 2.5$ and $\rho = \tilde{p}_T^{\rm cut}/p_T^{\rm cut} = 2$ for $gg \to H$ (left) and Drell-Yan at $Q = m_Z$ (right). The orange solid lines show the full results, the dashed blue lines the singular result that accounts for the jet veto step at $\eta_{\rm cut}$ in the beam function, and the dotted green lines their difference. The dashed and dotted gray lines show the corresponding results without taking into account the step in the jet veto, which do not describe the singular behavior of the full cross section.

i.e., we can express the step veto by ordering the jets with respect to their weighted transverse momenta, where for $|\eta| > \eta_{\rm cut}$ the corresponding step weight function $f_{\rm step}(\eta)$ is given by the ratio of veto parameters,

$$\rho \equiv \frac{\tilde{p}_T^{\rm cut}}{p_T^{\rm cut}} > 1\,. \tag{3.8}$$

The differential spectrum in $\mathcal{T}_{\rm step}$ is then related to the jet-vetoed cross section with a step by the relation

$$\sigma_0(p_T^{\rm cut},\, \rho\, p_T^{\rm cut},\, \eta_{\rm cut}, R) = \int_0^{p_T^{\rm cut}} \mathrm{d}\mathcal{T}_{\rm step}\, \frac{\mathrm{d}\sigma(\rho, \eta_{\rm cut}, R)}{\mathrm{d}\mathcal{T}_{\rm step}}\,. \tag{3.9}$$

In figure 8 we compare $\mathrm{d}\sigma(\rho, \eta_{\rm cut})/\mathrm{d}\mathcal{T}_{\rm step}$ at fixed $\mathcal{O}(\alpha_s)$ in full QCD to the singular spectrum predicted by eq. (3.2) as well as the standard factorization eq. (2.8) without a step for $gg \to H$ (left panel) and Drell-Yan at the Z pole (right panel). The singular result using the full $\tilde{p}_T^{\rm cut}$ and $\eta_{\rm cut}$ dependent beam functions (dashed blue) correctly reproduces the singular behavior of full QCD (solid orange) in the limit $\mathcal{T}_{\rm step} \to 0$, with the difference to the full QCD spectrum (dotted green) vanishing like a power in $\mathcal{T}_{\rm step}$ as it should. On the other hand, the standard factorization without step (dashed gray) does not reproduce the correct singular behavior of full QCD, with the difference (dotted gray) diverging for $\mathcal{T}_{\rm step} \to 0$. Note that the mismatch here is reduced compared to the $\tilde{p}_T^{\rm cut} = \infty$ case shown in figures 4 and 5, owing to the larger phase space available to unconstrained radiation at $|\eta| > \eta_{\rm cut}$ for $\tilde{p}_T^{\rm cut} = \infty$.

3.3 $p_T^{\rm cut}/Q \ll \tilde{p}_T^{\rm cut}/Q \sim e^{-\eta_{\rm cut}}$ (collinear NGLs)

This regime is a direct extension of regime 3 without a step in section 2.4. For $e^{-\eta_{\rm cut}} \ll \tilde{p}_T^{\rm cut}/Q$, the effect of $\tilde{p}_T^{\rm cut}$ is again suppressed by $1/\tilde{p}_T^{\rm cut}$ and vanishes for $\tilde{p}_T^{\rm cut} \to \infty$, yielding

JHEP04(2019)142

the same result as in section 2.4. The nontrivial new hierarchy is $p_T^{\rm cut}/Q \ll \tilde{p}_T^{\rm cut}/Q \sim e^{-\eta_{\rm cut}}$, shown in the top right panel of figure 7. In this regime, the mode setup is as in section 2.4. However, the collinear modes are now additionally constrained for $|\eta| > \eta_{\rm cut}$ by the jet veto at $\tilde{p}_T^{\rm cut}$, making them sensitive to both $\tilde{p}_T^{\rm cut}$ and the kinematic scale $Qe^{-\eta_{\rm cut}}$. This leads to a modification of the overall initial-state collinear functions in eqs. (2.35) and (2.36) by

$$\begin{aligned}\mathcal{B}_i(p_T^{\rm cut}, \tilde{p}_T^{\rm cut}, \eta_{\rm cut}, R, \omega, \mu, \nu) &= B_i^{(\rm cut)}(\tilde{p}_T^{\rm cut}, \eta_{\rm cut}, R, \omega, \mu)\, \mathcal{S}_i^{(\rm cut)}(p_T^{\rm cut}, \eta_{\rm cut}, R, \mu, \nu) \\ &\quad \times \left[1 + \mathcal{B}_i^{(\rm NG)}\left(\frac{p_T^{\rm cut}}{\omega e^{-\eta_{\rm cut}}}, \frac{p_T^{\rm cut}}{\tilde{p}_T^{\rm cut}}, \omega, R\right)\right]. \end{aligned} \tag{3.10}$$

Here $\mathcal{S}_i^{(\rm cut)}$ is the same soft-collinear function as in eq. (2.37). By RG consistency the functions $B_i^{(\rm cut)}$ have the same renormalization as those in eq. (2.37), i.e., the additional dependence on $\tilde{p}_T^{\rm cut}$ does not change their renormalization. The associated matching coefficients at one loop are given by subtracting the correction term $\Delta I_{ij}^{(1)}$ in eq. (2.25), which accounts for an n-collinear emission with $\eta > \eta_{\rm cut}$ and $p_T > \tilde{p}_T^{\rm cut}$, from the coefficient $\mathcal{I}_{ij}^{(\rm cut)}$ in eq. (2.38), which accounts for an n-collinear emission with $\eta > \eta_{\rm cut}$ without constraints from a jet veto, such that

$$\mathcal{I}_{ij}^{(\rm cut)}(\tilde{p}_T^{\rm cut}, \eta_{\rm cut}, R, \omega, z, \mu) = \mathcal{I}_{ij}^{(\rm cut)}(\eta_{\rm cut}, \omega, z, \mu) - \frac{\alpha_s(\mu)}{4\pi} \Delta I_{ij}^{(1)}\left(\frac{\omega e^{-\eta_{\rm cut}}}{\tilde{p}_T^{\rm cut}}, z, R\right) + \mathcal{O}(\alpha_s^2)\,. \tag{3.11}$$

The $\mathcal{B}_i^{(\rm NG)}$ term in eq. (3.10) contains nonglobal logarithms of $p_T^{\rm cut}/\tilde{p}_T^{\rm cut} \sim p_T^{\rm cut}/Qe^{-\eta_{\rm cut}}$.

3.4 $p_T^{\rm cut}/Q \sim \tilde{p}_T^{\rm cut}/Q \ll e^{-\eta_{\rm cut}}$ (soft-collinear step)

In this regime (bottom left panel of figure 7), the mode setup in section 2.2 is extended by soft-collinear modes that resolve the step in the jet veto at $\eta_{\rm cut}$,

$$\begin{aligned} &n_a\text{-soft-collinear:} \quad p^\mu \sim p_T^{\rm cut}(e^{-\eta_{\rm cut}}, e^{\eta_{\rm cut}}, 1) \sim \tilde{p}_T^{\rm cut}(e^{-\eta_{\rm cut}}, e^{\eta_{\rm cut}}, 1)\,, \\ &n_b\text{-soft-collinear:} \quad p^\mu \sim p_T^{\rm cut}(e^{\eta_{\rm cut}}, e^{-\eta_{\rm cut}}, 1) \sim \tilde{p}_T^{\rm cut}(e^{\eta_{\rm cut}}, e^{-\eta_{\rm cut}}, 1)\,. \end{aligned} \tag{3.12}$$

At the same time, the collinear modes only see the jet veto at $\tilde{p}_T^{\rm cut}$, while the soft modes only see the veto at $p_T^{\rm cut}$. This yields the factorized cross section

$$\begin{aligned}\sigma_0(p_T^{\rm cut}, \tilde{p}_T^{\rm cut}, \eta_{\rm cut}, R, \Phi) &= H_\kappa(\Phi, \mu)\, B_a(\tilde{p}_T^{\rm cut}, R, \omega, \mu, \nu)\, B_b(\tilde{p}_T^{\rm cut}, R, \omega, \mu, \nu)\, S_\kappa(p_T^{\rm cut}, \mu, \nu) \\ &\quad \times \mathcal{S}_a(p_T^{\rm cut}, \tilde{p}_T^{\rm cut}, \eta_{\rm cut}, R, \mu, \nu)\, \mathcal{S}_b(p_T^{\rm cut}, \tilde{p}_T^{\rm cut}, \eta_{\rm cut}, R, \mu, \nu) \\ &\quad \times \left[1 + \mathcal{O}\left(\frac{p_T^{\rm cut}}{Q}, \frac{\tilde{p}_T^{\rm cut}}{Q}, \frac{p_T^{\rm cut}}{Qe^{-\eta_{\rm cut}}}, \frac{\tilde{p}_T^{\rm cut}}{Qe^{-\eta_{\rm cut}}}, R^2\right)\right]. \end{aligned} \tag{3.13}$$

The soft-collinear function $\mathcal{S}_i$ encodes the actual step at $\eta_{\rm cut}$ and is defined by the measurement eq. (3.1). For $\tilde{p}_T^{\rm cut} = p_T^{\rm cut}$ there is no step in the jet veto and $\mathcal{S}_i$ has to vanish. The RG consistency of the cross section implies that its μ anomalous dimension vanishes in general, while its resummed ν anomalous dimension is given by

$$\gamma_{\nu,\mathcal{S}}^i(p_T^{\rm cut}, \tilde{p}_T^{\rm cut}, R) = 2\eta_\Gamma^i(p_T^{\rm cut}, \tilde{p}_T^{\rm cut}) + \frac{1}{2}\Big\{\gamma_\nu^i[\alpha_s(\tilde{p}_T^{\rm cut}), R] - \gamma_\nu^i[\alpha_s(p_T^{\rm cut}), R]\Big\}\,. \tag{3.14}$$

JHEP04(2019)142

It does not depend on μ at all, as required by exact path independence in the (μ,ν) plane. Note that the beam functions in eq. (3.13) depend on $\tilde{p}_T^{\text{cut}}$ (rather than p_T^{cut}) because collinear radiation is too forward to be constrained by the tighter central veto. This is reflected in the somewhat curious rapidity anomalous dimension of $\mathcal{S}_i$ in eq. (3.14), which accounts for the mismatch between the logarithms of p_T^{cut} and $\tilde{p}_T^{\text{cut}}$ generated by the soft and beam rapidity evolution, respectively.

Solving eq. (3.14) order by order in α_s we find the following very simple structure of the soft-collinear function through two loops:

$$\begin{aligned}\mathcal{S}_i(p_T^{\text{cut}},\tilde{p}_T^{\text{cut}},\eta_{\text{cut}},R,\mu,\nu) = 1 &+ \frac{\alpha_s(\mu)}{4\pi}\Big[2\Gamma_0^i \ln\rho\, L_{\mathcal{S}}^{\nu} + \mathcal{S}_{i,1}(\rho)\Big] \\ &+ \frac{\alpha_s^2(\mu)}{(4\pi)^2}\Big\{2(\Gamma_0^i)^2\ln^2\rho\,(L_{\mathcal{S}}^{\nu})^2 + 2\ln\rho\, L_{\mathcal{S}}^{\nu}\big[2L_{\mathcal{S}}^{\mu}\beta_0\Gamma_0^i + \Gamma_0^i\,\mathcal{S}_{i,1}(\rho) + \Gamma_1^i\big] \\ &\qquad + 2\beta_0 L_{\mathcal{S}}^{\mu}\,\mathcal{S}_{i,1}(\rho) + \mathcal{S}_{i,2}(\rho,R)\Big\} + \mathcal{O}(\alpha_s^3)\,,\end{aligned} \tag{3.15}$$

where

$$\rho \equiv \frac{\tilde{p}_T^{\text{cut}}}{p_T^{\text{cut}}}\,, \qquad L_{\mathcal{S}}^{\nu} \equiv \ln\frac{\nu}{\sqrt{p_T^{\text{cut}}\tilde{p}_T^{\text{cut}}}\,e^{\eta_{\text{cut}}}}\,, \qquad L_{\mathcal{S}}^{\mu} \equiv \ln\frac{\mu}{\sqrt{p_T^{\text{cut}}\tilde{p}_T^{\text{cut}}}}\,. \tag{3.16}$$

It is straightforward to check that the one-loop finite term vanishes (see appendix A.4),

$$\mathcal{S}_{i,1} = 0\,. \tag{3.17}$$

The two-loop finite term is a generic function of the dimensionless ratio ρ and the jet radius parameter R, which must satisfy $\mathcal{S}_{i,2}(\rho=1,R)=0$. As usual, we can decompose it according to its R dependence as

$$\mathcal{S}_{i,2}(\rho,R) = -8C_i c_{ii}^R\,\ln\rho\ln R + \mathcal{S}_{i,2}^{(c)}(\rho) + \mathcal{O}(R^2)\,, \tag{3.18}$$

where c_{ii}^R is given by eq. (2.31) and $C_i = C_F$ (C_A) for $i = q$ (g). The coefficient of $\ln R$ at this order is completely determined by the R dependence of the noncusp rapidity anomalous dimensions in eq. (3.14). The full two-loop finite term $\mathcal{S}_{i,2}(\rho,R)$ could readily be obtained numerically using the methods of refs. [62, 63], which would enable the full NNLL′ resummation.

This regime is again free of nonglobal logarithms and hence can easily be applied to phenomenological studies. It can be used to supplement the EFT setup from section 3.2, which enables the resummation of logarithms of the ratio $p_T^{\text{cut}}/Q \sim \tilde{p}_T^{\text{cut}}/Q$, with an additional resummation of logarithms of the ratio $p_T^{\text{cut}}/Qe^{-\eta_{\text{cut}}} \sim \tilde{p}_T^{\text{cut}}/Qe^{-\eta_{\text{cut}}}$ by choosing the canonical scales

$$\begin{aligned}&\mu_B \sim \tilde{p}_T^{\text{cut}}\,, \quad \mu_{\mathcal{S}} \sim \sqrt{p_T^{\text{cut}}\tilde{p}_T^{\text{cut}}}\,, \qquad \mu_S \sim p_T^{\text{cut}}\,, \\ &\nu_B \sim Q\,, \qquad \nu_{\mathcal{S}} \sim \sqrt{p_T^{\text{cut}}\tilde{p}_T^{\text{cut}}}\,e^{\eta_{\text{cut}}}\,, \quad \nu_S \sim p_T^{\text{cut}}\,.\end{aligned} \tag{3.19}$$

Here, the rapidity evolution between $\nu_{\mathcal{S}}$ and ν_S is responsible for resumming the large logarithms of $e^{-\eta_{\text{cut}}} \sim \nu_S/\nu_{\mathcal{S}}$.

JHEP04(2019)142

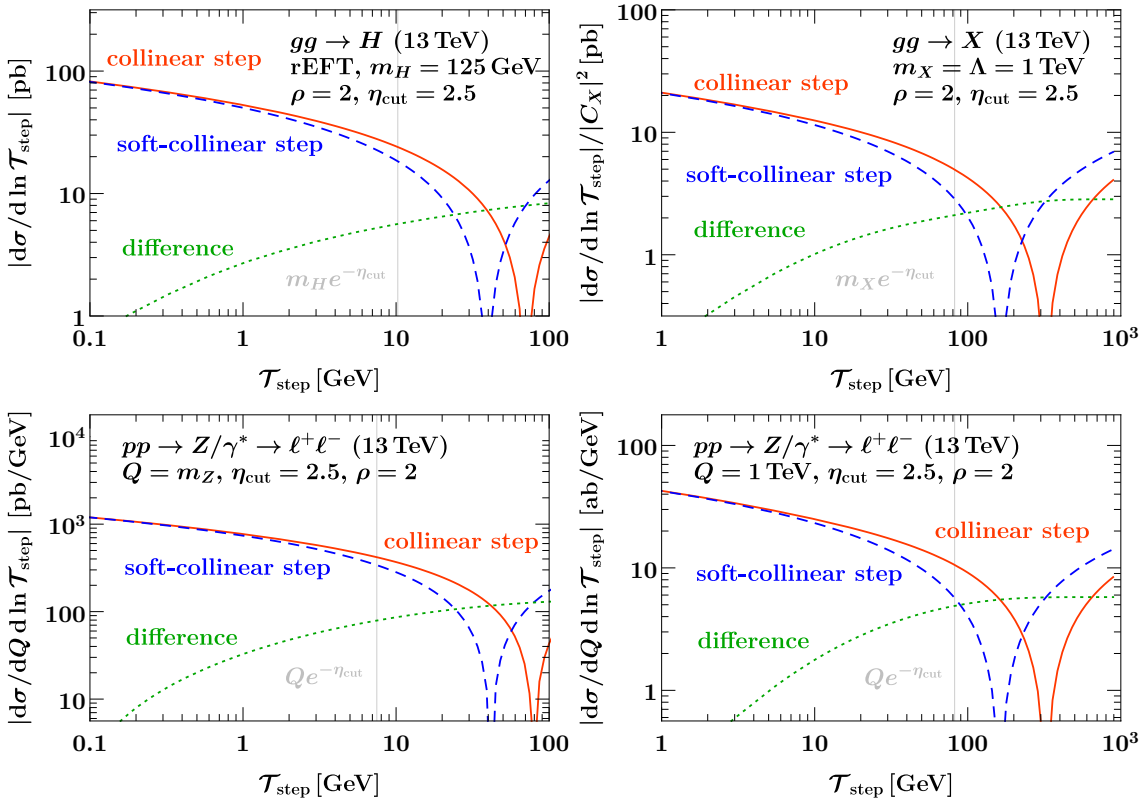

Figure 9. Comparison of the singular contributions to the fixed $\mathcal{O}(\alpha_s)$ (LO_1) $\mathcal{T}_{\rm step}$ spectrum for $\eta_{\rm cut} = 2.5$ and $\rho = 2$ for $gg \to H$ (top left), $gg \to X$ (top right), and Drell-Yan at $Q = m_Z$ (bottom left) and $Q = 1\,\mathrm{TeV}$ (bottom right). The solid orange lines show the singular spectrum for the collinear-step regime and the blue dashed lines the further factorized result in the soft-collinear-step regime. Their difference, shown by the dotted green lines vanishes as a power of $\mathcal{T}_{\rm step}$. The vertical lines indicate where the parametric relation $\mathcal{T}_{\rm step}/Q = e^{-\eta_{\rm cut}}$ is satisfied.

Numerical validation. To validate our setup in this regime, we exploit that eq. (3.13) provides a refactorization of the collinear step in eq. (3.2), where

$$\mathcal{I}_{ij}(p_T^{\rm cut}, \tilde{p}_T^{\rm cut}, \eta_{\rm cut}, R, \omega, z, \mu, \nu) = \mathcal{S}_i(p_T^{\rm cut}, \tilde{p}_T^{\rm cut}, \eta_{\rm cut}, R, \mu, \nu)\, \mathcal{I}_{ij}(p_T^{\rm cut}, R, \omega, z, \mu, \nu) \times \left[1 + \mathcal{O}\left(\frac{p_T^{\rm cut}}{\omega e^{-\eta_{\rm cut}}}, \frac{\tilde{p}_T^{\rm cut}}{\omega e^{-\eta_{\rm cut}}}, R^2\right)\right]. \tag{3.20}$$

In particular, eq. (3.13) must reproduce eq. (3.2) up to power corrections in $p_T^{\rm cut}/Qe^{-\eta_{\rm cut}}$ and $\tilde{p}_T^{\rm cut}/Qe^{-\eta_{\rm cut}}$. We can test this numerically using the $\mathcal{T}_{\rm step}$ observable defined in section 3.2, which simultaneously probes both classes of power corrections. In figure 9, we show the fixed $\mathcal{O}(\alpha_s)$ $\mathcal{T}_{\rm step}$ spectra for the collinear step (solid orange) and soft-collinear step (dashed blue). In all cases their difference (dotted green) vanishes like a power in $\mathcal{T}_{\rm step}$.

The additional resummation using the soft-collinear step may be applicable up to values of $p_T^{\rm cut} = 20\,\mathrm{GeV}$ ($p_T^{\rm cut} = 80\,\mathrm{GeV}$) for $Q \sim 100\,\mathrm{GeV}$ ($Q = 1\,\mathrm{TeV}$), for the choice of $\rho = 2, \eta_{\rm cut} = 2.5$ displayed in figure 9. This can be read off from the relative size of leading-power (soft-collinear step) and subleading power (difference) contributions, which

JHEP04(2019)142

leave some room where resummation in the leading-power cross section can improve the prediction. We find a slightly larger potential resummation region than for the analogous refactorization in the $\tilde{p}_T^{\text{cut}} = \infty$ case, where an earlier onset of the power corrections was observed in figure 6.

3.5 $p_T^{\text{cut}}/Q \ll \tilde{p}_T^{\text{cut}}/Q \ll e^{-\eta_{\text{cut}}}$ (soft-collinear NGLs)

For this hierarchy (bottom right panel of figure 7), two types of soft-collinear modes arise,

$$\begin{aligned} n_a\text{-soft-collinear } (p_T^{\text{cut}}): &\quad p^\mu \sim p_T^{\text{cut}}(e^{-\eta_{\text{cut}}}, e^{\eta_{\text{cut}}}, 1)\,, \\ n_a\text{-soft-collinear } (\tilde{p}_T^{\text{cut}}): &\quad p^\mu \sim \tilde{p}_T^{\text{cut}}(e^{-\eta_{\text{cut}}}, e^{\eta_{\text{cut}}}, 1)\,, \end{aligned} \tag{3.21}$$

and analogously for the n_b-soft-collinear sectors, which are both parametrically distinct from the energetic collinear modes. Compared to the regime $p_T^{\text{cut}} \sim \tilde{p}_T^{\text{cut}} \ll Qe^{-\eta_{\text{cut}}}$ there are now parametrically large logarithms $\ln(p_T^{\text{cut}}/\tilde{p}_T^{\text{cut}})$ in the soft-collinear function $\mathcal{S}_i$ in eq. (3.13). The cross section can be written as in eq. (3.13), where the soft-collinear function is refactorized as

$$\begin{aligned} \mathcal{S}_i(p_T^{\text{cut}}, \tilde{p}_T^{\text{cut}}, \eta_{\text{cut}}, R, \mu, \nu) = \mathcal{S}_i^{(\text{cut})}(p_T^{\text{cut}}, \eta_{\text{cut}}, R, \mu, \nu) \left[\mathcal{S}_i^{(\text{cut})}(\tilde{p}_T^{\text{cut}}, \eta_{\text{cut}}, R, \mu, \nu)\right]^{-1} \\ \times \left[1 + \mathcal{S}_i^{(\text{NG})}\left(\frac{p_T^{\text{cut}}}{\tilde{p}_T^{\text{cut}}}, R\right)\right] \times \left[1 + \mathcal{O}\left(\frac{p_T^{\text{cut}}}{\tilde{p}_T^{\text{cut}}}\right)\right], \end{aligned} \tag{3.22}$$

with $\mathcal{S}_i^{(\text{cut})}$ the same soft-collinear function as in eqs. (2.37) and (3.10). Both the power corrections and the nonglobal piece $\mathcal{S}_i^{(\text{NG})}$ are absent at one loop and at $\mathcal{O}(\alpha_s^2 \ln R)$. Equivalently this regime can be interpreted as a refactorization of eq. (3.10), where compared to the hierarchy for $p_T^{\text{cut}} \ll \tilde{p}_T^{\text{cut}} \sim Qe^{-\eta_{\text{cut}}}$ there are large (rapidity) logarithms $\ln(\tilde{p}_T^{\text{cut}} e^{\eta_{\text{cut}}}/Q)$ in the beam function $B_i^{(\text{cut})}$. Evolving the two soft-collinear functions to separate renormalization scales $\mu_{\mathcal{S},1} = p_T^{\text{cut}}$, $\nu_{\mathcal{S},1} = p_T^{\text{cut}} e^{\eta_{\text{cut}}}$ and $\mu_{\mathcal{S},2} = \tilde{p}_T^{\text{cut}}$, $\nu_{\mathcal{S},2} = \tilde{p}_T^{\text{cut}} e^{\eta_{\text{cut}}}$ resums Sudakov logarithms of $p_T^{\text{cut}}/\tilde{p}_T^{\text{cut}}$, but does not account for the nonglobal logarithms of the same ratio in $\mathcal{S}_i^{(\text{NG})}$.

4 Numerical results

In section 2 we discussed in detail how to incorporate the jet rapidity cut into the resummed 0-jet cross section. In particular, in the regime $p_T^{\text{cut}}/Q \sim e^{-\eta_{\text{cut}}}$ (regime 2), the dependence on η_{cut} is incorporated into the resummation via the RG evolution of the η_{cut} dependent beam functions. In this section, we illustrate these results by presenting numerical predictions for the resummed cross section at NLL′+NLO.

In section 4.1, we outline how the resummed results are combined with the full QCD results, as well as our estimation of perturbative uncertainties. In section 4.2, we assess the impact of the additional perturbative ingredients by comparing the different treatments of η_{cut}. In section 4.3, we show the predictions for selected η_{cut} as a function of p_T^{cut}.

In the following, we consider the four cases of gluon-fusion Higgs production $gg \to H$ at $m_H = 125\,\text{GeV}$, gluon fusion to a generic heavy scalar $gg \to X$ with $m_X = 1\,\text{TeV}$,

JHEP04(2019)142

and Drell-Yan production at $Q = m_Z$ and $Q = 1\,\text{TeV}$, with the same setup and inputs as described in section 2.3. The numerical results for the resummed predictions for all processes are obtained from our implementation in `SCETlib` [37]. The NLO results in full QCD are obtained from `MCFM 8.0` [38–40].

4.1 Fixed-order matching and perturbative uncertainties

The resummed cross section obtained from eq. (2.12) describes the 0-jet cross section up to power corrections in p_T^{cut}/Q, which become relevant when $p_T^{\text{cut}} \sim Q$. We account for them by the usual additive matching,

$$\sigma_0(p_T^{\text{cut}}, \eta_{\text{cut}}) = \sigma_0^{\text{res}}(p_T^{\text{cut}}, \eta_{\text{cut}}) + \left[\sigma_0^{\text{FO}}(p_T^{\text{cut}}, \eta_{\text{cut}}) - \sigma_0^{\text{sing}}(p_T^{\text{cut}}, \eta_{\text{cut}})\right]. \tag{4.1}$$

Here, σ_0^{res} is the resummed singular cross section obtained from eq. (2.12), σ_0^{sing} is its fixed-order expansion, and σ_0^{FO} is the fixed-order result in full QCD. By construction, the difference in square brackets is nonsingular and vanishes as $p_T^{\text{cut}} \to 0, \eta_{\text{cut}} \to \infty$ and can therefore be included at fixed order even at small p_T^{cut}. The dominant corrections at small p_T^{cut} are resummed in σ_0^{res}. At large p_T^{cut}, fixed-order perturbation theory is the appropriate description, so eq. (4.1) should recover σ_0^{FO}. This is achieved by turning off the resummation in σ_0^{res} as a function of p_T^{cut}, and by constructing σ_0^{res} such that it precisely reproduces σ^{sing} when the resummation is fully turned off.

To smoothly turn off the resummation as we approach $p_T^{\text{cut}} \to Q$, we use profile scales [64, 65], following the setup developed in ref. [13]. We stress that the profile scales for regime 2 are in one-to-one correspondence with the standard treatment in regime 1, since both regimes have the same RG structure. Similarly, our treatment of perturbative uncertainties is based on profile scale variations following ref. [13]. We distinguish an overall yield uncertainty $\Delta_{\mu 0}$, which is determined by a collective variation of all scales up and down, and a resummation (jet bin migration) uncertainty Δ_{resum} from varying individual scales in the beam and soft functions. For the gluon-induced processes, we follow ref. [66] and include an additional uncertainty Δ_φ from varying the complex phase of the hard scale, which was not considered in ref. [13]. The total uncertainty is then obtained by considering the different uncertainty sources as independent, and hence uncorrelated, and adding them in quadrature,

$$\Delta_{\text{total}} = \Delta_{\mu 0} \oplus \Delta_\varphi \oplus \Delta_{\text{resum}} \equiv \left(\Delta_{\mu 0}^2 + \Delta_\varphi^2 + \Delta_{\text{resum}}^2\right)^{1/2}. \tag{4.2}$$

4.2 Comparing different treatments of the jet rapidity cut

It is interesting to consider the impact of the additional perturbative ingredients in the η_{cut} dependent beam function on the prediction, e.g. compared to treating the rapidity cut effects purely at fixed order. In figures 10 and 11, we plot the results for fixed p_T^{cut} as a function of η_{cut} starting at $\eta_{\text{cut}} = \infty$ on the left and decreasing toward the right. The corresponding values of the $Qe^{-\eta_{\text{cut}}}$ scale are shown at the top.

Our result for the 0-jet cross section using the matching in eq. (4.1) is shown as orange bands. We refer to this prediction as NLL′(η_{cut})+NLO(η_{cut}), because both the NLL′ resummed singular cross section and the fixed-order matching are exact in η_{cut}. To

JHEP04(2019)142

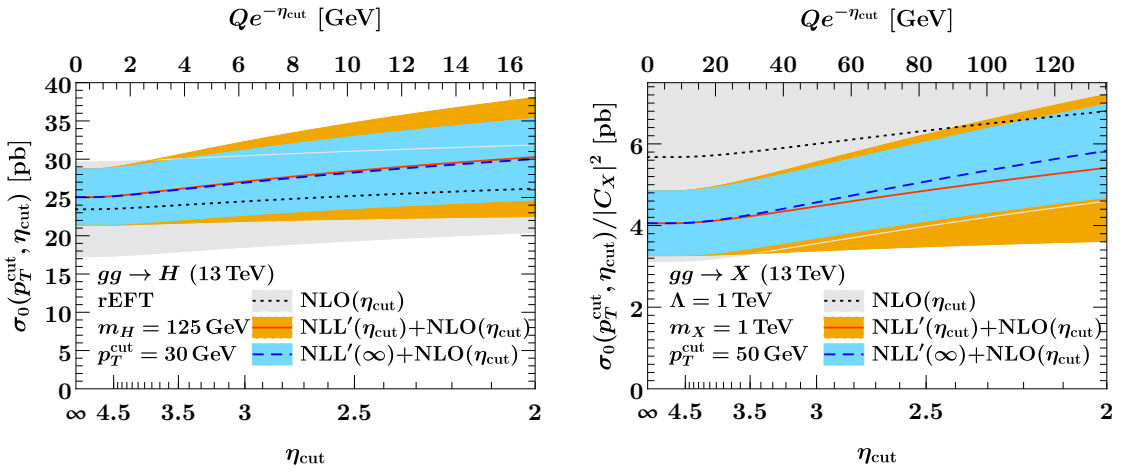

Figure 10. The 0-jet cross section for $gg \to H$ at $m_H = 125\,\text{GeV}$ for $p_T^{\rm cut} = 30\,\text{GeV}$ (left) and $gg \to X$ at $m_X = 1\,\text{TeV}$ and $p_T^{\rm cut} = 50\,\text{GeV}$ (right) as a function of $\eta_{\rm cut}$. The same observable (σ_0) is calculated in three different ways, shown by the different bands, as described in the text.

highlight the effect of the additional $\eta_{\rm cut}$ dependence in the regime 2 beam function, we consider two more alternative treatments of $\eta_{\rm cut}$. For the regime 1 result, shown by the blue bands and denoted by NLL′(∞)+NLO($\eta_{\rm cut}$), the $\eta_{\rm cut}$ dependence in the resummed cross section is dropped,

$$\sigma_0(p_T^{\rm cut}, \eta_{\rm cut}) = \sigma_0^{\rm res}(p_T^{\rm cut}, \infty) + \left[\sigma_0^{\rm FO}(p_T^{\rm cut}, \eta_{\rm cut}) - \sigma_0^{\rm sing}(p_T^{\rm cut}, \infty)\right]. \tag{4.3}$$

The resummation then only acts on the singular cross section for $\eta_{\rm cut} = \infty$, while all $\eta_{\rm cut}$ effects are included purely at fixed order via the matching term in square brackets. Note that the matching term is now no longer nonsingular, i.e., it no longer vanishes like a power in $p_T^{\rm cut}$ as $p_T^{\rm cut} \to 0$, as we saw in figures 4 and 5. The plain fixed-order calculation without any resummation,

$$\sigma_0(p_T^{\rm cut}, \eta_{\rm cut}) = \sigma_0^{\rm FO}(p_T^{\rm cut}, \eta_{\rm cut}), \tag{4.4}$$

is denoted by NLO($\eta_{\rm cut}$) and shown by the gray bands. In this case, the uncertainties are evaluated using the ST procedure [3].

We first consider gluon-fusion Higgs production shown in the left panel of figure 10, where we set $p_T^{\rm cut} = 30\,\text{GeV}$. The NLO($\eta_{\rm cut}$) prediction (gray band) exhibits a slight, physical rise in the cross section as $\eta_{\rm cut}$ decreases towards the right. This is not surprising as at fixed order, decreasing $\eta_{\rm cut}$ simply amounts to accumulating the squared LO_1 matrix element over a larger part of phase space. The rise is less pronounced than for the resummed results (orange and blue bands), but still compatible with them within each others' uncertainties. Comparing NLL′($\eta_{\rm cut}$)+NLO($\eta_{\rm cut}$) (orange) to NLL′(∞)+NLO($\eta_{\rm cut}$) (blue) we find that the additional tower of logarithms predicted by NLL′($\eta_{\rm cut}$) on top of the fixed NLO $\eta_{\rm cut}$ dependence barely affects the central value of the prediction down to $\eta_{\rm cut} = 2$. This is perhaps not surprising since $Qe^{-\eta_{\rm cut}}$ is at most half of $p_T^{\rm cut}$, which means we are not far from regime 1. However, we do observe a noticeable increase in the perturbative

JHEP04(2019)142

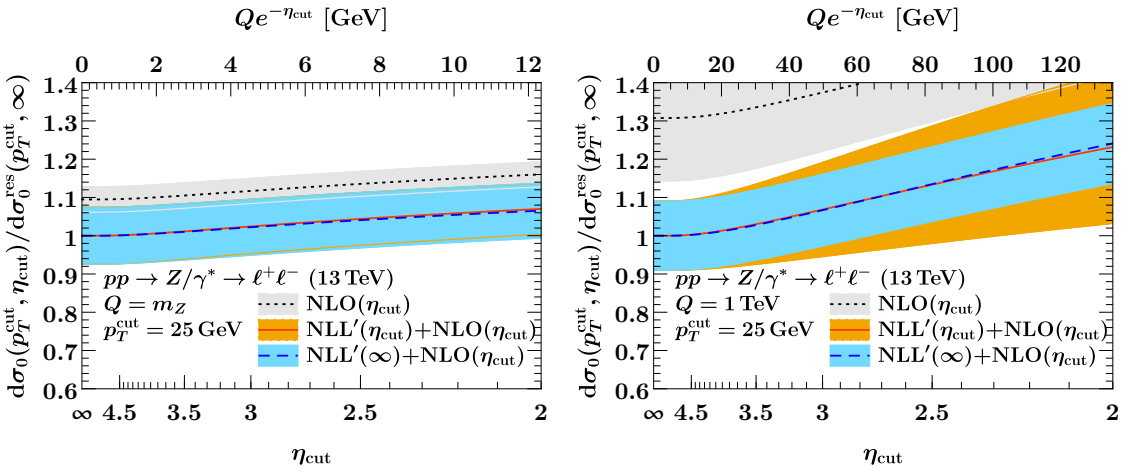

Figure 11. The 0-jet cross section for Drell-Yan at $Q = m_Z$ and $p_T^{\rm cut} = 20\,\text{GeV}$ (left) and $Q = 1\,\text{TeV}$ and $p_T^{\rm cut} = 25\,\text{GeV}$ (right) as a function of $\eta_{\rm cut}$. The same observable (σ_0) is calculated in three different ways, shown by the different bands, as described in the text. For better readability, all results are normalized to the resummed central value at $\eta_{\rm cut} = \infty$.

uncertainty estimate. This is mainly due to the resummation uncertainty, which is reasonable: $\Delta_{\rm resum}$ probes the unknown higher-order finite terms (the RGE boundary condition) and is therefore sensitive to a change of the beam function boundary condition by the $\eta_{\rm cut}$ correction $\Delta I_{ij}^{(1)}$ (see section 2.3). On the other hand, $\Delta I_{ij}^{(1)}$ must be large enough to accommodate — up to power corrections — the fixed-order difference to $\eta_{\rm cut} = \infty$ (roughly 2 pb at $\eta_{\rm cut} = 2.5$, as can be read off from the gray line), so we expect an impact on $\Delta_{\rm resum}$ of similar size. Hence, the conclusion is not that the NLL′(∞)+NLO($\eta_{\rm cut}$) result is more precise, but rather that its uncertainty is potentially underestimated because it cannot capture the $\eta_{\rm cut}$ dependence.

In the right panel of figure 10, we show the same results for a hypothetical color-singlet scalar resonance $gg \to X$ at $m_X = 1\,\text{TeV}$ using $p_T^{\rm cut} = 50\,\text{GeV}$. [The dimension-five operator mediating the production of X is given in eq. (2.33).] The NLO($\eta_{\rm cut}$) result (gray) is now off by a large amount already at $\eta_{\rm cut} = \infty$, where it is not covered by the resummed predictions. This is expected because the high production energy of 1 TeV implies we are deep in the resummation region, even for the larger value of $p_T^{\rm cut} = 50\,\text{GeV}$. The central values of the two resummed treatments start to differ below $\eta_{\rm cut} = 3$ or above $Qe^{-\eta_{\rm cut}} \simeq 50\,\text{GeV}$, where we are now fully in regime 2. However, the main difference is again the larger and likely more reliable uncertainty estimate in the NLL′($\eta_{\rm cut}$) prediction.

In figure 11 we show the analogous results for Drell-Yan production at $Q = m_Z$ using $p_T^{\rm cut} = 20\,\text{GeV}$ (left panel) and $Q = 1\,\text{TeV}$ using $p_T^{\rm cut} = 25\,\text{GeV}$ (right panel). For better readability, these results are normalized to the resummed 0-jet cross section at $\eta_{\rm cut} = \infty$. While all predictions agree in the slope of the cross section with respect to $\eta_{\rm cut}$, the NLO($\eta_{\rm cut}$) result has a constant offset and an unrealistically small uncertainty estimate. At the lower $Q \sim 100\,\text{GeV}$, we find practically no difference between the NLL′($\eta_{\rm cut}$) and NLL′(∞) calculations, so here the effects of the jet rapidity cut can safely be included

JHEP04(2019)142

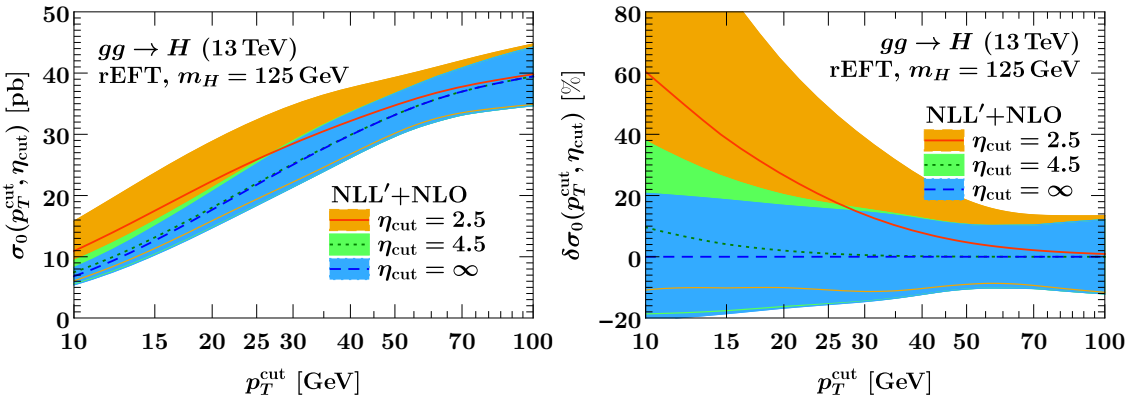

Figure 12. 0-jet cross section $\sigma_0(p_T^{\rm cut}, \eta_{\rm cut})$ for $gg \to H$ for $m_H = 125\,\text{GeV}$ at NLL′+NLO for different values of $\eta_{\rm cut}$. The bands indicate the total uncertainty $\Delta_{\mu 0} \oplus \Delta_\varphi \oplus \Delta_{\rm res}$. The absolute cross section is shown on the left. On the right, the same results are shown as the percent difference relative to the 0-jet cross section at $\eta_{\rm cut} = \infty$.

$\sigma_0(p_T^{\rm cut}, \eta_{\rm cut})$ [pb], $gg \to H$ (13 TeV), rEFT, $m_H = 125\,\text{GeV}$		
$\eta_{\rm cut}$	$p_T^{\rm cut} = 25\,\text{GeV}$	$p_T^{\rm cut} = 30\,\text{GeV}$
2.5	$25.9 \pm 3.8_{\mu 0} \pm 1.5_{\varphi} \pm 5.0_{\rm res}$ (25.0%)	$28.5 \pm 4.0_{\mu 0} \pm 1.6_{\varphi} \pm 4.6_{\rm res}$ (22.0%)
4.5	$22.0 \pm 2.0_{\mu 0} \pm 1.0_{\varphi} \pm 2.8_{\rm res}$ (16.2%)	$25.2 \pm 2.2_{\mu 0} \pm 1.2_{\varphi} \pm 2.8_{\rm res}$ (15.0%)
∞	$21.8 \pm 1.9_{\mu 0} \pm 1.0_{\varphi} \pm 2.7_{\rm res}$ (15.6%)	$25.0 \pm 2.2_{\mu 0} \pm 1.2_{\varphi} \pm 2.7_{\rm res}$ (14.7%)

Table 1. 0-jet cross section for $gg \to H$ for $m_H = 125\,\text{GeV}$ at NLL′+NLO for different values of $p_T^{\rm cut}$ and $\eta_{\rm cut}$ with a breakdown of the uncertainties.

via the fixed-order matching corrections to the regime 1 resummation. At higher production energies, the intrinsic NLL′($\eta_{\rm cut}$) ingredients become more relevant, similar to gluon-fusion, as shown by the increasing uncertainty estimates as $\eta_{\rm cut}$ decreases. Note that below $\eta_{\rm cut} = 2.5$, $Qe^{-\eta_{\rm cut}} \gtrsim 80\,\text{GeV}$ becomes large compared to this choice of $p_T^{\rm cut} = 25\,\text{GeV}$, so resumming logarithms of $p_T^{\rm cut}/(Qe^{-\eta_{\rm cut}})$ using the regime 3 factorization given in section 2.4 might help reduce the uncertainties.

4.3 Resummed predictions with a sharp rapidity cut

Here, we compare predictions for different values of $\eta_{\rm cut}$ as a function of $p_T^{\rm cut}$. Our working order is NLL′($\eta_{\rm cut}$)+NLO($\eta_{\rm cut}$) in the notation of the previous section, which from now on we simply refer to as NLL′+NLO, i.e., the $\eta_{\rm cut}$ dependence is always included in the resummation. We stress that the differences we observe between predictions in this subsection are physical differences due to the different jet rapidity cuts, and *not* due to different theoretical treatments as in the previous subsection.

In figure 12 and table 1 we present results for $gg \to H$. Going from $\eta_{\rm cut} = \infty$ to $\eta_{\rm cut} = 4.5$ we find a 1% increase of the cross section for the typical values of $p_T^{\rm cut} = 25\,\text{GeV}$ and 30 GeV. At $\eta_{\rm cut} = 2.5$ the increase becomes more sizable, 14% (19%) for $p_T^{\rm cut} = 30\,\text{GeV}$ (25 GeV). The differences vanish as the cross section saturates around $p_T^{\rm cut} \sim 100\,\text{GeV}$.

JHEP04(2019)142

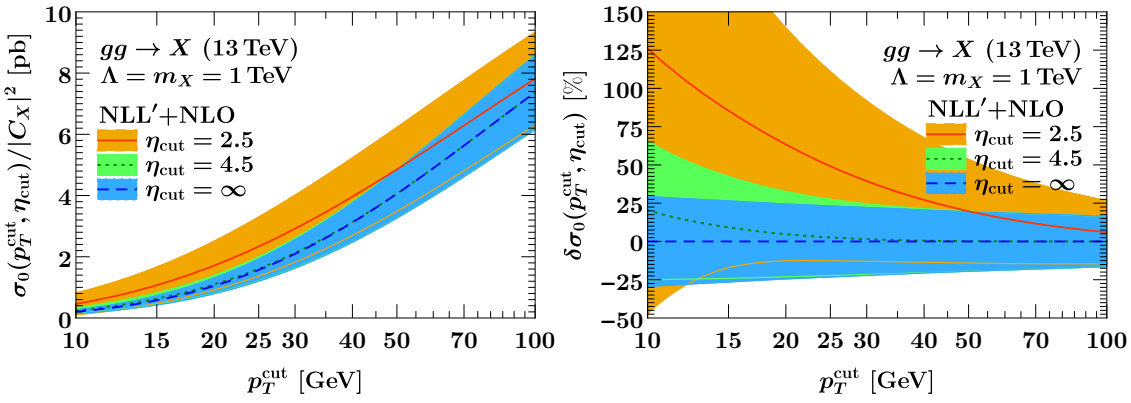

Figure 13. 0-jet cross section $\sigma_0(p_T^{\rm cut}, \eta_{\rm cut})$ for $gg \to X$ for $m_X = 1\,\text{TeV}$ at NLL′+NLO for different values of $\eta_{\rm cut}$. The bands indicate the total uncertainty $\Delta_{\mu 0} \oplus \Delta_\varphi \oplus \Delta_{\rm res}$. The absolute cross section is shown on the left. On the right, the same results are shown as the percent difference relative to the 0-jet cross section at $\eta_{\rm cut} = \infty$.

$\sigma_0(p_T^{\rm cut}, \eta_{\rm cut})/\lvert C_X\rvert^2$ [pb], $gg \to X$ (13 TeV), $\Lambda = m_X = 1$ TeV		
$\eta_{\rm cut}$	$p_T^{\rm cut} = 50\,\text{GeV}$	$p_T^{\rm cut} = 100\,\text{GeV}$
2.5	$4.9 \pm 0.7_{\mu 0} \pm 0.1_{\varphi} \pm 1.2_{\rm res}$ (28.3%)	$7.8 \pm 0.8_{\mu 0} \pm 0.1_{\varphi} \pm 1.3_{\rm res}$ (19.4%)
4.5	$4.1 \pm 0.3_{\mu 0} \pm 0.1_{\varphi} \pm 0.7_{\rm res}$ (19.6%)	$7.4 \pm 0.6_{\mu 0} \pm 0.1_{\varphi} \pm 1.1_{\rm res}$ (16.4%)
∞	$4.1 \pm 0.3_{\mu 0} \pm 0.1_{\varphi} \pm 0.7_{\rm res}$ (19.5%)	$7.4 \pm 0.6_{\mu 0} \pm 0.1_{\varphi} \pm 1.1_{\rm res}$ (16.4%)

Table 2. 0-jet cross section for $gg \to X$ for $m_X = 1\,\text{TeV}$ at NLL′+NLO for different values of $p_T^{\rm cut}$ and $\eta_{\rm cut}$ with a breakdown of the uncertainties.

The analogous results for $gg \to X$ for $m_X = 1\,\text{TeV}$ are shown in figure 13 and table 2. At such a high hard scale, the uncertainties for $\eta_{\rm cut} = 2.5$ become essentially beyond control for very tight vetoes $p_T^{\rm cut} \lesssim 25\,\text{GeV}$, which would make an additional resummation of $\ln p_T^{\rm cut}/(Qe^{-\eta_{\rm cut}})$ as outlined in section 2.4 necessary. As we will see in the next subsection, this effect can be tamed by replacing the sharp rapidity cut by a step in the jet veto. However, for any choice of $\eta_{\rm cut}$ the cross section is very strongly Sudakov suppressed for such small values of $p_T^{\rm cut}$. At more realistic values of the veto, the jet rapidity cut for $\eta_{\rm cut} = 2.5$ compared to $\eta_{\rm cut} = \infty$ still leads to a sizable increase of 20% (5%) for $p_T^{\rm cut} = 50\,\text{GeV}$ ($p_T^{\rm cut} = 100\,\text{GeV}$). In contrast, the effect for $\eta_{\rm cut} = 4.5$ is very small.

The results for Drell-Yan production are given in figure 14 and table 3. For $Q = m_Z$ (top rows), we find a 5–7% increase in the cross section at $\eta_{\rm cut} = 2.5$ for $p_T^{\rm cut} = 20$–$25\,\text{GeV}$. Here the uncertainty for $\eta_{\rm cut} = 2.5$ is under good control even down to $p_T^{\rm cut} \sim 10\,\text{GeV}$. For $Q = 1\,\text{TeV}$ (bottom rows), the cross section for $\eta_{\rm cut} = 2.5$ increases by 14% (4%) for $p_T^{\rm cut} = 25\,\text{GeV}$ (50 GeV) compared to $\eta_{\rm cut} = \infty$. The Sudakov suppression and the accompanying increase in relative uncertainty at small $p_T^{\rm cut}$ are weaker than for $gg \to X$ due to the smaller color factor (C_F vs. C_A) in the Sudakov exponent, but are still substantial for a quark-induced process. The effect of the rapidity cut at $\eta_{\rm cut} = 4.5$ is negligible.

JHEP04(2019)142

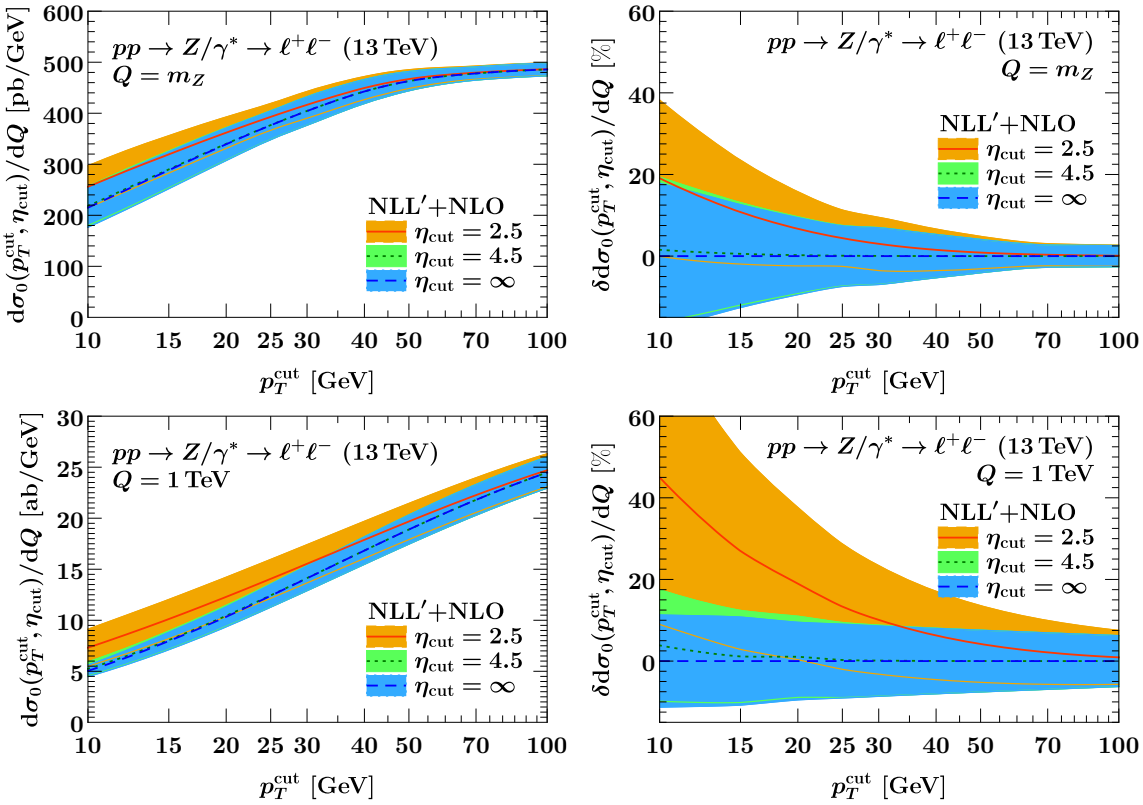

Figure 14. The 0-jet cross section $\mathrm{d}\sigma_0(p_T^{\rm cut}, \eta_{\rm cut})/\mathrm{d}Q$ for Drell-Yan production at the Z pole $Q = m_Z$ (top row) and at $Q = 1\,\mathrm{TeV}$ (bottom row) at NLL′+NLO for different values of $\eta_{\rm cut}$. The bands indicate the total uncertainty $\Delta_{\mu 0} \oplus \Delta_{\rm res}$. The absolute cross section is shown on the left. On the right, the same results are shown as the percent difference relative to the 0-jet cross section at $\eta_{\rm cut} = \infty$.

$\mathrm{d}\sigma_0(p_T^{\rm cut}, \eta_{\rm cut})/\mathrm{d}Q$ [pb/GeV], $pp \to Z/\gamma^* \to \ell^+\ell^-$ (13 TeV), $Q = m_Z$		
$\eta_{\rm cut}$	$p_T^{\rm cut} = 20\,\mathrm{GeV}$	$p_T^{\rm cut} = 25\,\mathrm{GeV}$
2.5	$362 \pm 22_{\mu 0} \pm 21_{\rm res}$ (8.5%)	$393 \pm 22_{\mu 0} \pm 14_{\rm res}$ (6.6%)
4.5	$340 \pm 24_{\mu 0} \pm 22_{\rm res}$ (9.4%)	$377 \pm 24_{\mu 0} \pm 15_{\rm res}$ (7.4%)
∞	$339 \pm 24_{\mu 0} \pm 22_{\rm res}$ (9.5%)	$376 \pm 24_{\mu 0} \pm 15_{\rm res}$ (7.4%)

$\mathrm{d}\sigma_0(p_T^{\rm cut}, \eta_{\rm cut})/\mathrm{d}Q$ [ab/GeV], $pp \to Z/\gamma^* \to \ell^+\ell^-$ (13 TeV), $Q = 1\,\mathrm{TeV}$		
$\eta_{\rm cut}$	$p_T^{\rm cut} = 25\,\mathrm{GeV}$	$p_T^{\rm cut} = 50\,\mathrm{GeV}$
2.5	$14.1 \pm 0.8_{\mu} \pm 1.7_{\rm res}$ (13.6%)	$19.7 \pm 0.6_{\mu} \pm 1.7_{\rm res}$ (9.0%)
4.5	$12.4 \pm 0.4_{\mu} \pm 1.1_{\rm res}$ (9.2%)	$18.9 \pm 0.4_{\mu} \pm 1.4_{\rm res}$ (7.6%)
∞	$12.4 \pm 0.4_{\mu} \pm 1.1_{\rm res}$ (9.1%)	$18.9 \pm 0.4_{\mu} \pm 1.4_{\rm res}$ (7.6%)

Table 3. The 0-jet cross section for Drell-Yan production at the Z pole $Q = m_Z$ (top) and at $Q = 1\,\mathrm{TeV}$ (bottom) at NLL′+NLO for different values of $p_T^{\rm cut}$ and $\eta_{\rm cut}$ with a breakdown of the uncertainties.

JHEP04(2019)142

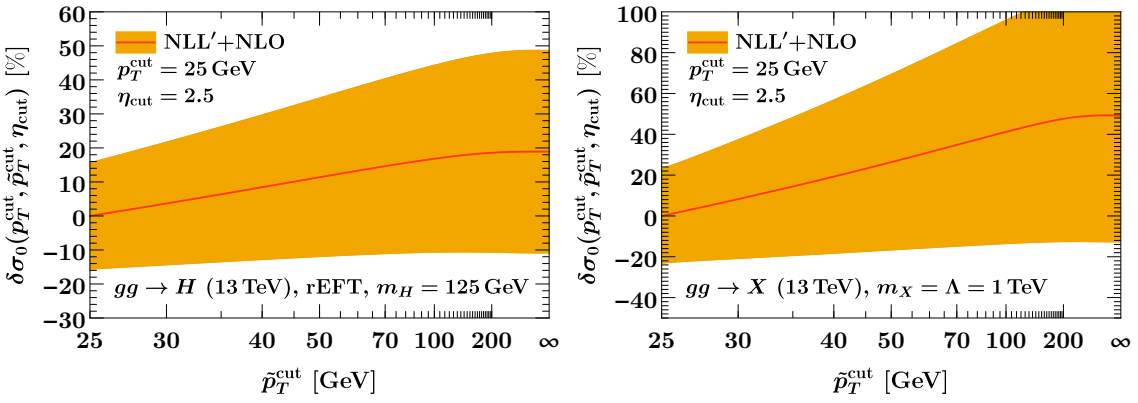

Figure 15. 0-jet cross section $\sigma_0(p_T^{\rm cut}, \tilde{p}_T^{\rm cut}, \eta_{\rm cut})$ with a step at $\eta_{\rm cut} = 2.5$ for $gg \to H$ (left panel) and $gg \to X$ (right panel) at NLL′+NLO. The results are shown for a fixed central veto at $p_T^{\rm cut} = 25\,\text{GeV}$ as a function of the jet veto $\tilde{p}_T^{\rm cut}$ that is applied beyond $\eta_{\rm cut}$. We show the percent differences relative to the result for a uniform veto $\tilde{p}_T^{\rm cut} = p_T^{\rm cut}$. The bands indicate the total uncertainty $\Delta_{\mu 0} \oplus \Delta_\varphi \oplus \Delta_{\rm res}$.

4.4 Resummed predictions with a step in the jet veto

In the previous subsection we have seen that a sharp rapidity cut at $\eta_{\rm cut} = 2.5$ can lead to a substantial loss of precision in the theory predictions, especially for gluon-induced processes and at high production energies.

In figure 15 we show the resummed 0-jet cross section for $gg \to H$ and $gg \to X$ with a step in the jet veto at $\eta_{\rm cut} = 2.5$ as a function of the second jet veto parameter $\tilde{p}_T^{\rm cut}$ that is applied beyond $\eta_{\rm cut}$. The central jet veto below $\eta_{\rm cut}$ is fixed to $p_T^{\rm cut} = 25\,\text{GeV}$. On the left of the plot $\tilde{p}_T^{\rm cut} = p_T^{\rm cut}$, which is equivalent to having no rapidity cut, in which case the uncertainties are well under control. In the limit $\tilde{p}_T^{\rm cut} \to \infty$ (towards the right) the step becomes a sharp cut, corresponding to the results of the previous subsection. While the step in the jet veto still leads to an increase in the uncertainties, this can now be controlled by the choice of $\tilde{p}_T^{\rm cut}$. At this order, a small step from $p_T^{\rm cut} = 25\,\text{GeV}$ to $\tilde{p}_T^{\rm cut} = 30\,\text{GeV}$ only leads to a small increase in uncertainty. For a larger step to $\tilde{p}_T^{\rm cut} = 50\,\text{GeV} = 2p_T^{\rm cut}$, the uncertainties already increase substantially but are still much smaller than for a sharp cut.

5 Conclusion

We have developed a systematic framework to seamlessly incorporate a cut on the rapidity of reconstructed jets, $|\eta_{\rm jet}| < \eta_{\rm cut}$, into the theoretical description of jet-vetoed processes at the LHC. We have shown that the standard jet-veto resummation, which neglects the rapidity cut, is correct up to power corrections of $\mathcal{O}(Qe^{-\eta_{\rm cut}}/p_T^{\rm cut})$, with Q the hard-interaction scale and $p_T^{\rm cut}$ the jet veto cut.

We calculated the necessary $\eta_{\rm cut}$-dependent corrections at one loop as well as all logarithmic contributions to them at two loops (including both small-R clustering logarithms and all jet-veto logarithms predicted by the RGE; see section 2.3). The remaining ingredients required for a full NNLL′ analysis with $\eta_{\rm cut}$ effects are finite nonlogarithmic pieces that

JHEP04(2019)142

could be either calculated explicitly or extracted numerically from the full-QCD results, which we leave to future work. In addition, we considered for the first time the case of a step in the jet veto, i.e., an increase in the veto parameter to $\tilde{p}_T^{\text{cut}} > p_T^{\text{cut}}$ beyond η_{cut}, and showed how to similarly incorporate it into the jet-veto resummation (see section 3.2).

We also considered the jet veto cross section in the limit $p_T^{\text{cut}} \ll Qe^{-\eta_{\text{cut}}}$, corresponding to either very tight vetoes or very central rapidity cuts (see section 2.4). In this regime, the jet-veto resummation becomes impaired by the presence of nonglobal logarithms, requiring a refactorization of the cross section. However, we have argued that this parametric region will most likely not play a role for typical jet binning analyses at the LHC. If experimentally necessary, it can be avoided by replacing the sharp rapidity cut by a moderate step in the jet veto, which is free of nonglobal logarithms (see section 3.4).

There are several important outcomes of our analysis. First, a jet rapidity cut at very forward rapidities due to the finite detector acceptance, $\eta_{\text{cut}} \simeq 4.5$, is theoretically safe and unproblematic. In contrast, restricting the jet veto to the more central region, with a sharp rapidity cut at the end of the tracking detectors, $\eta_{\text{cut}} \simeq 2.5$, leads to an increase in the perturbative uncertainties (which may not be captured if the jet rapidity cut is not included in the resummation). This loss in theoretical precision can become particularly severe for gluon-induced processes and for processes at high scales. It can however be mitigated by replacing the sharp rapidity cut by a moderate step in the jet veto. We expect this to be a generic feature that also holds at higher orders. It will be interesting to extend our resummed predictions to the next order (NNLL$'$) to confirm this as well as to reduce the overall size of the theoretical uncertainties. We encourage our experimental colleagues to take full advantage of such step-like jet vetoes in order to benefit from suitably tight jet vetoes at central rapidities, while avoiding the increased pile-up contamination in the forward region.

Acknowledgments

We thank Daekyoung Kang, Yiannis Makris, Thomas Mehen, and Iain Stewart for discussions. This work was partially supported by the German Science Foundation (DFG) through the Emmy-Noether Grant No. TA 867/1-1 and the Collaborative Research Center (SFB) 676 Particles, Strings and the Early Universe.

A Perturbative ingredients

We collect known results for required anomalous dimensions in appendix A.1 and for the standard p_T^{cut} beam function without a jet rapidity cut in appendix A.2. In appendix A.3 we provide some details on the computation of the one-loop beam function matching coefficients in eqs. (2.25) and (2.38). In appendix A.4 we compute the soft-collinear functions given in eqs. (2.40) and (3.15). In appendix A.5 we compare to the one-loop results of ref. [34]. In appendix A.6 we discuss the Mellin convolutions required in the two-loop η_{cut} dependent beam function in eq. (2.24).

JHEP04(2019)142

A.1 Anomalous dimensions

We expand the β function of QCD as

$$\mu\frac{\mathrm{d}\alpha_s(\mu)}{\mathrm{d}\mu} = \beta[\alpha_s(\mu)]\,, \qquad \beta(\alpha_s) = -2\alpha_s\sum_{n=0}^{\infty}\beta_n\left(\frac{\alpha_s}{4\pi}\right)^{n+1}\,, \tag{A.1}$$

with the one-loop and two-loop coefficients in the $\overline{\text{MS}}$ scheme given by

$$\beta_0 = \frac{11}{3}\,C_A - \frac{4}{3}\,T_F\,n_f\,, \qquad \beta_1 = \frac{34}{3}\,C_A^2 - \left(\frac{20}{3}\,C_A + 4C_F\right)\,T_F\,n_f\,. \tag{A.2}$$

The cusp and all noncusp anomalous dimensions $\gamma(\alpha_s)$ are expanded as

$$\Gamma^i_{\text{cusp}}(\alpha_s) = \sum_{n=0}^{\infty}\Gamma^i_n\Big(\frac{\alpha_s}{4\pi}\Big)^{n+1}\,, \qquad \gamma(\alpha_s) = \sum_{n=0}^{\infty}\gamma_n\Big(\frac{\alpha_s}{4\pi}\Big)^{n+1}\,. \tag{A.3}$$

The coefficients of the $\overline{\text{MS}}$ cusp anomalous dimension through two loops are

$$\begin{aligned}
&\Gamma^q_n = C_F\Gamma_n\,, \qquad \Gamma^g_n = C_A\Gamma_n\,, \qquad (\text{for } n=0,1,2)\,,\\
&\Gamma_0 = 4\,,\\
&\Gamma_1 = 4\Big[C_A\Big(\frac{67}{9}-\frac{\pi^2}{3}\Big) - \frac{20}{9}\,T_F\,n_f\Big] = \frac{4}{3}\big[(4-\pi^2)C_A + 5\beta_0\big]\,.
\end{aligned} \tag{A.4}$$

The PDF anomalous dimension in eq. (2.23) is expanded as

$$P_{ij}(\alpha_s,z) = \sum_{n=0}^{\infty}P^{(n)}_{ij}(z)\left(\frac{\alpha_s}{4\pi}\right)^{n+1}\,. \tag{A.5}$$

Note that we expand the PDF anomalous dimension in $\alpha_s/(4\pi)$ and not $\alpha_s/(2\pi)$ as is often done. The one-loop coefficients of the PDF anomalous dimension read

$$\begin{aligned}
&P^{(0)}_{q_iq_j}(z) = P^{(0)}_{\bar q_i\bar q_j}(z) = 2C_F\,\delta_{ij}\,\theta(z)P_{qq}(z)\,, \quad && P^{(0)}_{gg}(z) = 2C_A\,\theta(z)P_{gg}(z) + \beta_0\,\delta(1-z)\,,\\
&P^{(0)}_{q_ig}(z) = P^{(0)}_{\bar q_ig}(z) = 2T_F\,\theta(z)P_{qg}(z)\,, && P^{(0)}_{gq_i}(z) = P^{(0)}_{g\bar q_i}(z) = 2C_F\,\theta(z)P_{gq}(z)\,,
\end{aligned} \tag{A.6}$$

in terms of the standard color-stripped one-loop QCD splitting functions

$$\begin{aligned}
P_{qq}(z) &= 2\mathcal{L}_0(1-z) - \theta(1-z)(1+z) + \frac{3}{2}\delta(1-z) &&= \left[\theta(1-z)\frac{1+z^2}{1-z}\right]_+\,,\\
P_{gg}(z) &= 2\mathcal{L}_0(1-z) + \theta(1-z)\left[2z(1-z) + \frac{2(1-z)}{z} - 2\right] &&= 2\mathcal{L}_0(1-z)\frac{(1-z+z^2)^2}{z}\,,\\
P_{qg}(z) &= \theta(1-z)\big[1-2z(1-z)\big]\,,\\
P_{gq}(z) &= \theta(1-z)\frac{1+(1-z)^2}{z}\,.
\end{aligned} \tag{A.7}$$

JHEP04(2019)142

The two-loop coefficients were calculated in refs. [67–69]. They can be decomposed as

$$\begin{aligned}
P^{(1)}_{q_i q_j}(z) &= P^{(1)}_{\bar{q}_i \bar{q}_j}(z) = 4C_F\,\theta(z)\big[\delta_{ij} P^1_{qqV}(z) + P^1_{qqS}(z)\big]\,,\\
P^{(1)}_{q_i g}(z) &= P^{(1)}_{\bar{q}_i g}(z) = 4T_F\,\theta(z)\,P^1_{qg}\,,\\
P^{(1)}_{q_i \bar{q}_j}(z) &= P^{(1)}_{\bar{q}_i q_j}(z) = 4C_F\,\theta(z)\big[\delta_{ij} P^1_{q\bar{q}V}(z) + P^1_{qqS}(z)\big]\,,\\
P^{(1)}_{gg}(z) &= 4\theta(z)\big[C_A P^1_{ggA} + T_F n_f\,P^1_{ggF}\big]\,,\\
P^{(1)}_{g q_i}(z) &= P^{(1)}_{g \bar{q}_i}(z) = 4C_F\theta(z)\,P^1_{gq}\,,
\end{aligned} \tag{A.8}$$

where explicit expressions for the P^1 functions on the right-hand side can be found in appendices A of refs. [70, 71]. [Note that in refs. [70, 71] the superscript "1" here is written as "(1)" there, and the PDF anomalous dimension is expanded there in $\alpha_s/(2\pi)$, which is already accounted for by the overall factors of 4 on the right-hand side of eq. (A.8).] Explicit results for the Mellin convolutions of two color-stripped leading-order splitting functions can also be found there.

The coefficients of the noncusp beam anomalous dimension are [13, 24]

$$\begin{aligned}
\gamma^q_{B\,0} &= 6C_F\,,\\
\gamma^q_{B\,1} &= C_F\bigg[(3 - 4\pi^2 + 48\zeta_3)C_F + \big(-14 + 16(1+\pi^2)\ln 2 - 96\zeta_3\big)C_A\\
&\qquad + \left(\frac{19}{3} - \frac{4}{3}\pi^2 + \frac{80}{3}\ln 2\right)\beta_0\bigg]\,,\\
\gamma^g_{B\,0} &= 2\beta_0\,,\\
\gamma^g_{B\,1} &= 2\beta_1 + 8C_A\left[\left(-\frac{5}{4} + 2(1+\pi^2)\ln 2 - 6\zeta_3\right)C_A + \left(\frac{5}{24} - \frac{\pi^2}{3} + \frac{10}{3}\ln 2\right)\beta_0\right]
\end{aligned} \tag{A.9}$$

The coefficients of the rapidity noncusp anomalous dimension depend on the jet radius R. They read [13]

$$\gamma^i_{\nu\,0}(R) = 0\,, \tag{A.10}$$

$$\gamma^i_{\nu\,1}(R) = -16C_i\left[\left(\frac{17}{9} - (1+\pi^2)\ln 2 + \zeta_3\right)C_A + \left(\frac{4}{9} + \frac{\pi^2}{12} - \frac{5}{3}\ln 2\right)\beta_0\right] + C_2^i(R)\,.$$

Here $C_i = C_F\,(C_A)$ for $i = q\,(g)$ and $C_2^i(R)$ is the clustering correction due to the jet algorithm relative to a global E_T veto, as computed in refs. [8, 13],

$$C_2^i(R) = 16C_i c_{ii}^R \ln R + 15.62\,C_i C_A - 9.17\,C_i\beta_0 + \mathcal{O}(R^2)\,. \tag{A.11}$$

The small-R clustering coefficient $c_{ii} = c_{gg} = c_{qq}$ is given in eq. (2.31).

A.2 Beam function master formula for $\eta_{\rm cut} \to \infty$

In analogy to eq. (2.21) the matching coefficient $\mathcal{I}_{ij}(p_T^{\rm cut}, R, \omega, z, \mu, \nu)$ of the $\eta_{\rm cut} \to \infty$ beam functions satisfies (suppressing all other arguments of $\mathcal{I}_{ij}$)

$$\begin{aligned}
\mu\frac{\mathrm{d}}{\mathrm{d}\mu}\mathcal{I}_{ij}(z) &= \gamma^i_B(\omega,\mu,\nu)\,\mathcal{I}_{ij}(z) - \sum_k \mathcal{I}_{ik}(z)\otimes_z 2P_{kj}[\alpha_s(\mu), z]\,,\\
\nu\frac{\mathrm{d}}{\mathrm{d}\nu}\mathcal{I}_{ij}(z) &= \gamma^i_{\nu,B}(p_T^{\rm cut}, R, \mu)\,\mathcal{I}_{ij}(z)\,.
\end{aligned} \tag{A.12}$$

JHEP04(2019)142

Solving this order by order in α_s yields the beam function master formula,

$$
\begin{aligned}
\mathcal{I}_{ij}(z) &= \delta_{ij}\delta(1-z) + \frac{\alpha_s(\mu)}{4\pi}\,\mathcal{I}_{ij}^{(1)}(z) + \frac{\alpha_s^2(\mu)}{(4\pi)^2}\,\mathcal{I}_{ij}^{(2)}(z) + \mathcal{O}(\alpha_s^3)\,,\\
\mathcal{I}_{ij}^{(1)}(z) &= \delta_{ij}\delta(1-z)\,L_B^\mu(2\Gamma_0^i L_B^\nu + \gamma_{B\,0}^i) - 2L_B^\mu P_{ij}^{(0)}(z) + I_{ij}^{(1)}(z)\,,\\
\mathcal{I}_{ij}^{(2)}(z) &= \delta_{ij}\delta(1-z)\Big\{(L_B^\mu)^2\left[2(\Gamma_0^i)^2(L_B^\nu)^2 + L_B^\nu(2\beta_0\Gamma_0^i + 2\Gamma_0^i\gamma_{B\,0}^i) + \beta_0\gamma_{B\,0}^i + \frac{(\gamma_{B\,0}^i)^2}{2}\right]\\
&\qquad + L_B^\mu\Big[2\Gamma_1^i L_B^\nu + \gamma_{B\,1}^i\Big] - \frac{1}{2}\gamma_{\nu\,1}^i(R)L_B^\nu\Big\}\\
&\quad + P_{ij}^{(0)}(z)\,(L_B^\mu)^2\Big[-4\Gamma_0^i L_B^\nu - 2\beta_0 - 2\gamma_{B\,0}^i\Big] + I_{ij}^{(1)}(z)\,L_B^\mu\Big[2\Gamma_0^i L_B^\nu + 2\beta_0 + \gamma_{B\,0}^i\Big]\\
&\quad - 2L_B^\mu\sum_k I_{ik}^{(1)}(z)\otimes_z P_{kj}^{(0)}(z) - 2L_B^\mu P_{ij}^{(1)}(z) + 2(L_B^\mu)^2\sum_k P_{ik}^{(0)}(z)\otimes_z P_{kj}^{(0)}(z)\\
&\quad + I_{ij}^{(2)}(R,z)\,,
\end{aligned}
\tag{A.13}
$$

where we abbreviated

$$
L_B^\mu = \ln\frac{\mu}{p_T^{\text{cut}}}\,,\quad L_B^\nu = \ln\frac{\nu}{\omega}\,. \tag{A.14}
$$

The one-loop finite terms $I_{ij}^{(1)}$ using the η regulator [58, 59] are given by (see e.g. refs. [13, 19, 24])

$$
\begin{aligned}
I_{q_iq_j}^{(1)}(z) = I_{\bar q_i\bar q_j}^{(1)}(z) &= C_F\,\delta_{ij}\,\theta(z)\theta(1-z)\,2(1-z)\,,\\
I_{q_ig}^{(1)}(z) = I_{\bar q_ig}^{(1)}(z) &= T_F\,\theta(z)\theta(1-z)\,4z(1-z)\,,\\
I_{gg}^{(1)}(z) &= 0\,,\\
I_{gq_i}^{(1)}(z) = I_{g\bar q_i}^{(1)}(z) &= C_F\,\theta(z)\theta(1-z)\,2z\,.
\end{aligned}
\tag{A.15}
$$

Their convolutions with leading-order splitting functions always appear in the form

$$
\big[I^{(1)}\otimes P^{(0)}\big]_{ij}(z) \equiv \sum_k I_{ik}^{(1)}(z)\otimes_z P_{kj}^{(0)}(z)\,. \tag{A.16}
$$

For quark-to-(anti)quark transitions we decompose the above flavor structure as

$$
\begin{aligned}
\big[I^{(1)}\otimes P^{(0)}\big]_{q_iq_j} = \big[I^{(1)}\otimes P^{(0)}\big]_{\bar q_i\bar q_j} &\equiv \delta_{ij}\big[I^{(1)}\otimes P^{(0)}\big]_{qqV} + \big[I^{(1)}\otimes P^{(0)}\big]_{qqS}\,,\\
\big[I^{(1)}\otimes P^{(0)}\big]_{q_i\bar q_j} = \big[I^{(1)}\otimes P^{(0)}\big]_{q_i\bar q_j} &= \big[I^{(1)}\otimes P^{(0)}\big]_{qqS}\,.
\end{aligned}
\tag{A.17}
$$

The building blocks on the right, together with the gluon-to-quark case, are given by

$$
\begin{aligned}
\big[I^{(1)}\otimes P^{(0)}\big]_{qqV} &= 4C_F^2\,\theta(z)\theta(1-z)\,(1-z)\left[2\ln(1-z) - \ln z - \frac{1}{2}\right]\,,\\
\big[I^{(1)}\otimes P^{(0)}\big]_{qqS} &= 4T_FC_F\,\theta(z)\theta(1-z)\left(\frac{4}{3}z^2 + \frac{2}{3z} - 2z\ln z - 2\right)\,,\\
\big[I^{(1)}\otimes P^{(0)}\big]_{q_ig} = \big[I^{(1)}\otimes P^{(0)}\big]_{\bar q_ig} &= \theta(z)\theta(1-z)\Big\{4C_FT_F\left[z^2 + z - (2z+1)\ln z - 2\right]\\
&\quad + 4T_FC_A\left[\frac{34}{3}z^2 - 10z + \frac{2}{3z} - 8z\ln z - 2 + 4z(1-z)\ln(1-z)\right]\\
&\quad + 4T_F\beta_0\,z(1-z)\Big\}\,.
\end{aligned}
\tag{A.18}
$$

JHEP04(2019)142

The convolutions required for the gluon beam function read

$$\begin{aligned}\left[I^{(1)}\otimes P^{(0)}\right]_{gg} &= 4C_F(2n_f)T_F\,\theta(z)\theta(1-z)\big(1+z-2z^2+2z\ln z\big)\,, \\ \left[I^{(1)}\otimes P^{(0)}\right]_{gq_i} &= \left[I^{(1)}\otimes P^{(0)}\right]_{g\bar{q}_i} = 4C_F^2\,\theta(z)\theta(1-z)\left[1+\frac{z}{2}-z\ln z+2z\ln(1-z)\right]\,.\end{aligned} \tag{A.19}$$

These expressions agree with the color-stripped convolutions given in refs. [13, 19], accounting for different conventions for splitting functions. The two-loop finite terms in eq. (A.13) depend on R. Expanding them as

$$I_{ij}^{(2)}(R,z) = \ln R\, I_{ij}^{(2,\ln R)}(z) + I_{ij}^{(2,c)}(z) + \mathcal{O}(R^2)\,, \tag{A.20}$$

the coefficient of $\ln R$ can be written as

$$I_{ij}^{(2,\ln R)}(z) = c_{ij}^R\Big[2P_{ij}^{(0)}(z) - \gamma_{B\,0}^i\,\delta_{ij}\delta(1-z)\Big]\,. \tag{A.21}$$

We explicitly recomputed the coefficients c_{ij}^R, for which we found some discrepancies in the literature. [See eq. (2.31) in the main text.] Note that the terms proportional to $\delta(1-z)$ cancel in eq. (A.21) when the distributional structure of the splitting function is written purely in terms of $\delta(1-z)$, $\mathcal{L}_n(1-z)$, and regular terms in $1-z$.

A.3 Rapidity cut dependent beam functions

Here we provide some details on the computation of the one-loop beam function matching coefficients in eqs. (2.25) and (2.38). We use dimensional regularization for both UV and IR divergences and the η regulator [58, 59] for rapidity divergences. This ensures that all virtual diagrams, PDF diagrams, and zero-bin subtractions are scaleless. We work in Feynman gauge.

The relevant real-radiation diagrams are displayed in figure 16, and the associated expressions for the spin-contracted amplitudes can be read off e.g. from refs. [2, 72] with a proper replacement of the measurement function. For the beam function in eq. (2.12), the measurement on a single n-collinear emission with momentum k^μ and rapidity

$$\eta = \frac{1}{2}\ln\frac{k^-}{k^+} \tag{A.22}$$

reads, including label momentum conservation for $\omega = zp^-$, $k^- = (1-z)p^-$,

$$\begin{aligned}&\mathcal{M}_B(k^\mu, p_T^{\rm cut}, \eta_{\rm cut}, \omega, z) \\ &\quad= \left[\theta\left(e^{2\eta_{\rm cut}} - \frac{k^-}{k^+}\right)\theta(p_T^{\rm cut} - |\vec{k}_T|) + \theta\left(\frac{k^-}{k^+} - e^{2\eta_{\rm cut}}\right)\right]\delta\left(k^- - \frac{\omega(1-z)}{z}\right) \\ &\quad\equiv \mathcal{M}_B^{(\eta<\eta_{\rm cut})}(k^\mu, p_T^{\rm cut}, \eta_{\rm cut}, \omega, z) + \mathcal{M}_B^{(\eta>\eta_{\rm cut})}(k^\mu, \eta_{\rm cut}, \omega, z)\,.\end{aligned} \tag{A.23}$$

Here we will separately display the result for each diagram with $\mathcal{M}_B^{(\eta<\eta_{\rm cut})}$ and $\mathcal{M}_B^{(\eta>\eta_{\rm cut})}$ inserted, respectively. This also allows one to read off the one-loop result for the $B_i^{(\rm cut)}$ beam function in eq. (2.38), for which the measurement on a single emission is just $\mathcal{M}_B^{(\eta>\eta_{\rm cut})}$.

JHEP04(2019)142

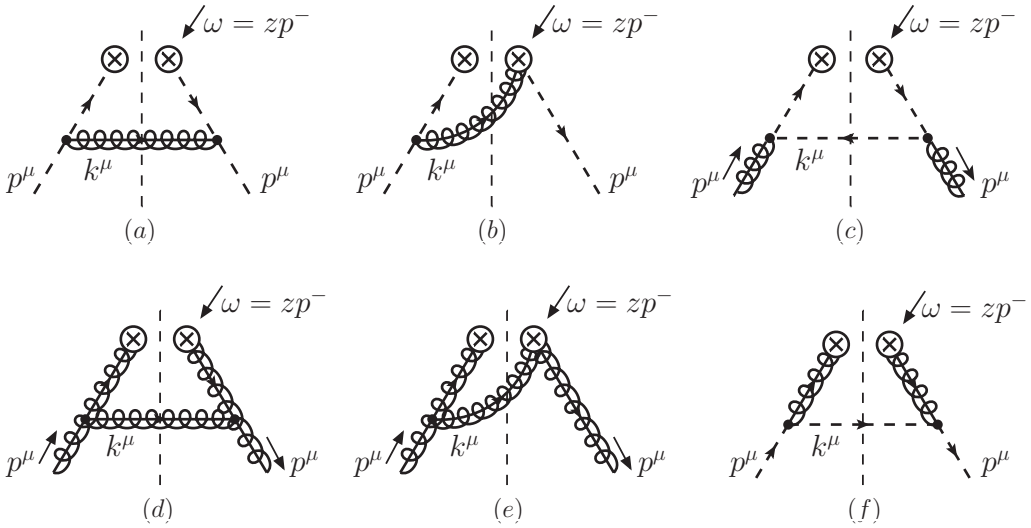

Figure 16. Nonvanishing diagrams for the computation of the one-loop beam function in pure dimensional regularization and Feynman gauge. Symmetric configurations are implicit. The measurement acts on particles crossing the on-shell cut indicated by the vertical dashed line.

On the other hand, for a direct computation of the finite correction due to the rapidity cut in eq. (2.25) it is more convenient to decompose the measurement function as

$$\begin{aligned}
&\mathcal{M}_B(k^\mu, p_T^{\rm cut}, \eta_{\rm cut}, \omega, z) \\
&\quad = \left[\theta(p_T^{\rm cut} - |\vec{k}_T|) + \theta(|\vec{k}_T| - p_T^{\rm cut})\,\theta\left(\frac{k^-}{k^+} - e^{2\eta_{\rm cut}}\right)\right]\delta\left(k^- - \frac{\omega(1-z)}{z}\right) \\
&\quad = \mathcal{M}_B(k^\mu, p_T^{\rm cut}, \omega, z) + \Delta\mathcal{M}_B(k^\mu, p_T^{\rm cut}, \eta_{\rm cut}, \omega, z)\,.
\end{aligned} \tag{A.24}$$

Inserting the first term into matrix elements yields the known results for the matching coefficients without any rapidity cut, while the second term yields the correction.

The relevant diagrams for the computation of the matching coefficient $\mathcal{I}_{qq}$ are (a) and (b). The on-shell condition and label momentum constraint lead to a trivial k^+ integral, which gives for diagram (a), after expanding in ϵ,

$$\begin{aligned}
&\langle q_n|\theta(\omega)\,\mathcal{O}_q^{\rm bare}(p_T^{\rm cut}, \omega)|q_n\rangle^{(a,\eta<\eta_{\rm cut})} \\
&\quad = \frac{\alpha_s C_F}{\pi}\,\theta\left(z - \frac{\omega e^{-\eta_{\rm cut}}}{p_T^{\rm cut} + \omega e^{-\eta_{\rm cut}}}\right)\theta(1-z)\,(1-z)\ln\frac{p_T^{\rm cut} z}{\omega e^{-\eta_{\rm cut}}(1-z)} + \mathcal{O}(\epsilon)\,, \\
&\langle q_n|\theta(\omega)\,\mathcal{O}_q^{\rm bare}(p_T^{\rm cut}, \omega)|q_n\rangle^{(a,\eta>\eta_{\rm cut})} \\
&\quad = \frac{\alpha_s C_F}{\pi}\,\theta(z)\,\theta(1-z)\,(1-z)\left[-\frac{1}{2\epsilon} + \ln\frac{\omega e^{-\eta_{\rm cut}}(1-z)}{\mu\, z} + \frac{1}{2} + \mathcal{O}(\epsilon)\right].
\end{aligned} \tag{A.25}$$

JHEP04(2019)142

Diagram (b) together with its mirror diagram gives, after expanding in η and ϵ,[5]

$$
\begin{aligned}
&\langle q_n|\theta(\omega)\,\mathcal{O}_q^{\rm bare}(p_T^{\rm cut},\omega)|q_n\rangle^{(b,\eta<\eta_{\rm cut})} \\
&\quad=\frac{\alpha_s C_F}{\pi}\,\theta\left(z-\frac{\omega e^{-\eta_{\rm cut}}}{p_T^{\rm cut}+\omega e^{-\eta_{\rm cut}}}\right)\theta(1-z)\Bigg\{\delta(1-z)\left[\frac{1}{\eta}\left(\frac{1}{\epsilon}-2\ln\frac{p_T^{\rm cut}}{\mu}+\mathcal{O}(\epsilon)\right)-\frac{1}{2\epsilon^2}\right. \\
&\qquad\left.+\frac{1}{\epsilon}\ln\frac{\nu e^{-\eta_{\rm cut}}}{\mu}-\ln^2\frac{\omega e^{-\eta_{\rm cut}}}{\mu}+2\ln\frac{p_T^{\rm cut}}{\mu}\ln\frac{\omega}{\nu}+\frac{\pi^2}{24}\right]+2\mathcal{L}_0(1-z)\ln\frac{p_T^{\rm cut}z}{\omega e^{-\eta_{\rm cut}}} \\
&\qquad-2\mathcal{L}_1(1-z)-2\ln\frac{p_T^{\rm cut}z}{\omega e^{-\eta_{\rm cut}}(1-z)}+\mathcal{O}(\eta,\epsilon)\Bigg\}\,, \\
&\langle q_n|\theta(\omega)\,\mathcal{O}_q^{\rm bare}(p_T^{\rm cut},\omega)|q_n\rangle^{(b,\eta>\eta_{\rm cut})} \\
&\quad=\frac{\alpha_s C_F}{\pi}\,\theta(z)\,\theta(1-z)\Bigg\{\delta(1-z)\left[\frac{1}{2\epsilon^2}-\frac{1}{\epsilon}\ln\frac{\omega e^{-\eta_{\rm cut}}}{\mu}+\ln^2\frac{\omega e^{-\eta_{\rm cut}}}{\mu}-\frac{\pi^2}{24}\right] \\
&\qquad+\mathcal{L}_0(1-z)\left[-\frac{1}{\epsilon}+2\ln\frac{\omega e^{-\eta_{\rm cut}}}{\mu\,z}\right]+2\mathcal{L}_1(1-z)+\frac{1}{\epsilon}-2\ln\frac{\omega e^{-\eta_{\rm cut}}(1-z)}{\mu\,z}+\mathcal{O}(\epsilon)\Bigg\}\,.
\end{aligned}
\tag{A.26}
$$

The matching coefficient $\mathcal{I}_{qg}$ is computed from diagram (c) giving

$$
\begin{aligned}
&\langle g_n|\theta(\omega)\,\mathcal{O}_q^{\rm bare}(p_T^{\rm cut},\omega)|g_n\rangle^{(c,\eta<\eta_{\rm cut})} \\
&\quad=\frac{\alpha_s T_F}{\pi}\,\theta\Big(z-\frac{\omega e^{-\eta_{\rm cut}}}{p_T^{\rm cut}+\omega e^{-\eta_{\rm cut}}}\Big)\,\theta(1-z)\,(1-2z+2z^2)\ln\frac{p_T^{\rm cut}z}{\omega e^{-\eta_{\rm cut}}(1-z)}+\mathcal{O}(\epsilon)\,, \\
&\langle g_n|\theta(\omega)\,\mathcal{O}_q^{\rm bare}(p_T^{\rm cut},\omega)|g_n\rangle^{(c,\eta>\eta_{\rm cut})} \\
&\quad=\frac{\alpha_s T_F}{\pi}\,\theta(z)\,\theta(1-z)\Bigg\{(1-2z+2z^2)\left[-\frac{1}{2\epsilon}+\ln\frac{\omega e^{-\eta_{\rm cut}}(1-z)}{\mu\,z}\right]+z(1-z)+\mathcal{O}(\epsilon)\Bigg\}\,.
\end{aligned}
\tag{A.27}
$$

The relevant diagrams for the computation of the matching coefficient $\mathcal{I}_{gg}$ are (d) and (e), which yield

$$
\begin{aligned}
&\langle g_n|\theta(\omega)\,\mathcal{O}_g^{\rm bare}(p_T^{\rm cut},\omega)|g_n\rangle^{(d,\eta<\eta_{\rm cut})} \\
&\quad=\frac{\alpha_s C_A}{\pi}\,\theta\left(z-\frac{\omega e^{-\eta_{\rm cut}}}{p_T^{\rm cut}+\omega e^{-\eta_{\rm cut}}}\right)\theta(1-z)\,\frac{2-2z+3z^2-2z^3}{z}\ln\frac{p_T^{\rm cut}z}{\omega e^{-\eta_{\rm cut}}(1-z)}+\mathcal{O}(\epsilon)\,, \\
&\langle g_n|\theta(\omega)\,\mathcal{O}_g^{\rm bare}(p_T^{\rm cut},\omega)|g_n\rangle^{(d,\eta>\eta_{\rm cut})} \\
&\quad=\frac{\alpha_s C_A}{\pi}\,\theta(z)\,\theta(1-z)\,\frac{2-2z+3z^2-2z^3}{z}\left[-\frac{1}{2\epsilon}+\ln\frac{\omega e^{-\eta_{\rm cut}}(1-z)}{\mu\,z}+\mathcal{O}(\epsilon)\right],
\end{aligned}
\tag{A.28}
$$

[5] For the renormalization one needs to account for the full d dimensional coefficient of the $1/\eta$ divergence, which we do not display here for simplicity.

JHEP04(2019)142

and, including the symmetric contribution of (e),

$$
\begin{aligned}
&\langle g_n|\theta(\omega)\,\mathcal{O}_g^{\text{bare}}(p_T^{\text{cut}},\omega)|g_n\rangle^{(e,\eta<\eta_{\text{cut}})} \\
&\quad= \frac{\alpha_s C_A}{\pi}\,\theta\left(z-\frac{\omega e^{-\eta_{\text{cut}}}}{p_T^{\text{cut}}+\omega e^{-\eta_{\text{cut}}}}\right)\theta(1-z)\Bigg\{\delta(1-z)\left[\frac{1}{\eta}\left(\frac{1}{\epsilon}-2\ln\frac{p_T^{\text{cut}}}{\mu}+\mathcal{O}(\epsilon)\right)-\frac{1}{2\epsilon^2}\right. \\
&\qquad\left.+\frac{1}{\epsilon}\ln\frac{\nu e^{-\eta_{\text{cut}}}}{\mu}-\ln^2\frac{\omega e^{-\eta_{\text{cut}}}}{\mu}+2\ln\frac{p_T^{\text{cut}}}{\mu}\ln\frac{\omega}{\nu}+\frac{\pi^2}{24}\right]+2\mathcal{L}_0(1-z)\ln\frac{p_T^{\text{cut}}z}{\omega e^{-\eta_{\text{cut}}}} \\
&\qquad-2\mathcal{L}_1(1-z)-(2+z)\ln\frac{p_T^{\text{cut}}z}{\omega e^{-\eta_{\text{cut}}}(1-z)}+\mathcal{O}(\eta,\epsilon)\Bigg\}, \\
&\langle g_n|\theta(\omega)\,\mathcal{O}_g^{\text{bare}}(p_T^{\text{cut}},\omega)|g_n\rangle^{(e,\eta>\eta_{\text{cut}})} \\
&\quad= \frac{\alpha_s C_A}{\pi}\,\theta(z)\,\theta(1-z)\Bigg\{\delta(1-z)\left[\frac{1}{2\epsilon^2}-\frac{1}{\epsilon}\ln\frac{\omega e^{-\eta_{\text{cut}}}}{\mu}+\ln^2\frac{\omega e^{-\eta_{\text{cut}}}}{\mu}-\frac{\pi^2}{24}\right] \\
&\qquad+\mathcal{L}_0(1-z)\left[-\frac{1}{\epsilon}+2\ln\frac{\omega e^{-\eta_{\text{cut}}}}{\mu z}\right]+2\mathcal{L}_1(1-z)+(2+z)\left[\frac{1}{2\epsilon}-\ln\frac{\omega e^{-\eta_{\text{cut}}}(1-z)}{\mu z}\right] \\
&\qquad+\mathcal{O}(\epsilon)\Bigg\}.
\end{aligned}
\tag{A.29}
$$

The matching coefficient $\mathcal{I}_{gq}$ is computed from diagram (f), giving

$$
\begin{aligned}
&\langle q_n|\theta(\omega)\,\mathcal{O}_g^{\text{bare}}(p_T^{\text{cut}},\omega)|q_n\rangle^{(f,\eta<\eta_{\text{cut}})} \\
&\quad= \frac{\alpha_s C_F}{\pi}\,\theta\left(z-\frac{\omega e^{-\eta_{\text{cut}}}}{p_T^{\text{cut}}+\omega e^{-\eta_{\text{cut}}}}\right)\theta(1-z)\,\frac{2-2z+z^2}{z}\ln\frac{p_T^{\text{cut}}z}{\omega e^{-\eta_{\text{cut}}}(1-z)}+\mathcal{O}(\epsilon), \\
&\langle q_n|\theta(\omega)\,\mathcal{O}_g^{\text{bare}}(p_T^{\text{cut}},\omega)|q_n\rangle^{(f,\eta>\eta_{\text{cut}})} \\
&\quad= \frac{\alpha_s C_F}{\pi}\,\theta(z)\,\theta(1-z)\left\{\frac{2-2z+z^2}{z}\left[-\frac{1}{2\epsilon}+\ln\frac{\omega e^{-\eta_{\text{cut}}}(1-z)}{\mu z}\right]+\frac{z}{2}+\mathcal{O}(\epsilon)\right\}.
\end{aligned}
\tag{A.30}
$$

Since PDF diagrams are scaleless in pure dimensional regularization, the renormalized beam function matching coefficients are given by the $\mathcal{O}(\epsilon^0\eta^0)$ terms in these expressions. From the results for $\mathcal{M}_B^{(\eta>\eta_{\text{cut}})}$ we get $\mathcal{I}_{ij}^{(\text{cut},1)}$ in eq. (2.38), while adding $\mathcal{M}_B^{(\eta<\eta_{\text{cut}})}$ gives the sum of eq. (2.25) and the second line of eq. (A.13).

A.4 Soft-collinear functions

We again use pure dimensional regularization and the η regulator, so virtual diagrams and soft zero-bin subtractions are scaleless. Note that we expand the η regulator to leading power using the soft-collinear scaling, i.e., for a single emission we insert $|k^-/\nu|^{-\eta}$ rather than $|2k^3/\nu|^{-\eta}$. This choice leads to a scaleless soft zero bin. In Feynman gauge the bare one-loop real contribution to the n-soft-collinear function $\mathcal{S}_i^{(\text{cut})}$ in eq. (2.37) is given by

$$
\mathcal{S}_{i\,\text{bare}}^{(\text{cut},1)}(p_T^{\text{cut}},\eta_{\text{cut}})=4g^2C_i\left(\frac{e^{\gamma_E}\mu^2}{4\pi}\right)^{\epsilon}\int\frac{\mathrm{d}^dk}{(2\pi)^d}\left|\frac{\nu}{k^-}\right|^{\eta}\frac{2\pi\delta^+(k^\mu)}{k^-k^+}\,\mathcal{M}_{\mathcal{S}}^{(\text{cut})}(k^\mu,p_T^{\text{cut}},\eta_{\text{cut}}),
\tag{A.31}
$$

where $\delta^+(k^\mu)=\delta(k^2)\,\theta(k^0)$, and the measurement function reads

$$
\mathcal{M}_{\mathcal{S}}^{(\text{cut})}(k^\mu,p_T^{\text{cut}},\eta_{\text{cut}})=\theta(p_T^{\text{cut}}-|\vec{k}_T|)\,\theta\left(e^{2\eta_{\text{cut}}}-\frac{k^-}{k^+}\right)+\theta\left(\frac{k^-}{k^+}-e^{2\eta_{\text{cut}}}\right).
\tag{A.32}
$$

JHEP04(2019)142

The second term yields a scaleless contribution, while the first term corresponds to a boosted hemisphere and leads to the result

$$\mathcal{S}_{i\,\text{bare}}^{(\text{cut},1)}(p_T^{\text{cut}},\eta_{\text{cut}}) = \frac{\alpha_s C_i}{\pi}\biggl\{\frac{1}{\eta}\biggl[\frac{1}{\epsilon} - 2\ln\frac{p_T^{\text{cut}}}{\mu} + \mathcal{O}(\epsilon)\biggr] - \frac{1}{2\epsilon^2} + \frac{1}{\epsilon}\ln\frac{\nu e^{-\eta_{\text{cut}}}}{\mu} + \ln^2\frac{p_T^{\text{cut}}}{\mu} - 2\ln\frac{p_T^{\text{cut}}}{\mu}\ln\frac{\nu e^{-\eta_{\text{cut}}}}{\mu} + \frac{\pi^2}{24} + \mathcal{O}(\eta,\epsilon)\biggr\}. \tag{A.33}$$

Absorbing the divergent terms (including contributions of the form ϵ^n/η, which are not shown) into counterterms yields the renormalized one-loop result in eq. (2.40).

The bare one-loop contribution to the soft-collinear function resolving the step in eq. (3.13) is again given by eq. (A.31), but this time the measurement reads

$$\mathcal{M}_{\mathcal{S}}^{(\text{step})}(k^\mu,p_T^{\text{cut}},\eta_{\text{cut}}) = \theta(p_T^{\text{cut}} - |\vec{k}_T|)\,\theta\left(e^{2\eta_{\text{cut}}} - \frac{k^-}{k^+}\right) + \theta(\tilde{p}_T^{\text{cut}} - |\vec{k}_T|)\,\theta\left(\frac{k^-}{k^+} - e^{2\eta_{\text{cut}}}\right). \tag{A.34}$$

Successively dropping terms that yield scaleless integrals we can replace ($\mapsto$)

$$\begin{aligned}\mathcal{M}_{\mathcal{S}}^{(\text{step})}(k^\mu,p_T^{\text{cut}},\eta_{\text{cut}}) &\mapsto \theta\left(\frac{k^-}{k^+} - e^{2\eta_{\text{cut}}}\right)\Bigl[\theta(\tilde{p}_T^{\text{cut}} - |\vec{k}_T|) - \theta(p_T^{\text{cut}} - |\vec{k}_T|)\Bigr]\\ &\mapsto \theta\left(e^{2\eta_{\text{cut}}} - \frac{k^-}{k^+}\right)\Bigl[\theta(p_T^{\text{cut}} - |\vec{k}_T|) - \theta(\tilde{p}_T^{\text{cut}} - |\vec{k}_T|)\Bigr]\\ &= \mathcal{M}_{\mathcal{S}}^{(\text{cut})}(k^\mu,p_T^{\text{cut}},\eta_{\text{cut}}) - \mathcal{M}_{\mathcal{S}}^{(\text{cut})}(k^\mu,\tilde{p}_T^{\text{cut}},\eta_{\text{cut}}),\end{aligned} \tag{A.35}$$

so at one loop we find a simple relation between bare results,

$$\mathcal{S}_{i\,\text{bare}}^{(1)}(p_T^{\text{cut}},\tilde{p}_T^{\text{cut}},\eta_{\text{cut}}) = \mathcal{S}_{i\,\text{bare}}^{(\text{cut},1)}(p_T^{\text{cut}},\eta_{\text{cut}}) - \mathcal{S}_{i\,\text{bare}}^{(\text{cut},1)}(\tilde{p}_T^{\text{cut}},\eta_{\text{cut}}). \tag{A.36}$$

Remapping the measurement on the primary emission as in eq. (A.35) yields the analogous relation for the small-R clustering contributions.

A.5 Comparison to quark beam function results in the literature

In ref. [34] the regime $p_T^{\text{cut}} \sim Qe^{-\eta_{\text{cut}}}$ was accounted for by adding a finite contribution $\Delta B_{i/j}^{(1)}$ from so-called out-of-jet radiation to the unmeasured beam function in eq. (2.37) as

$$\mathcal{I}_{ij}^{(\text{cut},1)}(\eta_{\text{cut}},\omega,z,\mu) \mapsto \mathcal{I}_{ij}^{(\text{cut},1)}(\eta_{\text{cut}},\omega,z,\mu) + \Delta B_{i/j}^{(1)}(p_T^{\text{cut}},z,\omega,e^{-\eta_{\text{cut}}}). \tag{A.37}$$

One-loop consistency with our eq. (2.12) reads, at the level of bare ingredients,

$$\begin{aligned}&\mathcal{I}_{ij\,\text{bare}}^{(1)}(p_T^{\text{cut}},\eta_{\text{cut}},\omega,z)\\ &\quad= \mathcal{I}_{ij\,\text{bare}}^{(\text{cut},1)}(\eta_{\text{cut}},\omega,z) + \Delta B_{i/j}^{(1)}(p_T^{\text{cut}},z,\omega,e^{-\eta_{\text{cut}}}) + \delta_{ij}\delta(1-z)\,\mathcal{S}_{i\,\text{bare}}^{(\text{cut},1)}(p_T^{\text{cut}},\eta_{\text{cut}}),\end{aligned} \tag{A.38}$$

where $\mathcal{S}_i^{(\text{cut},1)}$ is the bare soft-collinear function at one loop, see eq. (A.33). By eq. (A.23) we have, in terms of bare collinear matrix elements up to scaleless PDF diagrams,

$$\mathcal{I}_{qq\,\text{bare}}^{(1)}(p_T^{\text{cut}},\eta_{\text{cut}},\omega,z) = \mathcal{I}_{qq\,\text{bare}}^{(\text{cut},1)}(\eta_{\text{cut}},\omega,z) + \langle q_n|\theta(\omega)\,\mathcal{O}_q^{\text{bare}}(p_T^{\text{cut}},\omega)|q_n\rangle^{(\eta<\eta_{\text{cut}})}, \tag{A.39}$$

JHEP04(2019)142

and similarly for $\mathcal{I}_{qg}$. With this, eq. (A.38) simplifies to

$$\begin{aligned}\langle q_n|\theta(\omega)\,\mathcal{O}_q^{\text{bare}}(p_T^{\text{cut}},\omega)|q_n\rangle^{(\eta<\eta_{\text{cut}})} &= \Delta B^{(1)}_{q/q}(p_T^{\text{cut}},z,\omega,e^{-\eta_{\text{cut}}}) + \delta(1-z)\,\mathcal{S}^{(\text{cut},1)}_{q\,\text{bare}}(p_T^{\text{cut}},\eta_{\text{cut}})\,,\\ \langle g_n|\theta(\omega)\,\mathcal{O}_q^{\text{bare}}(p_T^{\text{cut}},\omega)|g_n\rangle^{(\eta<\eta_{\text{cut}})} &= \Delta B^{(1)}_{q/g}(p_T^{\text{cut}},z,\omega,e^{-\eta_{\text{cut}}})\,.\end{aligned} \tag{A.40}$$

Both relations are readily checked after summing over all contributing diagrams.

A.6 Mellin convolutions in the two-loop rapidity dependent beam function

The PDF and beam function RGEs together predict Mellin convolutions of the following form in the two-loop matching kernels eq. (2.24) for the rapidity dependent beam function:

$$\sum_k \Delta I^{(1)}_{ik}(\zeta_{\text{cut}},z)\otimes_z P^{(0)}_{kj}(z) \equiv [\Delta I^{(1)}\otimes P^{(0)}]_{ij}(\zeta_{\text{cut}},z)\,. \tag{A.41}$$

The relevant partonic channels read, leaving all arguments implicit,

$$\begin{aligned}
[\Delta I^{(1)}\otimes P^{(0)}]_{q_iq_j} &= \delta_{ij}\,8C_F^2\,P^w_{qq}\otimes_z P_{qq} + 8T_FC_F\,P^w_{qg}\otimes_z P_{gq} = [\Delta I^{(1)}\otimes P^{(0)}]_{\bar q_i\bar q_j}\,,\\
[\Delta I^{(1)}\otimes P^{(0)}]_{q_i\bar q_j} &= 8T_FC_F\,P^w_{qg}\otimes_z P_{gq} = [\Delta I^{(1)}\otimes P^{(0)}]_{\bar q_iq_j}\,,\\
[\Delta I^{(1)}\otimes P^{(0)}]_{q_ig} &= 8C_FT_F\,P^w_{qq}\otimes_z P_{qg} + 8T_F\left[C_A\,P^w_{qg}\otimes_z P_{gg} + \frac{\beta_0}{2}P^w_{qg}\right] = [\Delta I^{(1)}\otimes P^{(0)}]_{\bar q_ig}\,,\\
[\Delta I^{(1)}\otimes P^{(0)}]_{gg} &= 8C_A\left[C_A\,P^w_{gg}\otimes_z P_{gg} + \frac{\beta_0}{2}P^w_{gg}\right] + 8C_FT_F(2n_f)\,P^w_{gq}\otimes_z P_{qg}\,,\\
[\Delta I^{(1)}\otimes P^{(0)}]_{gq_i} &= 8C_AC_F P^w_{gg}\otimes_z P_{gq} + 8C_F^2 P^w_{gq}\otimes_z P_{qq} = [\Delta I^{(1)}\otimes P^{(0)}]_{g\bar q_i}\,,
\end{aligned} \tag{A.42}$$

where n_f is the number of light quark flavors. Here we introduced a shorthand for weighted color-stripped splitting functions that depend on ζ_{cut} in addition to z,

$$P^w_{ij}(\zeta_{\text{cut}},z) = \theta\left(\frac{\zeta_{\text{cut}}}{1+\zeta_{\text{cut}}}-z\right)\ln\frac{\zeta_{\text{cut}}(1-z)}{z}P_{ij}(z)\,. \tag{A.43}$$

The Mellin convolutions $P^w_{ik}\otimes_z P_{kj}$ are straightforward to evaluate analytically, but the resulting expressions are lengthy. They are available from the authors upon request.

B Jet rapidity cuts in $\mathcal{T}_B$ and $\mathcal{T}_C$ vetoes

Here we comment on how the factorization setup for the smoothly rapidity dependent jet vetoes introduced in ref. [16] is modified when an additional sharp jet rapidity cut is introduced. The restriction on reconstructed jets reads in this case

$$\max_{k\in\text{jets: }|\eta_k|<\eta_{\text{cut}}}\left\{|\vec p_{T,k}|\,f(\eta_k)\right\} < \mathcal{T}_{\text{cut}}\,, \tag{B.1}$$

where $f(\eta)e^{|\eta|}\to 1$ for $\eta\to\pm\infty$. Examples are the beam thrust veto with $f(\eta)=e^{-|\eta|}$ and the C-parameter veto with $f(\eta)=1/(2\cosh\eta)$. The discussion of an additional sharp rapidity cut largely parallels the case of the p_T^{cut} veto in section 2. We again distinguish

JHEP04(2019)142

three hierarchies between $\sqrt{\mathcal{T}_{\rm cut}/Q}$ and $e^{-\eta_{\rm cut}}$, where now $\sqrt{\mathcal{T}_{\rm cut}/Q}$ replaces $p_T^{\rm cut}/Q$ as the characteristic angular size of collinear radiation constrained by the jet veto. The hierarchy $\sqrt{\mathcal{T}_{\rm cut}/Q} \gg e^{-\eta_{\rm cut}}$ (regime 1) reduces to the factorization for $\eta_{\rm cut} \to \infty$ [8, 16, 28], up to power corrections of $\mathcal{O}(e^{-\eta_{\rm cut}}\sqrt{Q/\mathcal{T}_{\rm cut}})$.

For $\sqrt{\mathcal{T}_{\rm cut}/Q} \sim e^{-\eta_{\rm cut}}$ (regime 2) the relevant EFT modes scale as

$$\begin{aligned}
\text{soft:} \quad & p^\mu \sim (\mathcal{T}_{\rm cut}, \mathcal{T}_{\rm cut}, \mathcal{T}_{\rm cut})\,, \\
n_a\text{-collinear:} \quad & p^\mu \sim \Big(\mathcal{T}_{\rm cut}, Q, \sqrt{\mathcal{T}_{\rm cut} Q}\Big) \sim \Big(Q e^{-2\eta_{\rm cut}}, Q, Q e^{-\eta_{\rm cut}}\Big)\,, \\
n_b\text{-collinear:} \quad & p^\mu \sim \Big(Q, \mathcal{T}_{\rm cut}, \sqrt{\mathcal{T}_{\rm cut} Q}\Big) \sim \Big(Q, Q e^{-2\eta_{\rm cut}}, Q e^{-\eta_{\rm cut}}\Big)\,.
\end{aligned} \tag{B.2}$$

The factorized 0-jet cross section reads

$$\begin{aligned}
\sigma_0(\mathcal{T}_{\rm cut}, \eta_{\rm cut}, R, \Phi) = {} & H_\kappa(\Phi, \mu)\, B_a(\mathcal{T}_{\rm cut}, \eta_{\rm cut}, R, \omega_a, \mu)\, B_b(\mathcal{T}_{\rm cut}, \eta_{\rm cut}, R, \omega_b, \mu)\, S_\kappa(\mathcal{T}_{\rm cut}, R, \mu) \\
& \times \left[1 + \mathcal{O}\Big(\frac{\mathcal{T}_{\rm cut}}{Q}, e^{-\eta_{\rm cut}}, R^2\Big)\right].
\end{aligned} \tag{B.3}$$

The beam and soft function are different from the $p_T^{\rm cut}$ veto. The rapidity cut again affects only the beam functions without changing their RG structure or anomalous dimension. In analogy to eq. (2.16) we can write the matching coefficients as

$$\mathcal{I}_{ij}(\mathcal{T}_{\rm cut}, \eta_{\rm cut}, R, \omega, z, \mu) = \mathcal{I}_{ij}(\omega \mathcal{T}_{\rm cut}, R, z, \mu) + \Delta\mathcal{I}_{ij}(\mathcal{T}_{\rm cut}, \eta_{\rm cut}, R, \omega, z, \mu)\,, \tag{B.4}$$

where the first term on the right-hand side is the $\eta_{\rm cut} \to \infty$ matching coefficient as calculated to two loops in ref. [28], which only depends on the boost-invariant product $\omega\mathcal{T}_{\rm cut}$. The correction $\Delta\mathcal{I}_{ij}$ vanishes for $\omega e^{-2\eta_{\rm cut}} \ll \mathcal{T}_{\rm cut}$ and at one loop is given by

$$\begin{aligned}
\Delta\mathcal{I}_{ij}(\mathcal{T}_{\rm cut}, \eta_{\rm cut}, R, \omega, z, \mu) = {} & \frac{\alpha_s(\mu)}{4\pi}\, \theta\left(\frac{\omega e^{-2\eta_{\rm cut}}}{\omega e^{-2\eta_{\rm cut}} + \mathcal{T}_{\rm cut}} - z\right) P_{ij}^{(0)}(z)\, \ln \frac{\omega e^{-2\eta_{\rm cut}}(1-z)}{z\mathcal{T}_{\rm cut}} \\
& + \mathcal{O}(\alpha_s^2)\,.
\end{aligned} \tag{B.5}$$

For $\sqrt{\mathcal{T}_{\rm cut}/Q} \ll e^{-\eta_{\rm cut}}$ (regime 3) we again distinguish two types of collinear modes,

$$\begin{aligned}
n_a\text{-collinear:} \quad & p^\mu \sim \Big(Q e^{-2\eta_{\rm cut}}, Q, Q e^{-\eta_{\rm cut}}\Big)\,, \\
n_a\text{-soft-collinear:} \quad & p^\mu \sim \Big(\mathcal{T}_{\rm cut}, \mathcal{T}_{\rm cut} e^{2\eta_{\rm cut}}, \mathcal{T}_{\rm cut} e^{\eta_{\rm cut}}\Big)\,.
\end{aligned} \tag{B.6}$$

The contributions from these modes can be encoded in a function $\mathcal{B}_i$ which can be refactorized in analogy to eq. (2.37) to resum Sudakov logarithms of $\mathcal{T}_{\rm cut} e^{2\eta_{\rm cut}}/Q$,

$$\begin{aligned}
\mathcal{B}_i(\mathcal{T}_{\rm cut}, \eta_{\rm cut}, R, \omega, z, \mu) = {} & B_i^{(\rm cut)}(\eta_{\rm cut}, \omega, \mu)\, \mathcal{S}_i^{(\rm cut)}\big(\mathcal{T}_{\rm cut} e^{\eta_{\rm cut}}, R, \mu\big) \\
& \times \left[1 + \mathcal{B}_i^{(\rm NG)}\left(\frac{\mathcal{T}_{\rm cut} e^{2\eta_{\rm cut}}}{\omega}, \omega, R\right)\right].
\end{aligned} \tag{B.7}$$

Here, the $\eta_{\rm cut}$ dependent and $\mathcal{T}_{\rm cut}$ independent piece $B_i^{(\rm cut)}$ is identical to the one in eq. (2.37), while the soft-collinear function $\mathcal{S}_i^{(\rm cut)}$ is different and reads

$$\mathcal{S}_i^{(\rm cut)}\big(\mathcal{T}_{\rm cut} e^{\eta_{\rm cut}}, \mu\big) = 1 + \frac{\alpha_s C_i}{4\pi}\left(4\ln^2 \frac{\mathcal{T}_{\rm cut} e^{\eta_{\rm cut}}}{\mu} - \frac{\pi^2}{6}\right) + \mathcal{O}(\alpha_s^2)\,. \tag{B.8}$$

JHEP04(2019)142

The $\mathcal{B}_i^{(\mathrm{NG})}$ piece, which contains nonglobal logarithms starting at $\mathcal{O}(\alpha_s^2)$, is again different from the one in eq. (2.37). We verified that, up to power corrections, the explicit one-loop expressions in eqs. (2.38) and (B.8) reproduce the sum of eq. (B.5) and the matching coefficients without a rapidity cut given in appendix B of ref. [16].

Open Access. This article is distributed under the terms of the Creative Commons Attribution License (CC-BY 4.0), which permits any use, distribution and reproduction in any medium, provided the original author(s) and source are credited.

References

[1] M.A. Ebert et al., *Exploiting jet binning to identify the initial state of high-mass resonances*, *Phys. Rev.* **D 94** (2016) 051901 [arXiv:1605.06114] [INSPIRE].

[2] C.F. Berger, C. Marcantonini, I.W. Stewart, F.J. Tackmann and W.J. Waalewijn, *Higgs Production with a Central Jet Veto at NNLL+NNLO*, *JHEP* **04** (2011) 092 [arXiv:1012.4480] [INSPIRE].

[3] I.W. Stewart and F.J. Tackmann, *Theory Uncertainties for Higgs and Other Searches Using Jet Bins*, *Phys. Rev.* **D 85** (2012) 034011 [arXiv:1107.2117] [INSPIRE].

[4] I.W. Stewart, F.J. Tackmann and W.J. Waalewijn, *Factorization at the LHC: From PDFs to Initial State Jets*, *Phys. Rev.* **D 81** (2010) 094035 [arXiv:0910.0467] [INSPIRE].

[5] I.W. Stewart, F.J. Tackmann and W.J. Waalewijn, *The Beam Thrust Cross Section for Drell-Yan at NNLL Order*, *Phys. Rev. Lett.* **106** (2011) 032001 [arXiv:1005.4060] [INSPIRE].

[6] A. Banfi, G.P. Salam and G. Zanderighi, *NLL+NNLO predictions for jet-veto efficiencies in Higgs-boson and Drell-Yan production*, *JHEP* **06** (2012) 159 [arXiv:1203.5773] [INSPIRE].

[7] T. Becher and M. Neubert, *Factorization and NNLL Resummation for Higgs Production with a Jet Veto*, *JHEP* **07** (2012) 108 [arXiv:1205.3806] [INSPIRE].

[8] F.J. Tackmann, J.R. Walsh and S. Zuberi, *Resummation Properties of Jet Vetoes at the LHC*, *Phys. Rev.* **D 86** (2012) 053011 [arXiv:1206.4312] [INSPIRE].

[9] A. Banfi, P.F. Monni, G.P. Salam and G. Zanderighi, *Higgs and Z-boson production with a jet veto*, *Phys. Rev. Lett.* **109** (2012) 202001 [arXiv:1206.4998] [INSPIRE].

[10] X. Liu and F. Petriello, *Resummation of jet-veto logarithms in hadronic processes containing jets*, *Phys. Rev.* **D 87** (2013) 014018 [arXiv:1210.1906] [INSPIRE].

[11] X. Liu and F. Petriello, *Reducing theoretical uncertainties for exclusive Higgs-boson plus one-jet production at the LHC*, *Phys. Rev.* **D 87** (2013) 094027 [arXiv:1303.4405] [INSPIRE].

[12] T. Becher, M. Neubert and L. Rothen, *Factorization and $N^3LL_p + NNLO$ predictions for the Higgs cross section with a jet veto*, *JHEP* **10** (2013) 125 [arXiv:1307.0025] [INSPIRE].

[13] I.W. Stewart, F.J. Tackmann, J.R. Walsh and S. Zuberi, *Jet p_T resummation in Higgs production at $NNLL' + NNLO$*, *Phys. Rev.* **D 89** (2014) 054001 [arXiv:1307.1808] [INSPIRE].

[14] A. Banfi, P.F. Monni and G. Zanderighi, *Quark masses in Higgs production with a jet veto*, *JHEP* **01** (2014) 097 [arXiv:1308.4634] [INSPIRE].

JHEP04(2019)142

[15] R. Boughezal, X. Liu, F. Petriello, F.J. Tackmann and J.R. Walsh, *Combining Resummed Higgs Predictions Across Jet Bins*, *Phys. Rev.* **D 89** (2014) 074044 [arXiv:1312.4535] [INSPIRE].

[16] S. Gangal, M. Stahlhofen and F.J. Tackmann, *Rapidity-Dependent Jet Vetoes*, *Phys. Rev.* **D 91** (2015) 054023 [arXiv:1412.4792] [INSPIRE].

[17] A. Banfi et al., *Jet-vetoed Higgs cross section in gluon fusion at $N^3LO + NNLL$ with small-R resummation*, *JHEP* **04** (2016) 049 [arXiv:1511.02886] [INSPIRE].

[18] D.Y. Shao, C.S. Li and H.T. Li, *Resummation Prediction on Higgs and Vector Boson Associated Production with a Jet Veto at the LHC*, *JHEP* **02** (2014) 117 [arXiv:1309.5015] [INSPIRE].

[19] Y. Li and X. Liu, *High precision predictions for exclusive VH production at the LHC*, *JHEP* **06** (2014) 028 [arXiv:1401.2149] [INSPIRE].

[20] I. Moult and I.W. Stewart, *Jet Vetoes interfering with $H \to WW$*, *JHEP* **09** (2014) 129 [arXiv:1405.5534] [INSPIRE].

[21] P. Jaiswal and T. Okui, *Explanation of the WW excess at the LHC by jet-veto resummation*, *Phys. Rev.* **D 90** (2014) 073009 [arXiv:1407.4537] [INSPIRE].

[22] T. Becher, R. Frederix, M. Neubert and L. Rothen, *Automated $NNLL + NLO$ resummation for jet-veto cross sections*, *Eur. Phys. J.* **C 75** (2015) 154 [arXiv:1412.8408] [INSPIRE].

[23] Y. Wang, C.S. Li and Z.L. Liu, *Resummation prediction on gauge boson pair production with a jet veto*, *Phys. Rev.* **D 93** (2016) 094020 [arXiv:1504.00509] [INSPIRE].

[24] F.J. Tackmann, W.J. Waalewijn and L. Zeune, *Impact of Jet Veto Resummation on Slepton Searches*, *JHEP* **07** (2016) 119 [arXiv:1603.03052] [INSPIRE].

[25] B. Fuks and R. Ruiz, *A comprehensive framework for studying W' and Z' bosons at hadron colliders with automated jet veto resummation*, *JHEP* **05** (2017) 032 [arXiv:1701.05263] [INSPIRE].

[26] ATLAS collaboration, *Performance of pile-up mitigation techniques for jets in pp collisions at $\sqrt{s} = 8$ TeV using the ATLAS detector*, *Eur. Phys. J.* **C 76** (2016) 581 [arXiv:1510.03823] [INSPIRE].

[27] ATLAS collaboration, *Measurements of Higgs boson properties in the diphoton decay channel with 36 fb^{-1} of pp collision data at $\sqrt{s} = 13$ TeV with the ATLAS detector*, *Phys. Rev.* **D 98** (2018) 052005 [arXiv:1802.04146] [INSPIRE].

[28] S. Gangal, J.R. Gaunt, M. Stahlhofen and F.J. Tackmann, *Two-Loop Beam and Soft Functions for Rapidity-Dependent Jet Vetoes*, *JHEP* **02** (2017) 026 [arXiv:1608.01999] [INSPIRE].

[29] C.W. Bauer, S. Fleming and M.E. Luke, *Summing Sudakov logarithms in $B \to X_s\gamma$ in effective field theory*, *Phys. Rev.* **D 63** (2000) 014006 [hep-ph/0005275] [INSPIRE].

[30] C.W. Bauer, S. Fleming, D. Pirjol and I.W. Stewart, *An Effective field theory for collinear and soft gluons: Heavy to light decays*, *Phys. Rev.* **D 63** (2001) 114020 [hep-ph/0011336] [INSPIRE].

[31] C.W. Bauer and I.W. Stewart, *Invariant operators in collinear effective theory*, *Phys. Lett.* **B 516** (2001) 134 [hep-ph/0107001] [INSPIRE].

JHEP04(2019)142

[32] C.W. Bauer, D. Pirjol and I.W. Stewart, *Soft collinear factorization in effective field theory*, *Phys. Rev.* **D 65** (2002) 054022 [hep-ph/0109045] [INSPIRE].

[33] A. Hornig, Y. Makris and T. Mehen, *Jet Shapes in Dijet Events at the LHC in SCET*, *JHEP* **04** (2016) 097 [arXiv:1601.01319] [INSPIRE].

[34] A. Hornig, D. Kang, Y. Makris and T. Mehen, *Transverse Vetoes with Rapidity Cutoff in SCET*, *JHEP* **12** (2017) 043 [arXiv:1708.08467] [INSPIRE].

[35] D. Kang, Y. Makris and T. Mehen, *From Underlying Event Sensitive To Insensitive: Factorization and Resummation*, *JHEP* **09** (2018) 055 [arXiv:1803.04413] [INSPIRE].

[36] Z.-B. Kang, F. Ringer and I. Vitev, *The semi-inclusive jet function in SCET and small radius resummation for inclusive jet production*, *JHEP* **10** (2016) 125 [arXiv:1606.06732] [INSPIRE].

[37] M.A. Ebert et al., *SCETlib: A C++ Package for Numerical Calculations in QCD and Soft-Collinear Effective Theory*, DESY-17-099 (2018).

[38] J.M. Campbell and R.K. Ellis, *An Update on vector boson pair production at hadron colliders*, *Phys. Rev.* **D 60** (1999) 113006 [hep-ph/9905386] [INSPIRE].

[39] J.M. Campbell, R.K. Ellis and C. Williams, *Vector boson pair production at the LHC*, *JHEP* **07** (2011) 018 [arXiv:1105.0020] [INSPIRE].

[40] J.M. Campbell, R.K. Ellis and W.T. Giele, *A Multi-Threaded Version of MCFM*, *Eur. Phys. J.* **C 75** (2015) 246 [arXiv:1503.06182] [INSPIRE].

[41] R.V. Harlander, S. Liebler and H. Mantler, *SusHi: A program for the calculation of Higgs production in gluon fusion and bottom-quark annihilation in the Standard Model and the MSSM*, *Comput. Phys. Commun.* **184** (2013) 1605 [arXiv:1212.3249] [INSPIRE].

[42] R.V. Harlander, S. Liebler and H. Mantler, *SusHi Bento: Beyond NNLO and the heavy-top limit*, *Comput. Phys. Commun.* **212** (2017) 239 [arXiv:1605.03190] [INSPIRE].

[43] R.V. Harlander and W.B. Kilgore, *Next-to-next-to-leading order Higgs production at hadron colliders*, *Phys. Rev. Lett.* **88** (2002) 201801 [hep-ph/0201206] [INSPIRE].

[44] R. Harlander and P. Kant, *Higgs production and decay: Analytic results at next-to-leading order QCD*, *JHEP* **12** (2005) 015 [hep-ph/0509189] [INSPIRE].

[45] J. Butterworth et al., *PDF4LHC recommendations for LHC Run II*, *J. Phys.* **G 43** (2016) 023001 [arXiv:1510.03865] [INSPIRE].

[46] S. Dulat et al., *New parton distribution functions from a global analysis of quantum chromodynamics*, *Phys. Rev.* **D 93** (2016) 033006 [arXiv:1506.07443] [INSPIRE].

[47] L.A. Harland-Lang, A.D. Martin, P. Motylinski and R.S. Thorne, *Parton distributions in the LHC era: MMHT 2014 PDFs*, *Eur. Phys. J.* **C 75** (2015) 204 [arXiv:1412.3989] [INSPIRE].

[48] NNPDF collaboration, *Parton distributions for the LHC Run II*, *JHEP* **04** (2015) 040 [arXiv:1410.8849] [INSPIRE].

[49] J. Gao and P. Nadolsky, *A meta-analysis of parton distribution functions*, *JHEP* **07** (2014) 035 [arXiv:1401.0013] [INSPIRE].

[50] S. Carrazza, S. Forte, Z. Kassabov, J.I. Latorre and J. Rojo, *An Unbiased Hessian Representation for Monte Carlo PDFs*, *Eur. Phys. J.* **C 75** (2015) 369 [arXiv:1505.06736] [INSPIRE].

JHEP04(2019)142

[51] Y. Hatta and T. Ueda, *Resummation of non-global logarithms at finite N_c*, *Nucl. Phys.* **B 874** (2013) 808 [arXiv:1304.6930] [INSPIRE].

[52] S. Caron-Huot, *Resummation of non-global logarithms and the BFKL equation*, *JHEP* **03** (2018) 036 [arXiv:1501.03754] [INSPIRE].

[53] A.J. Larkoski, I. Moult and D. Neill, *Non-Global Logarithms, Factorization and the Soft Substructure of Jets*, *JHEP* **09** (2015) 143 [arXiv:1501.04596] [INSPIRE].

[54] T. Becher, M. Neubert, L. Rothen and D.Y. Shao, *Factorization and Resummation for Jet Processes*, *JHEP* **11** (2016) 019 [*Erratum ibid.* **05** (2017) 154] [arXiv:1605.02737] [INSPIRE].

[55] D.W. Kolodrubetz, P. Pietrulewicz, I.W. Stewart, F.J. Tackmann and W.J. Waalewijn, *Factorization for Jet Radius Logarithms in Jet Mass Spectra at the LHC*, *JHEP* **12** (2016) 054 [arXiv:1605.08038] [INSPIRE].

[56] S.D. Ellis, C.K. Vermilion, J.R. Walsh, A. Hornig and C. Lee, *Jet Shapes and Jet Algorithms in SCET*, *JHEP* **11** (2010) 101 [arXiv:1001.0014] [INSPIRE].

[57] M. Procura and W.J. Waalewijn, *Fragmentation in Jets: Cone and Threshold Effects*, *Phys. Rev.* **D 85** (2012) 114041 [arXiv:1111.6605] [INSPIRE].

[58] J.-y. Chiu, A. Jain, D. Neill and I.Z. Rothstein, *The Rapidity Renormalization Group*, *Phys. Rev. Lett.* **108** (2012) 151601 [arXiv:1104.0881] [INSPIRE].

[59] J.-Y. Chiu, A. Jain, D. Neill and I.Z. Rothstein, *A Formalism for the Systematic Treatment of Rapidity Logarithms in Quantum Field Theory*, *JHEP* **05** (2012) 084 [arXiv:1202.0814] [INSPIRE].

[60] A. Hornig, C. Lee, I.W. Stewart, J.R. Walsh and S. Zuberi, *Non-global Structure of the $O(\alpha_s^2)$ Dijet Soft Function*, *JHEP* **08** (2011) 054 [*Erratum ibid.* **10** (2017) 101] [arXiv:1105.4628] [INSPIRE].

[61] M. Balsiger, T. Becher and D.Y. Shao, *Non-global logarithms in jet and isolation cone cross sections*, *JHEP* **08** (2018) 104 [arXiv:1803.07045] [INSPIRE].

[62] G. Bell, R. Rahn and J. Talbert, *Automated Calculation of Dijet Soft Functions in Soft-Collinear Effective Theory*, PoS(RADCOR2015)052 (2016) [arXiv:1512.06100] [INSPIRE].

[63] G. Bell, R. Rahn and J. Talbert, *Automated Calculation of Dijet Soft Functions in the Presence of Jet Clustering Effects*, PoS(RADCOR2017)047 (2018) [arXiv:1801.04877] [INSPIRE].

[64] Z. Ligeti, I.W. Stewart and F.J. Tackmann, *Treating the b quark distribution function with reliable uncertainties*, *Phys. Rev.* **D 78** (2008) 114014 [arXiv:0807.1926] [INSPIRE].

[65] R. Abbate, M. Fickinger, A.H. Hoang, V. Mateu and I.W. Stewart, *Thrust at N^3LL with Power Corrections and a Precision Global Fit for $\alpha_s(m_Z)$*, *Phys. Rev.* **D 83** (2011) 074021 [arXiv:1006.3080] [INSPIRE].

[66] M.A. Ebert, J.K.L. Michel and F.J. Tackmann, *Resummation Improved Rapidity Spectrum for Gluon Fusion Higgs Production*, *JHEP* **05** (2017) 088 [arXiv:1702.00794] [INSPIRE].

[67] G. Curci, W. Furmanski and R. Petronzio, *Evolution of Parton Densities Beyond Leading Order: The Nonsinglet Case*, *Nucl. Phys.* **B 175** (1980) 27 [INSPIRE].

[68] W. Furmanski and R. Petronzio, *Singlet Parton Densities Beyond Leading Order*, *Phys. Lett.* **97B** (1980) 437 [INSPIRE].

JHEP04(2019)142

[69] R.K. Ellis and W. Vogelsang, *The Evolution of parton distributions beyond leading order: The Singlet case*, hep-ph/9602356 [INSPIRE].

[70] J.R. Gaunt, M. Stahlhofen and F.J. Tackmann, *The Quark Beam Function at Two Loops*, *JHEP* **04** (2014) 113 [arXiv:1401.5478] [INSPIRE].

[71] J. Gaunt, M. Stahlhofen and F.J. Tackmann, *The Gluon Beam Function at Two Loops*, *JHEP* **08** (2014) 020 [arXiv:1405.1044] [INSPIRE].

[72] I.W. Stewart, F.J. Tackmann and W.J. Waalewijn, *The Quark Beam Function at NNLL*, *JHEP* **09** (2010) 005 [arXiv:1002.2213] [INSPIRE].

JHEP04(2019)142